Lawrence Berkeley National Laboratory
Recent Work

Title

Application of a-Si:H Radiation Detectors in Medical Imaging

Permalink

https://escholarship.org/uc/item/8d98t67m

Author

Lee, H.-K.

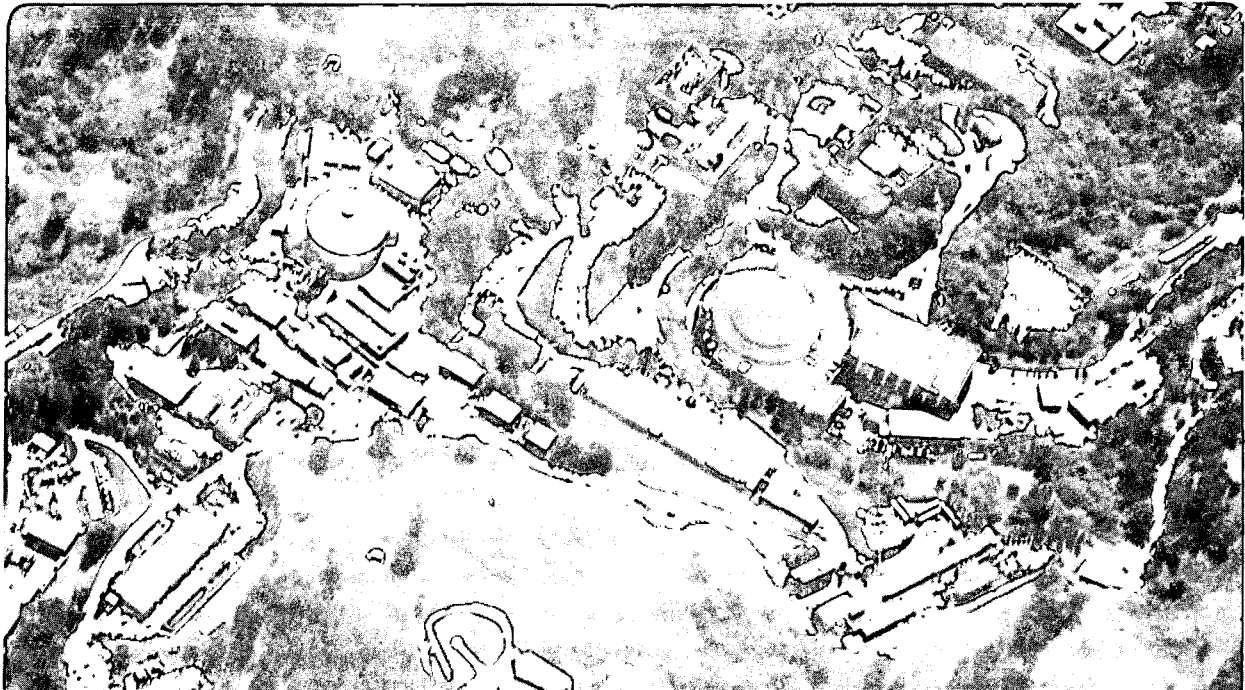**Publication Date**

1995-06-12

Lawrence Berkeley Laboratory
UNIVERSITY OF CALIFORNIA

Physics Division

Application of a-Si:H Radiation Detectors in Medical Imaging

H.-K. Lee
(Ph.D. Thesis)

June 1995

DISCLAIMER

Application of a-Si:H Radiation Detectors in Medical Imaging

Hyoung-Koo Lee

Ph.D. Thesis

Department of Nuclear Engineering
University of California at Berkeley
and
Physics Division
Lawrence Berkeley Laboratory
Berkeley, CA 94720

June 1995

Application of a-Si:H Radiation Detectors
in Medical Imaging

by

Hyoung-Koo Lee

B.S. (Seoul National University) 1986
M.S. (Seoul National University) 1988

A dissertation submitted in partial satisfaction of the

requirements for the degree of

Doctor of Philosophy

in

Engineering-Nuclear Engineering

in the

GRADUATE DIVISION

of the

UNIVERSITY of CALIFORNIA at BERKELEY

Committee in charge:

Professor Selig N. Kaplan, Chair
Professor Victor Perez-Mendez
Professor Thomas F. Budinger

1995

Application of a-Si:H Radiation Detectors

in Medical Imaging

© 1995

by

Hyoung-Koo Lee

Abstract

Application of a-Si:H Radiation Detectors
in Medical Imaging

by

Hyoung-Koo Lee

Doctor of Philosophy in Engineering-Nuclear Engineering

University of California at Berkeley

Professor Selig N. Kaplan, Chair
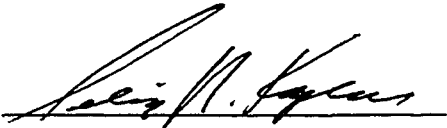
Monte Carlo simulations of a proposed a-Si:H-based current-integrating gamma camera were performed. The analysis showed that the intrinsic resolution of such a camera was 1 ~ 2.5 mm, which is somewhat better than that of a conventional gamma camera, and that the greater blurring, due to the detection of scattered γ-rays, could be reduced considerably by image restoration techniques. This proposed gamma camera would be useful for imaging shallow organs such as the thyroid. Prototype charge-storage a-Si:H pixel detectors for such a camera were designed, constructed and tested. The detectors could store signal charge as long as 5 min at -26°C. The thermal generation current in reverse biased a-Si:H p-i-n photodetectors was investigated, and the Poole-Frenkel effect was found to be the most significant source of the thermal generation current. Based on the Poole-Frenkel effect, voltage- and time-dependent thermal generation current was modeled. Using this model, the operating

1

conditions of the proposed a-Si:H gamma camera, such as the operating temperature, the operating bias and the γ-scan period, could be predicted.

The transient photoconductive gain mechanism in various a-Si:H devices was investigated for applications in digital radiography. Using the a-Si:H photoconductors in n-i-n configuration in pixel arrays, enhancement in signal collection (more than 200 times higher signal level) can be achieved in digital radiography, compared to the ordinary p-i-n type a-Si:H x-ray imaging arrays .

Committee in charge: Selig N. Kaplan, Chair
                         Victor Perez-Mendez
                         Thomas F. Budinger

To my mother, wife and daughter,

and to the memory of my father

Table of Contents

Acknowledgements

I would like to thank Dr. Victor Perez-Mendez, who is a professor of Physics in the Department of Radiology in UCSF and a faculty senior scientist in LBL, for his great ideas, valuable suggestions and guidance during my tenure in the Lawrence Berkeley Laboratory. I also would like to thank Dr. Selig N. Kaplan, who is my research advisor in the Department of Nuclear Engineering, for his kindness, helpful discussions and guidance to complete my Ph.D. program in UC Berkeley. My appreciation is extended to Dr. Thomas F. Budinger for his valuable discussions on gamma cameras and other medical imaging technologies. I would like to thank my group members, Dr. John Drewery, Dr. Gyuseong Cho, Dr. Ali Mireshghi, Wan-Shick Hong, Tao Jing and Daniel Wildermuth for experimental assistance and discussions during my research. I express gratitude to Dr. Olander and Dr. Fowler, who are professors in the Department of Nuclear Engineering in UC Berkeley, for their useful classes and warm guidance.

I would like to thank my mother and my late father who have supported me through my life. I also would like to thank my wife, Meehyang who is always there whenever I need her and my daughter, Sharon who refreshes my mind every time I see a smile on her beautiful face. Finally, I would like to thank our Lord who has made who I am, and has been with me and always will be.

Chapter 1   Introduction

Although its history is short compared to other semiconductor materials, hydrogenated amorphous silicon (a-Si:H) has been investigated extensively in many groups around the world in connection with its various applications. Due to its ability of being deposited on a large area substrate with any geometry and its high radiation hardness, a-Si:H has also been candidated as a material for large area radiation imaging devices. Even though it is still under development, a-Si:H radiation imaging arrays may replace many of the conventional imaging devices in the near future. In this chapter the historical background, production method, structure and basic properties of a-Si:H are briefly described.

1.1   History of a-Si:H

A-Si:H is a relatively new material. It was first made in England in 1969 by Chittick et al. using glow discharge.[1] Before that time amorphous silicon was made by sputtering or by thermal evaporation, which produced unhydrogenated amorphous silicon. The amorphous silicon without hydrogen has a high defect density and cannot be doped, hence did not draw much attention from scientists. Even the improvement of photoconductivity and defect density of amorphous silicon using hydrogenation by Chittick was not of significant interest at that time because the overall electronic quality of a-Si:H was still far worse than that of crystal semiconductors. In 1975 Spear and LeComber reported that substitutional n-type or p-type

doping was possible by adding phosphine or diborane to silane.[2] Since then many scientists started having interest in a-Si:H and research on this material has been widely performed. In 1976 Carlson and Wronski first made a-Si:H solar cells utilizing the photovoltaic effect of p-i-n structure.[3] The thickness of the device was ~1μm and they could obtain 2.4% conversion efficiency in AM-1 sunlight. As for large area a-Si:H devices, Snell and his coworkers first reported field effect transistors for liquid crystal displays in 1981.[4] Since then various applications of large area a-Si:H devices, such as optical scanners and radiation imaging arrays, have been studied. Wei et al first demonstrated in 1985 that an a-Si:H p-i-n diode coupled with a layer of phosphor could be used as an x-ray sensor.[5] They used ZnS(Ni) and $CdWO_4$ as phosphors and reported linear response of the sensor output current to the input x-ray. From their measurement results they proposed that a-Si:H sensor arrays might replace the detector arrays made of crystalline Si, Ge, CdTe and HgI_2 in medical imaging devices such as x-ray computed tomography scanners. Charged particle detection using a-Si:H p-i-n diodes was first performed by Perez-Mendez and Kaplan et. al. in 1986.[6] They used single layer and back-to-back coupled p-i-n diodes without scintillator and measured alpha particle from [241]Am.

1.2   Fabrication

The usual method of depositing a-Si:H is Plasma Enhanced Chemical Vapor Deposition (PECVD). A typical PECVD reactor is schematically shown in Fig. 1-1. Silane gas and other added gases for doping are decomposed by the plasma and grown on a substrate. The
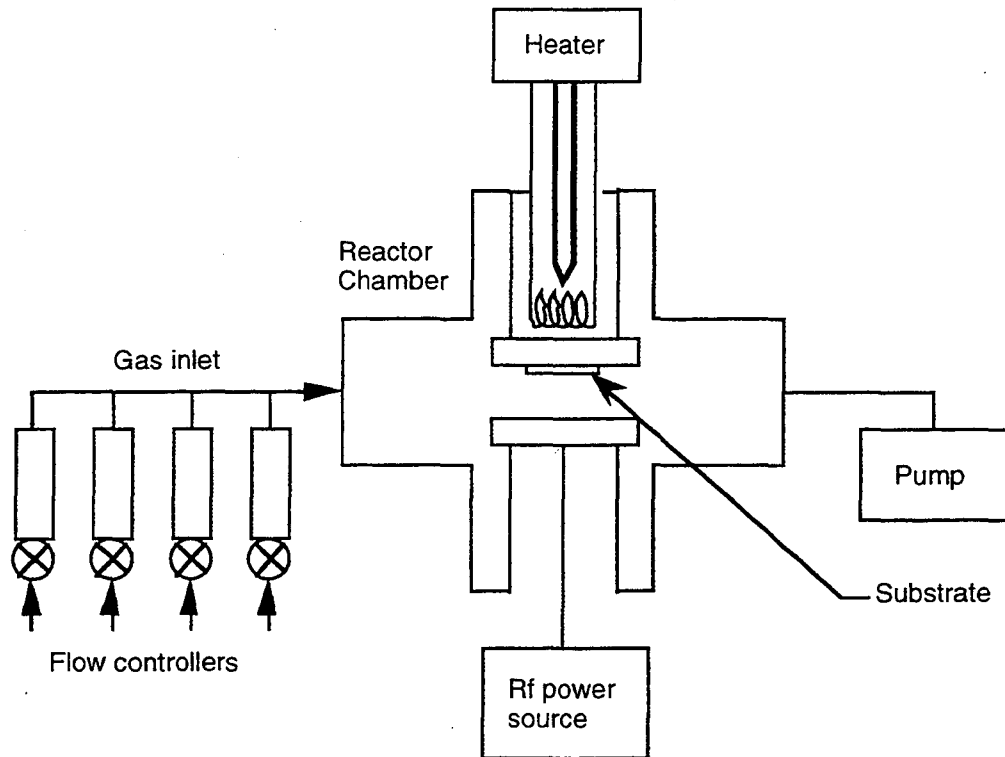
Fig. 1-1   Schematic diagram of a typical PECVD reactor for
a-Si:H deposition.

deposition temperature controls the chemical reactions on the growing surface and is usually less than 250 °C. The amorphous silicon film can be grown at higher temperature, but the quality is worse because hydrogen does not remain in the film.[7] If the deposition temperature is too low, hydrogen cannot diffuse into the structure, hence a more disordered structure is formed. The other parameters which control the deposition process are gas pressure, gas flow rate and rf power. The gas pressure determines the mean free path of the gas molecules, and the usual pressure is 0.1 ~ 1 Torr. The gas flow rate controls the residence time of the gases in the reactor, and the rf power determines the film growth rate.

Many modifications on the glow discharge technique have been studied to improve the quality of a-Si:H material, and recently, using a

3

hydrogen dilution technique with PECVD, improved electronic properties of a-Si:H samples which contain microcrystalline silicon were reported.[8] A fast deposition rate by He dilution of silane at low deposition temperature was also reported, and using this technique thick a-Si:H samples with low stress can be successfully made.[9]

1.3   Structure and basic properties

Amorphous silicon is a material which has a disordered structure, but not completely disordered. It has the same short range order as the crystal silicon but not the long range order. Usually the structure of amorphous semiconductors is explained by a continuous random network. The continuous random network model treats the structure of a covalently bonded amorphous material such that a perfect connectivity is maintained among atoms but the periodicity is not well retained.[7,10] As the short range order is well preserved, the overall electronic property of amorphous silicon is similar to that of the crystal silicon. But due to the long range disorder, the abrupt band edges of crystal silicon are replaced by a broadened tail state distribution which extend into the forbidden gap. Amorphous semiconductors generally have well-defined bond lengths, bond angles and coordinations. The coordination is the specific numbers of bonds of an atom to immediate neighboring atoms. It is determined by the famous '8-N' rule by Mott,[11] and is four in silicon. When an atom has too many or too few bonds a coordination defect is formed, and this structural defect is referred to as a dangling bond. Dangling bonds produce deep electronic states in the forbidden gap, and control the electronic properties

by trapping and recombination. Hydrogenation of amorphous silicon improves the electronic quality by reducing dangling bond density. The atomic hydrogen concentration in good a-Si:H materials is about 10%. The structure of a-Si:H is schematically illustrated in Fig. 1-2.

The wavefunction of electronic states in crystalline silicon can be obtained by solving the Schrödinger equation with a periodic potential well, and is described by the Block wave,[12]

$$\Psi(\mathbf{r}, \mathbf{k}) = u(\mathbf{r}, \mathbf{k}) \exp(i\mathbf{k} \cdot \mathbf{r}) \quad ,$$

where $u(\mathbf{r}, \mathbf{k})$ is periodic in $\mathbf{r}$ with the periodicity of the crystal lattice. The wavefunction, which extends throughout the crystal, has a well-defined momentum $\mathbf{k}$, and the allowed energies of electrons can be represented by means of a E-k dispersion relations in k-space. Hence, the band gap in a crystal is a consequence of the periodicity of the lattice. In a-Si:H, however, as there is no periodicity, k-space cannot exist and the wavefunction cannot

$\bigcirc$ Si $\cdot \text{o}$ H $\bullet$— dangling bond
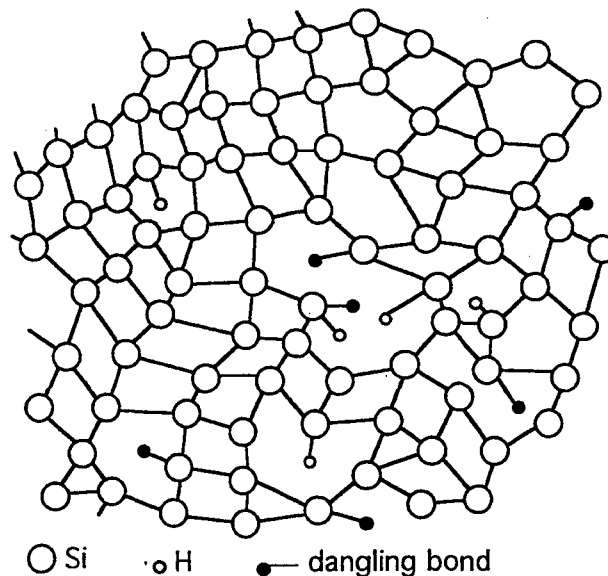
Fig. 1-2   Schematic diagram of a-Si:H material structure which shows the continuous random network.

5

be expressed by the Block wave. Therefore, the band gap cannot be described by E-k dispersion relations any more. The density of states, however, is valid as a description of electron states for both crystal and amorphous silicon.[10] Weaire and Thorpe showed that the electronic density of states are mainly determined by the short range order and that a gap could exist for a tetrahedrally coordinated amorphous solid.[13] The density of states distribution in a-Si:H is compared with that of crystal silicon in Fig. 1-3. The sharp features in the density of states in crystal silicon become smeared out in a-Si:H due to lack of the long range order. Fluctuations in short range order such as bond angle distortion also contribute to the tail states.

In an amorphous semiconductor, electrons may become localized, that is, the wavefunction is confined to a small volume rather than being
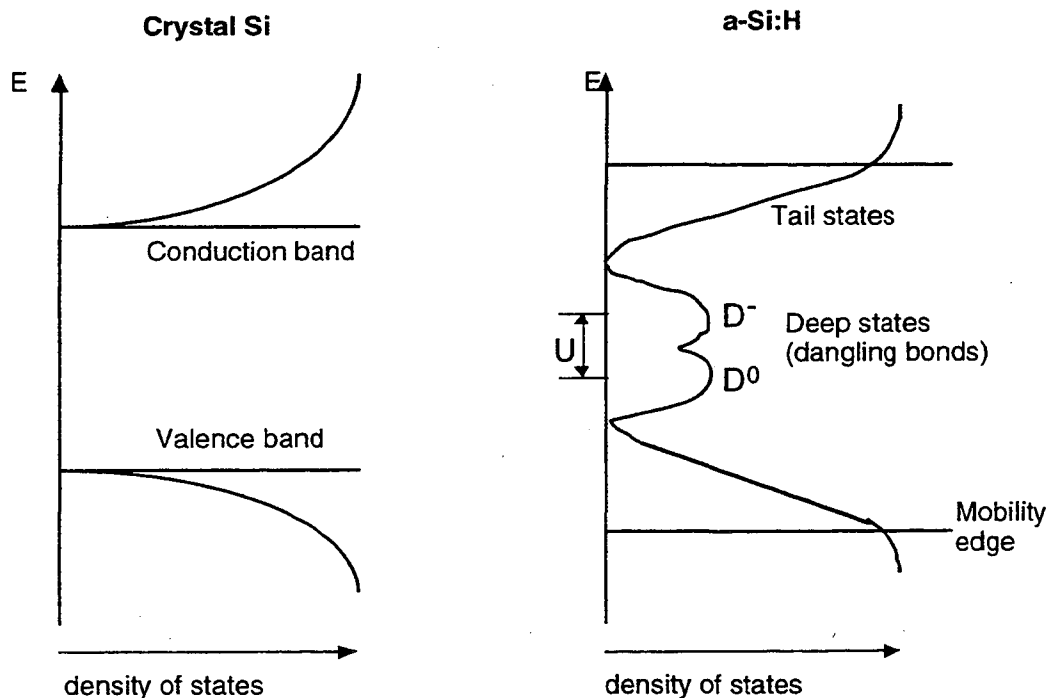
Fig. 1-3   Schematic diagram of density of states in crystal silicon and a-Si:H.

extended. The electron localization in amorphous material was first modeled by Anderson, who showed that if the average of the disordered potential experienced by electrons exceeds a critical value, all of the electron states in the material are localized.[14] The probability of localization is high in tail states because these are generally attributed to distorted sites.[10] Mott showed that there is a critical energy E_c below which the allowed states are localized, and conduction is achieved by thermally-activated hopping to another localized state or by thermal excitation to energies above E_c.[15] This E_c which demarcates localized states and extended states is termed the 'mobility edge', and is shown in Fig. 1-3. At T=0K, the mobility of electrons above the mobility edge is finite, but the electrons below the mobility edge are immobile. The energy difference between the mobility edges is called mobility gap and is about 1.9 eV in a-Si:H.[7]

A dangling bond, which is the source of generation and recombination centers in the forbidden gap, can have three charge states: +e, 0 and -e. When it is occupied by a single electron it is neutral. When an electron is added to a singly occupied dangling bond, the two electrons repel each other by the Coulomb force and the energy levels are split by the so-called correlation energy.[7] The D^- and D^0 state splitting due to the correlation energy U is schematically shown in Fig. 1-3.

In amorphous semiconductors the mobilities of electrons and holes are reduced due to scattering, which increases with the degree of disorder. In a-Si:H the microscopic mobility, which is defined as the mobility of free carriers in the extended states, is ~10 cm^2/Vsec, and ~1 cm^2/Vsec for electrons and holes, respectively. At room temperature, electrons and

7

holes spend some fraction of their life in the extended states and some fraction in the localized states. In other words, electrons, for example, keep trapping and detrapping between the extended states above the mobility edge and the tail states below the mobility edge. Therefore the transport of charge carriers is trap-limited, and the effective carrier mobility, which is called drift mobility, is consequently lower than the microscopic free carrier mobility. In a-Si:H the drift mobility is ~1 cm^2/Vsec, and ~$5x10^{-3}$ cm^2/Vsec for electrons and holes, respectively. As the detrapping mechanism is determined by the thermal energy, the drift mobility is temperature dependent, and if the temperature is sufficiently high the drift mobility is equal to the microscopic mobility since most of the carriers will be in the extended states.

References

[1]   R. C. Chittick, J. H. Alexander and H. F. Sterling, "The Preparation and Properties of Amorphous Silicon," J. Electrochemical Soc., 116, 77 (1969)

[2]   W. E. Spear and P. G. LeComber, "Substitutional Doping of Amorphous Silicon," Solid State Commun., 17, 1193 (1975)

[3]   D. E. Carlson and C. R. Wronski, "Amorphous Silicon Solar Cell," Appl. Phys. Lett., 28, 671 (1976)

[4]   A. J. Snell, K. D. Mackenzie, W. E. Spear, P. G. LeComber and A. J. Hughes, "Application of Amorphous Silicon Field Effect Transistors in Addressable Liquid Crystal Display Panels," Appl. Phys., 24, 357 (1981)

[5]   G.-P. Wei, H. Okamoto and Y. Hamakawa, "Amorphous-Silicon Photovoltaic X-Ray Sensor," Jpn. J. Appl. Phys., 24, 1105 (1985)

[6]   S. N. Kaplan, J. R. Morel, T. A. Mulera, V. Perez-Mendez, G. Schnurmacher and R. A. Street, "Detection of Charged Particles in Amorphous Silicon Layers," IEEE Trans. Nucl. Sci., 33, 351 (1986)

[7]   R. A. Street, *Hydrogenated Amorphous Silicon*, Cambridge University Press, Cambridge (1991)

[8]   A. Mireshghi, W. S. Hong, J. S. Drewery, T. Jing, S. N. Kaplan, H. K. Lee and V. Perez-Mendez, "Improved Electrical and Transport Characteristics of Amorphous Silicon by Enriching with Microcrystalline Silicon," Presented at Mat. Res. Soc. Meeting at San Francisco in April (1994)

[9]   W. S. Hong, A. Mireshghi, J. S. Drewery, T. Jing, Y. Kitsuno, H. K. Lee, S. N. Kaplan and V. Perez-Mendez, "Charged Particle Detectors Based on High Quality Amorphous Silicon Deposited with Hydrogen or Helium Dilution of Silane," Presented at IEEE Nuclear Science Symposium at Norfolk in November (1994)

[10]   S. R. Elliot, *Physics of Amorphous Materials*, 2nd Ed., Longman Scientific & Technical, Harlow, England (1990)

[11]   N. F. Mott, "Conduction in Non-Crystalline Materials: III. Localized States in a Pseudogap and Near Extremities of Conduction and Valence Bands," Philos. Mag., 19, 835 (1969)

[12]   S. Wang, *Fundamentals of Semiconductor Theory and Device Physics*, Prentice-Hall International, Inc., London (1989)

[13]   D. Weaire and M. F. Thorpe, "Electronic Properties of an Amorphous Solid. I.A Simple Tight-Binding Theory," Phys. Rev., B4, 2508 (1971)

[14]   P. W. Anderson, "Absence of Diffusion in Certain Random Lattices," Phys. Rev., 109, 1492 (1958)

[15]   N. F. Mott, "Electrons in Disordered Structures," Adv. Phys., 16, 49 (1967)

Chapter 2   Radiation Detection Principles

2.1   Detection Scheme with a-Si:H Detectors

The radiation detectors made from a-Si:H are either p-i-n or Schottky
barrier structures in sandwich type. Since the p- and n- layers provide
better blocking junctions,[1] p-i-n diodes are more frequently used than the
Schottky barrier devices. Unlike crystalline silicon detectors, for a-Si:H a
p-n junction is ineffective without the intrinsic layer, because the mean free
path of the minority carriers in p- and n-type a-Si:H is too short.[2,3]
During radiation detection the a-Si:H p-i-n diode is reverse biased, and the
signal charge is collected by the depletion field which is imposed by a
reverse bias. The a-Si:H p-i-n diodes can be fabricated in small pixels,
making two dimensional imaging using a-Si:H pixel detector arrays
possible. There are two possible schemes of radiation detection using
a-Si:H p-i-n diodes: direct detection and indirect detection, which are
discussed in the following subsections.

2.1.1 Direct Detection

In this scheme, the electron-hole pairs are generated in the p-i-n
diode by interaction with the incident radiation itself. In Fig. 2-1 (a), the
direct detection method is schematically shown. Using this scheme, a fast
signal can be obtained if the reverse bias is sufficiently high. Also a good
spatial resolution can be achieved when the detectors constitute a pixel

11
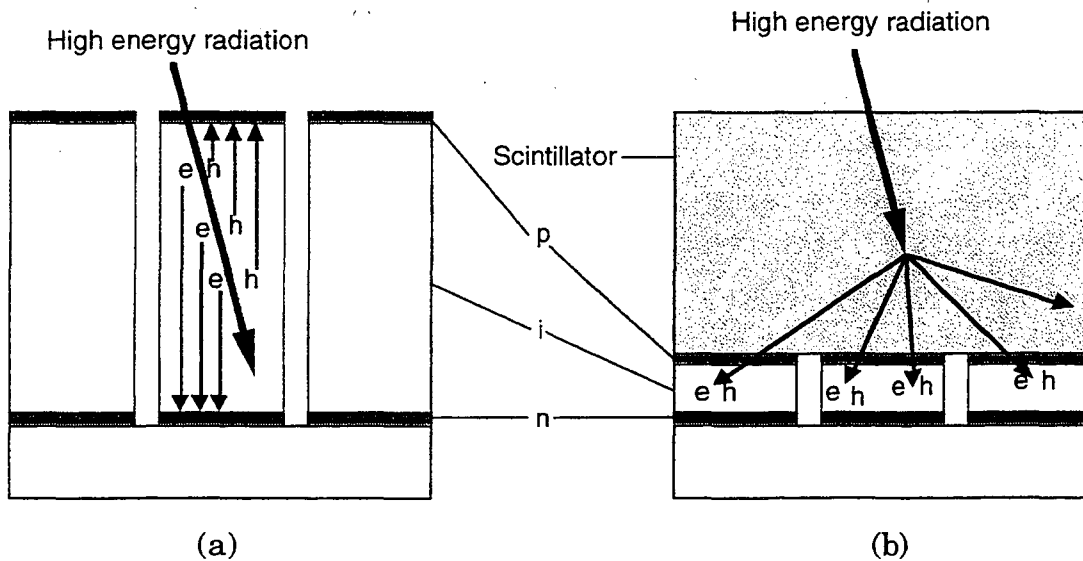
Fig. 2-1   Radiation detection schemes using a-Si:H p-i-n
photodiode pixel arrays: (a) direct detection and (b)
indirect detection.

array, because the position of interaction is confined in one pixel, hence the

pixel size determines the spatial resolution. Using direct detection scheme,

highly ionizing particles such as low energy protons and alpha particles

could be measured.[1,2]   For detection of minimum ionizing particles,

however, this scheme needs a thick i-layer due to the low stopping power of

a-Si:H.[4]   The average energy required to produce one electron-hole pair in

a-Si:H is 4.8 ± 0.3 eV, and the minimum ionizing particle generates about

80 electron-hole pairs per micron in a-Si:H.[5]   Therefore to detect the

minimum ionizing particles with an adequate signal to noise ratio, the

thickness of the i-layer should be at least 50 µm.[2,6]   Thick a-Si:H p-i-n

diodes have, however, problems with internal stress and high electric field

at the p-i interface.[7,8]   Due to the ionized defect density the electric field is

not uniform in the i-region of the a-Si:H p-i-n diode and is peaked at the p-i

interface.   Good collection efficiency requires full depletion of the i-region

12

and accordingly needs high reverse bias, which, if too high, causes pop-corn noise or breakdown of the diode. Many efforts on achieving high collection efficiency with low operation bias, such as using buried p-i-n structure, have been made.[9] Another possibility of low bias operation on a thick a-Si:H p-i-n diode is using photoconductive gain mechanism, which has, however, a higher shot noise due to large dark current level.[10] The photoconductive gain mechanisms in a-Si:H devices are discussed in Chapter 5.

2.1.2 Indirect Detection

An alternative scheme of radiation detection using a-Si:H p-i-n diode is the indirect detection. For indirect detection, a thin a-Si:H p-i-n diode is coupled to a scintillating layer which converts the energy deposited by charged particles, x-rays or γ-rays into visible light. As the mean free path of the visible light is short in a-Si:H a thin i-layer can be used. A 1 μm thick i-layer can absorb ~96% of the light incident on the p-i-n diode.[11] The scheme of indirect detection is shown in Fig. 2-1 (b). There are a number of advantages in indirect detection compared to direct detection, such as higher signal size, lower fabrication cost and time, lower bias operation and no stress problem. But this scheme has the disadvantages of a slower signal response, which is a function of the scintillator used, and poorer spatial resolution, due to the light spread in the scintillator. The thickness of the scintillator is 100 ~ 400 μm for x-ray detection and a few millimeters for γ-ray detection.[8,12] Choice of the scintillator depends on specific requirements of detection such as signal size, speed and spatial resolution.

There are many candidates of scintillator which can coupled to a-Si:H photodiodes. These include CsI(Tl), CsI(Na), $CdWO_4$, ZnS(Ni) and Gd_2O_2S:Tb (Kodak Lanex screen). Among these, CsI(Tl) has drawn much attention due to its high light yield (~52,000 photons/1 MeV absorbed energy) and a good emission spectrum that matches the a-Si:H photodiode quantum efficiency.[13,14] The emission spectrum of CsI(Tl) is compared with that of CsI(Na) and the quantum efficiency of a-Si:H photodiode in Fig. 2-2.[14] As the light yield of CsI(Tl) is high, the signal size from an a-Si:H p-i-n diode coupled to CsI(Tl) is higher than that from the p-i-n diode alone, as shown in Fig. 2-3.[14]
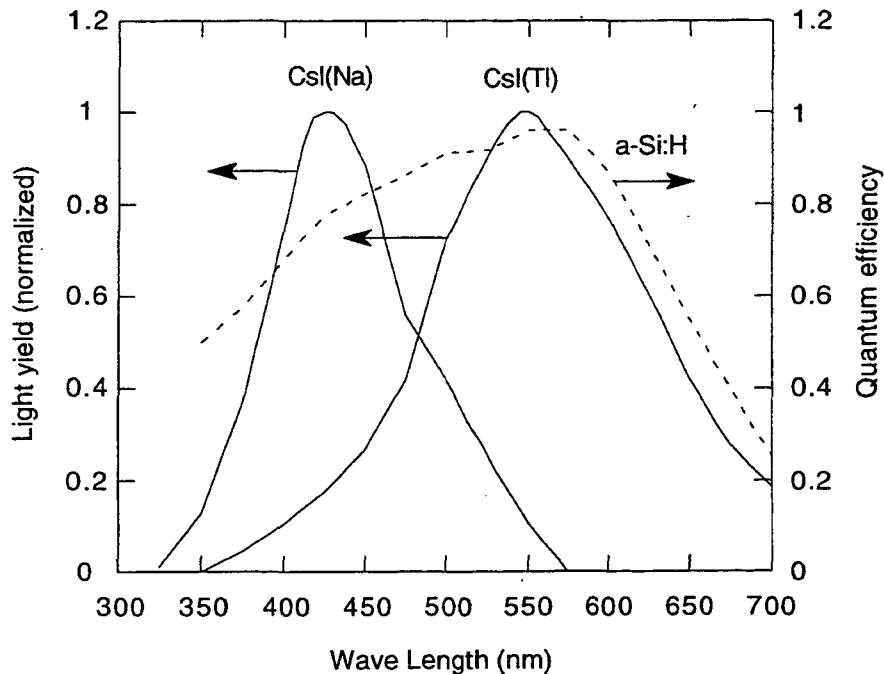
Fig. 2-2   Emission spectra of CsI(Tl) and CsI(Na), and the quantum efficiency spectrum of a-Si:H photo-diodes.[14]

14
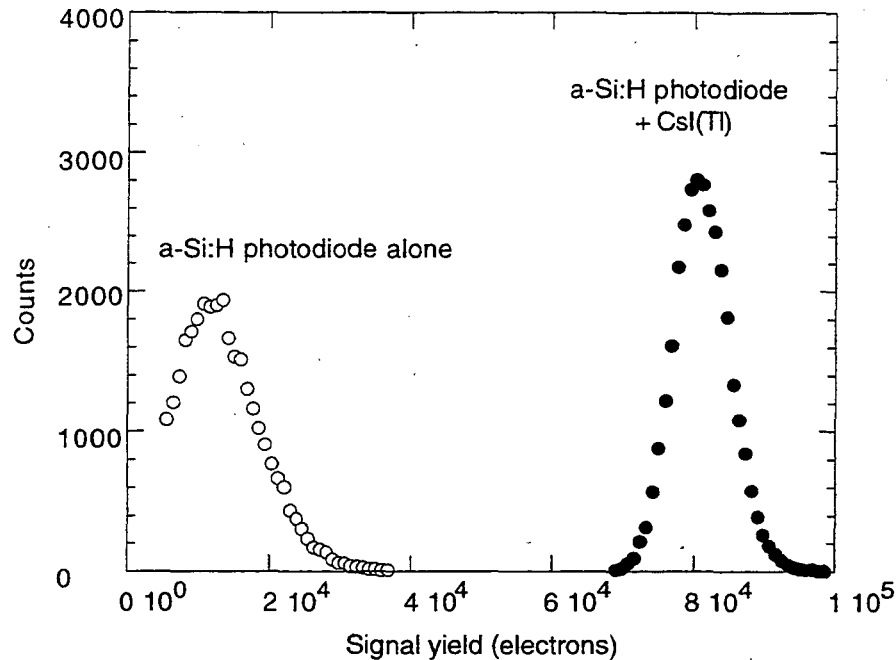
Fig. 2-3   Pulse height spectra obtained with a-Si:H photodiode alone and a-Si:H photodiode with CsI(Tl). The thickness of a-Si:H p-i-n diode is 10 μm and the thickness of CsI(Tl) is 233 μm. 2 μsec of x-ray pulse was used as a radiation source and the total radiation energy was ~22 MeV.[14]

2.2   Radiation Detection System

A conventional radiation detection system used with crystalline detectors[15] can also be used with a-Si:H radiation detectors, and is shown in Fig. 2-4. It consists of a low noise charge sensitive preamplifier, a shaping amplifier and a pulse height analyzer. The charge sensitive preamplifier receives the signal from the detector and produces a voltage output which is given by $V_o = Q_d/C_f$, where Q_d is the charge collected by the detector and C_f is the feedback capacitance of the charge sensitive preamplifier. This relationship is based on a large open loop gain of the charge sensitive amplifier. The shaping amplifier is composed of $CR-(RC)^n$

15
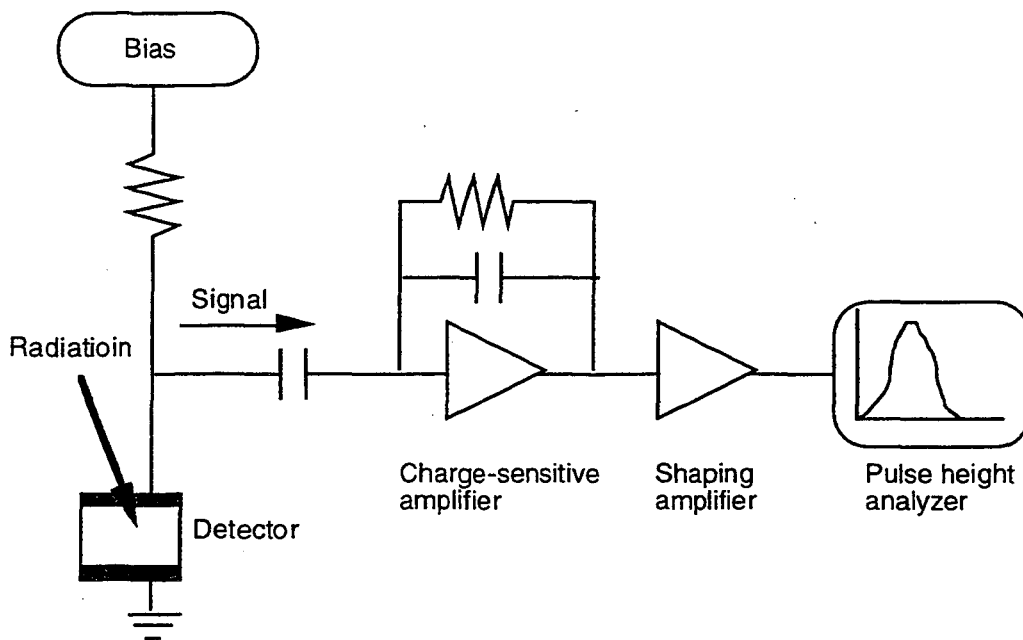
Fig. 2-4   Schematic diagram of a typical radiation detection
            system used with semiconductor radiation
            detectors.

network and produces a Gaussian pulse shape whose peak amplitude is
proportional to the preamplifier output voltage.

2.3   Properties of a-Si:H p-i-n Detectors

There are several parameters which determine the performance of
a-Si:H p-i-n diode as a radiation detector. These include mobility-lifetime
product and ionized dangling bond density, which are briefly discussed in
the following subsections. Details on these material properties are
intensively discussed in the literature.[3,16,17]

2.3.1 Mobility-Lifetime Product

The mobility-lifetime product ($\mu_d \tau$) of intrinsic a-Si:H determines the collection efficiency of the a-Si:H p-i-n detector, since the mean free path l of a charge carrier is given by

$$l = \frac{\mu_d \tau V}{d} \quad , \tag{2-1}$$

where V is the applied reverse bias and d is the thickness of the i-layer. Charge collection is complete when $l \gg d$, otherwise full collection is not possible. It is worth mentioning that the mobility and lifetime we consider here are the drift mobility and the total lifetime for deep trapping,[3] which are sometimes confused with the microscopic mobility and recombination lifetime obtained from steady state photoconductivity measurement.[16] The $\mu_d \tau$ values of electrons and holes in good quality intrinsic a-Si:H are $\sim 1 \times 10^{-7}$ cm^2/V and $\sim 2 \times 10^{-8}$ cm^2/V, respectively. The value of $\mu_d \tau$ is obtained from a time-of-flight (TOF) measurement. In a TOF experiment, a short light pulse of a strongly absorbed wavelength is incident on one side of the p-i-n diode under a condition of uniform electric field, and the charge carriers which drift across the sample along the electric field are measured. Due to deep trapping the collected charge Q is less than the initial light-generated charge Q_o, and is given by the famous Hecht equation:

$$\frac{Q}{Q_o} = \frac{\mu_d \tau V}{d^2} \left[1 - \exp\left(-\frac{d^2}{\mu_d \tau V} \right) \right] \quad . \tag{2-2}$$

From the measured dependence of Q and V the value of $\mu_d \tau$ is calculated.

17

An experimental system for the TOF measurement is schematically shown in Fig. 2-5. The pulse generator controls both the high voltage pulser and the N_2 laser with a slow repetition rate (< 1 Hz) in order to provide the sample with sufficient time for relaxation. In order that there be a uniform electric field in the sample when it is exposed to the laser light, the bias must be applied shortly before the light exposure so that the sample is not depleted. It takes usually more than 200 sec for full depletion at room temperature, but the initial depletion process is fast.[18] Hence, to ensure that little depletion occurs during the time interval between the onset of the bias and laser light exposure, the interval must be as short as possible. However, this time interval must be long enough to avoid the influence of RC transients on the measured signal. The time interval is controlled by the delay and is 50 ~ 200 μsec. A dye laser is used to control the wavelength of the light (~550 nm) incident on the sample and a neutral optical attenuator is used to control the light intensity. The light intensity should be low enough to avoid the distortion of the electric field by the photo-induced charge. The photodiode which is located between the dye laser and the optical attenuator detects the laser light and triggers the oscilloscope. The photo-induced signal from the a-Si:H sample is amplified and read by an oscilloscope which is connected to a PC for data analyses.

An electron Q-V plot of a 27 μm thick a-Si:H p-i-n diode obtained from a TOF measurement is shown in Fig. 2-6 as an example.[19] It shows an electron $\mu_d \tau$ value of 9.7 x 10^{-8} cm²/V.

Fig. 2-5 Schematic diagram of time-of-flight experimental system.

$\mu_d \tau = 9.7 \times 10^{-8} \ cm^2/V$

Fig. 2-6 A typical Q-V plot obtained from an electron TOF measurement.[19]

19

2.3.2 Ionized Dangling Bond Density

Good quality a-Si:H generally has a dangling bond density (defect density) of $10^{15} \sim 10^{16}$ cm^{-3}. When a reverse bias is applied on the a-Si:H p-i-n diode, about 30% of the dangling bonds in the i-region release electrons and become positively ionized .[17] This process is called depletion and the required bias V_f for the full depletion of the i-region is proportional to the ionized dangling bond density N_d^* and can be expressed as

$$V_f = \frac{qd^2 N_d^*}{2\varepsilon_{Si}} \quad , \tag{2-3}$$

where q is the charge of an electron, d is the thickness of the i-region and ε_{Si} is the dielectric constant of a-Si:H. The a-Si:H p-i-n detectors with lower N_d^*, therefore, need lower operating bias and have less problem with the high electric field at the p-i interface. The value of N_d^* can be obtained from the hole-onset measurement. In hole-onset measurement, a short pulse of strongly absorbing light is incident on the n-i interface under a dc reverse biased condition. When the bias is lower than the full depletion bias V_f, the electric field at the n-i interface is zero and the holes generated by the light cannot drift to the p-side, hence no signal is observed. When the bias is equal to or higher than V_f, the photo-induced holes can be collected as they drift along the electric field which is present across the whole region of the i-layer. Therefore, N_d^* can be calculated from the measured V_f using Eq. (2-3). A typical result of the hole-onset measurement on the a-Si:H p-i-n diode is shown in Fig. 2-7, which shows $V_f \approx 57$ V and corresponding $N_d^* \approx 4 \times 10^{14}$ cm^{-3}.
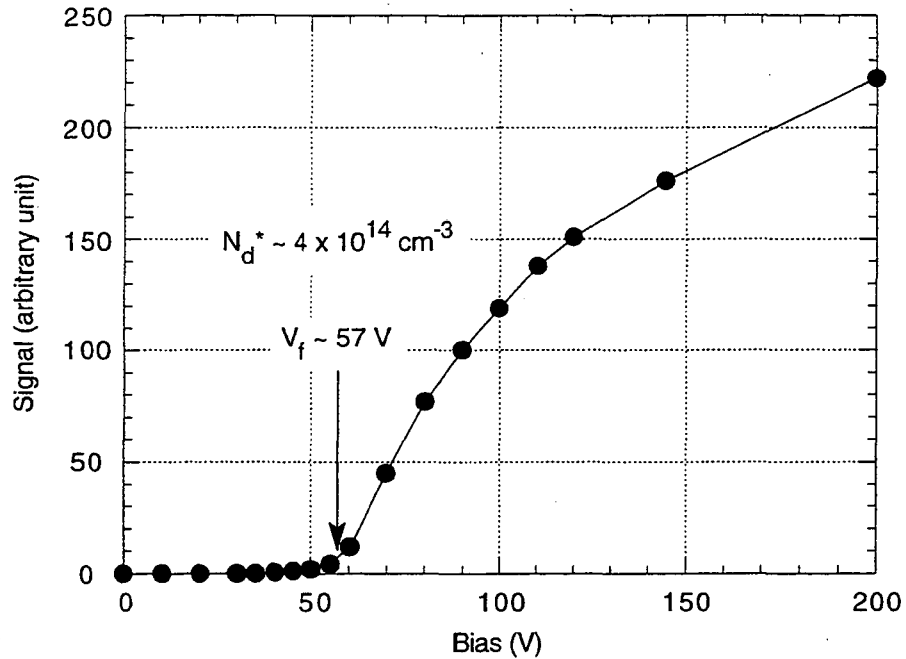
Fig. 2-7   Collected hole signal as a function of applied bias
            from a 14 μm thick p-i-n diode. Full depletion
            occurs at about 57 V.

2.4   Signal Generation in a-Si:H p-i-n Detectors

2.4.1 Surface Generation

a)   <u>P-side Generation</u>

When a point charge q moves a distance Δx during Δt along the electric field in the i-region of the a-Si:H p-i-n detector whose thickness is d, it induces current $i = q/d \cdot \Delta x/\Delta t$ in the external circuit.[20] Consider a certain amount of charge q_o which is generated at $x = 0$ (p-i interface). In this case, the signal is carried by electron transport only since the transit distance of holes is nearly zero. During the transit across the detector the

number of electrons decreases due to deep trapping. Therefore, the remaining charge $q(t)$ at a certain time t, which is less than the transit time, is

$$q(t) = q_o e^{-t/\tau_e} \quad , \tag{2-4}$$

where τ_e is the total lifetime of an electron for deep trapping which can be obtained from the TOF experiment as discussed in Section 2.3.1. The induced current $i(t)$ is then given by

$$\begin{aligned} i(t) &= \frac{q(t)}{d} \frac{\Delta x}{\Delta t} \\ &= \frac{q_o}{d} e^{-t/\tau_e} \mu_d E(x) \quad , \end{aligned} \tag{2-5}$$

where $E(x)$ is the position dependent electric field. The collected signal charge Q_{sig} can be calculated by integrating Eq. (2-5) over either a measurement time t_m or the transit time t_r whichever is shorter. When the electric field $E(x)$ is uniform such as in TOF experiment, Q_{sig} can be obtained from the Hecht equation. In actual operation of a-Si:H p-i-n detectors with a dc bias, the electric field is not uniform due to the positive space charge, and the expression of Q_{sig} is different whether the detector is fully depleted or not. In the case of partial depletion,[19]

$$Q_{sig} = q_o \lambda \frac{1 - e^{-\beta_e t_m}}{\alpha_e \beta_e} \quad , \tag{2-6}$$

where α_e and $1/\beta_e$ are the electron characteristic times defined by

$$\begin{aligned} \alpha_e &= \frac{\varepsilon_{Si}}{q N_d^* \mu_d^e} \quad , \\ \beta_e &= \frac{\alpha_e + \tau_e}{\alpha_e \tau_e} \quad , \end{aligned} \tag{2-7}$$

and λ is the ratio of the depletion width to the diode thickness,

$$\lambda = \frac{1}{d}\sqrt{\frac{2\varepsilon_{Si}V}{qN_d^*}} \quad . \tag{2-8}$$

When the detector is fully depleted,

$$Q_{sig} = q_o\left(\frac{1+\lambda^2}{2}\right)\frac{1-e^{-\beta_e t^*}}{\alpha_e\beta_e} \quad , \tag{2-9}$$

where t^* is the shorter one of t_m or t_r.

b)   N-side Generation

This is the case when a strongly absorbing light pulse is incident on the n-side of the p-i-n diode as in the hole-onset experiment, and the signal is formed by hole transport.

i)   Partial depletion

When the diode is not fully depleted, the holes generated in the n-i interface region cannot move because no electric field exist in that region, as discussed in Section 2.3.2. Therefore, no signal charge is collected.

ii)   Full depletion

By the similar procedure as in the case of p-side generation, the collected signal charge is[19]

$$Q_{sig} = q_o\left(\frac{\lambda^2-1}{2}\right)\frac{1-e^{-\beta_h t^*}}{\alpha_h\beta_h} \quad , \tag{2-10}$$

23

where

$$\alpha_h = \frac{\varepsilon_{Si}}{q N_d^* \mu_d^h} \quad ,$$

$$\beta_h = \frac{\alpha_h + \tau_h}{\alpha_h \tau_h} \quad ,$$

(2-11)

μ_d^h is the hole drift mobility, τ_h is the hole deep trapping and t^* is the shorter one of the measurement time or the transit time. The measured collection efficiency (Q_{sig}/q_o) of electrons and holes in the case of surface generation is shown in Fig. 2-8 together with the calculated results using the above equations.[19] It is shown in the graph that the hole signal becomes noticeable at a reverse bias of ~350 V which is the full depletion bias of this 27 μm thick p-i-n diode.
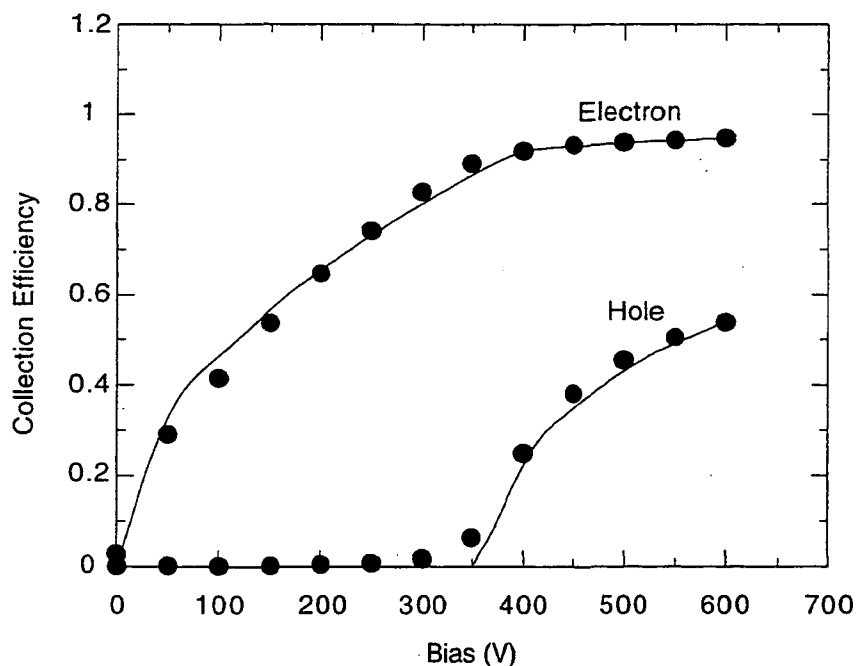
Fig. 2-8   Collection efficiencies of electrons and holes in the case of surface generation of charge carriers. Solid circles represent measurements and curves represent calculations.[19]

24

2.4.2 Uniform Generation

When the photo-induced charge is uniform across the diode, both electrons and holes contribute to the signal formation. For each type of carrier the induced current can be obtained by integrating the expression in Eq. (2-5) over the whole thickness of the i-region, and the signal charge is obtained by an integration of this current over the measurement time.

i)   Partial depletion

$$
\begin{aligned}
Q_{sig} &= Q_{sig}^{e} + Q_{sig}^{h} \\
&= \frac{\lambda^2}{2}\left(\frac{1-e^{-\beta_e t_m}}{\alpha_e \beta_e} + \frac{1-e^{-\beta_h t_m}}{\alpha_h \beta_h} \right)
\end{aligned}
\tag{2-12}
$$

ii)   Full depletion

$$
Q_{sig} = \frac{1}{8}\left[\left(\lambda^2 + 1\right)^2 \left(\frac{1-e^{-\beta_e t_m}}{\alpha_e \beta_e} + \frac{1-e^{-\beta_h t_m}}{\alpha_h \beta_h} \right) \right.
$$
$$
\left. -\left(\lambda^2 - 1\right)^2 \left(\frac{1-e^{-\gamma_e t_m}}{\alpha_e \gamma_e} + \frac{1-e^{-\gamma_h t_m}}{\alpha_h \gamma_h} \right) \right] ,
\tag{2-13}
$$

where $\gamma_e = \dfrac{\alpha_e - \tau_e}{\alpha_e \tau_e}$ and $\gamma_h = \dfrac{\alpha_h - \tau_h}{\alpha_h \tau_h}$.

The collection efficiencies for the uniform generation case are shown in Fig. 2-9 as a function of reverse bias.[19]   The calculated results are compared with the measurements.
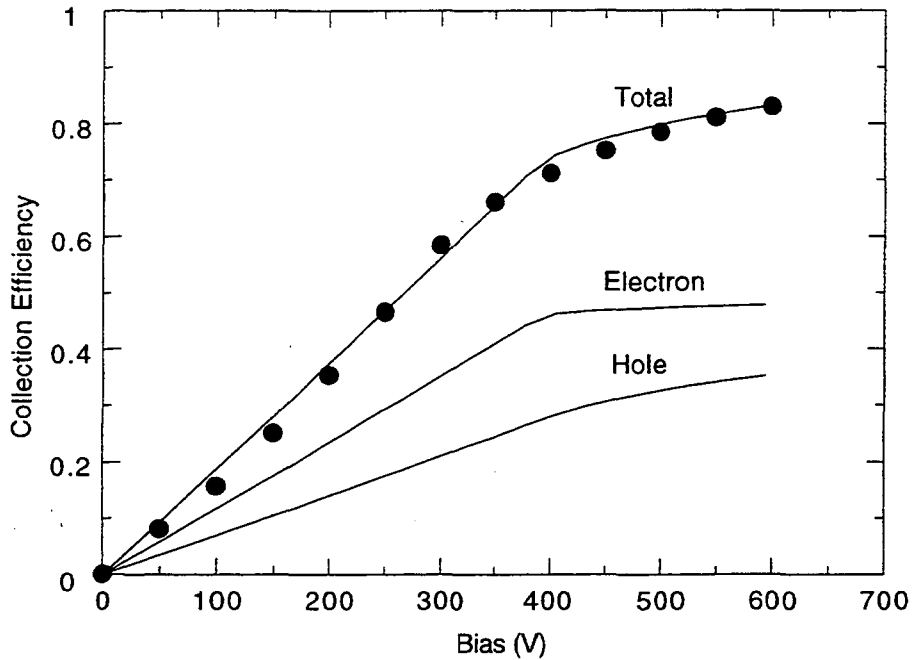
Fig. 2-9   Collection efficiencies in the case of uniform generation of charge carriers. Solid circles represent measured total collection efficiency and curves represent calculations.[19]

2.5   X-Ray Imaging with a-Si:H Detector Arrays

Utilizing the advantage of large area fabrication, a-Si:H has recently been investigated for x-ray imaging.[21-30] The imaging arrays made from a-Si:H may replace the x-ray films or image intensifying tubes in radiography. The images obtained by a-Si:H arrays are digital images, hence have many advantages over the conventional x-ray films, such as digital image processing, computer storage and communication through PACS. It was also reported that using a-Si:H imaging arrays tomographic imaging was possible.[24]

A-Si:H x-ray imaging arrays developed so far use the indirect detection scheme which is described in Section 2.1.2. Fig. 2-10 (a) and (b) show the schematic diagram of a-Si:H x-ray imaging array structure and
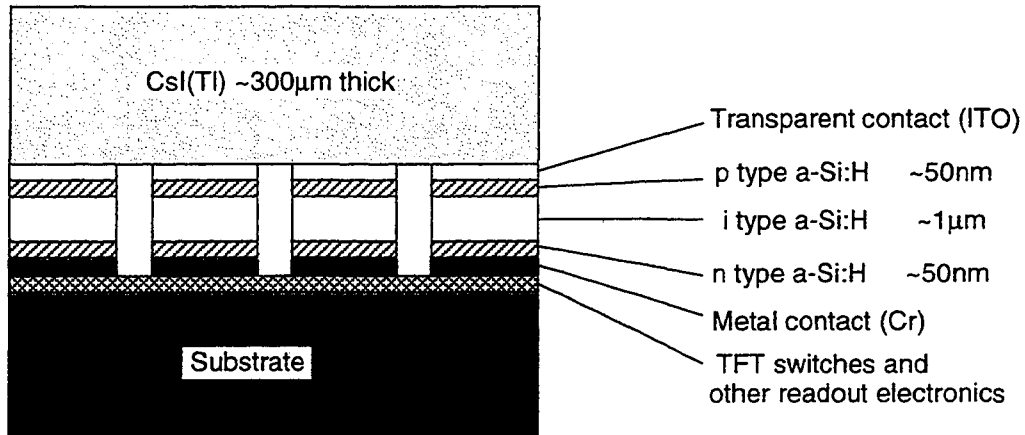
(a)
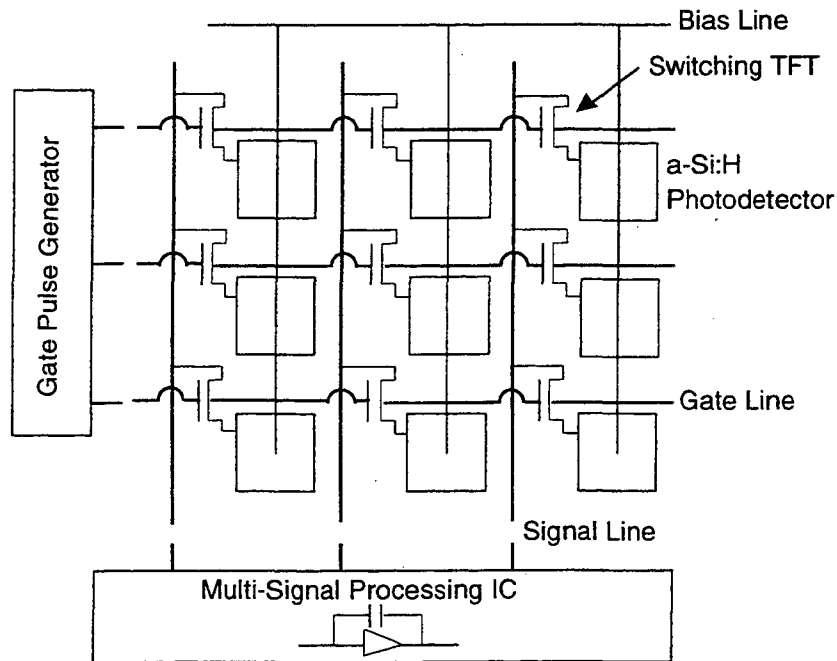
(b)

Fig. 2-10   Schematic diagrams of (a) a-Si:H detector array
            structure and (b) readout electronics for x-ray
            imaging.   Four pixels are shown in (a), and nine
            pixels are drawn in (b).

27

readout electronics. Each pixel is composed of a thin (~ 1 μm) a-Si:H p-i-n photodiode, and is connected to a switching TFT which can be made of either a-Si:H or polycrystalline silicon. The gate contact of the switching TFTs along a row are connected to a common gate line, and the drain contact of the TFTs along a column are connected to a common signal line. The gate pulse generator applies a sequential pulse to the TFTs in a row, and the addressed a-Si:H p-i-n photodiodes send the stored signal charge to an external multi-signal processor through TFTs and signal lines in a row. The photodiodes in other rows which have not addressed yet retain the signal charge until they are addressed by a gate pulse generator. The signal charge is stored on the pixel by the intrinsic capacitance of the photodiode and the off-resistance of the TFT. The actual a-Si:H imaging array developed by Xerox company for x-ray imaging is shown in Fig. 2-11,[27] and diagnostic x-ray images obtained with this array in conjunction with a Kodak Lanex Fast B screen (Gd_2O_2S:Tb) are shown in Fig. 2-12.[23,26] The array is composed of 512x560 pixels of a-Si:H p-i-n photodiodes and a-Si:H TFTs with a pixel pitch of 450 μm.

There are a few characteristics which represent the performance of a-Si:H based x-ray imaging arrays. These include linearity of pixel response, image lag, frame rate and noise, which determine the operation conditions of the imaging arrays. The linearity of the pixels has been shown to be good (within ~1%) at low signal levels, and as the operation bias increases the fraction of linear signal range increases up to more than 85% of the full signal range.[28] Image lag and frame rate are influenced by the characteristics of charge transfer during readout. Image lag is due
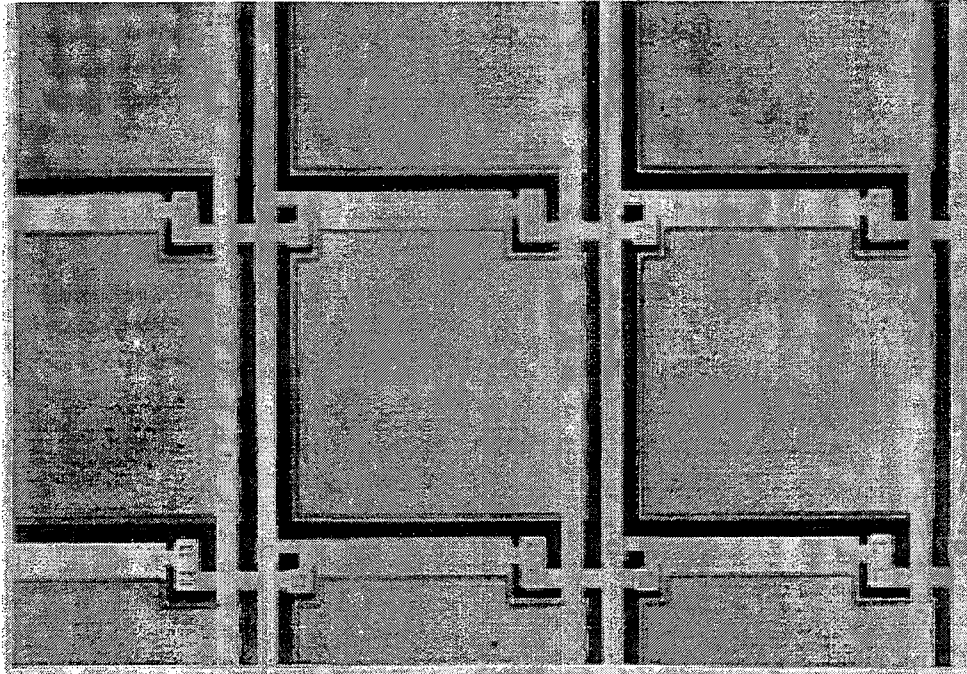
Fig. 2-11   Picture of an x-ray imaging array based on a-Si:H
p-i-n photodiodes and a-Si:H TFTs made by Xerox.
The pixel pitch is 450 μm.   Signal lines run
vertically over the left-hand side of the pixels and
the gate lines run horizontally over the top side of
pixels. A TFT is fabricated on the top side of each
pixel. The vertical lines over the right-hand side of
the pixels are for biasing.[27]

to incomplete charge transfer from the photodiodes to the external circuit

and/or slow release of trapped charge in the photodiodes. The image lag

increases as the light intensity increases, and decreases as the operation

bias increases.[27]   High frame rate also reduces the image lag.[29]   The

frame rate is limited by various factors such as array size, operation voltage

and pixel reinitialization properties. A theoretical value of 30 fps (frame

per second) was achieved for pixel arrays with 30x30 cm^2 area and 100 μm

pixel pitch.[29]   The dominant noise source of imaging arrays is the

thermal noise due to the on-state resistance of the switching TFT. The 1/f

noise and shot noise from a-Si:H p-i-n diode can be neglected since the dark
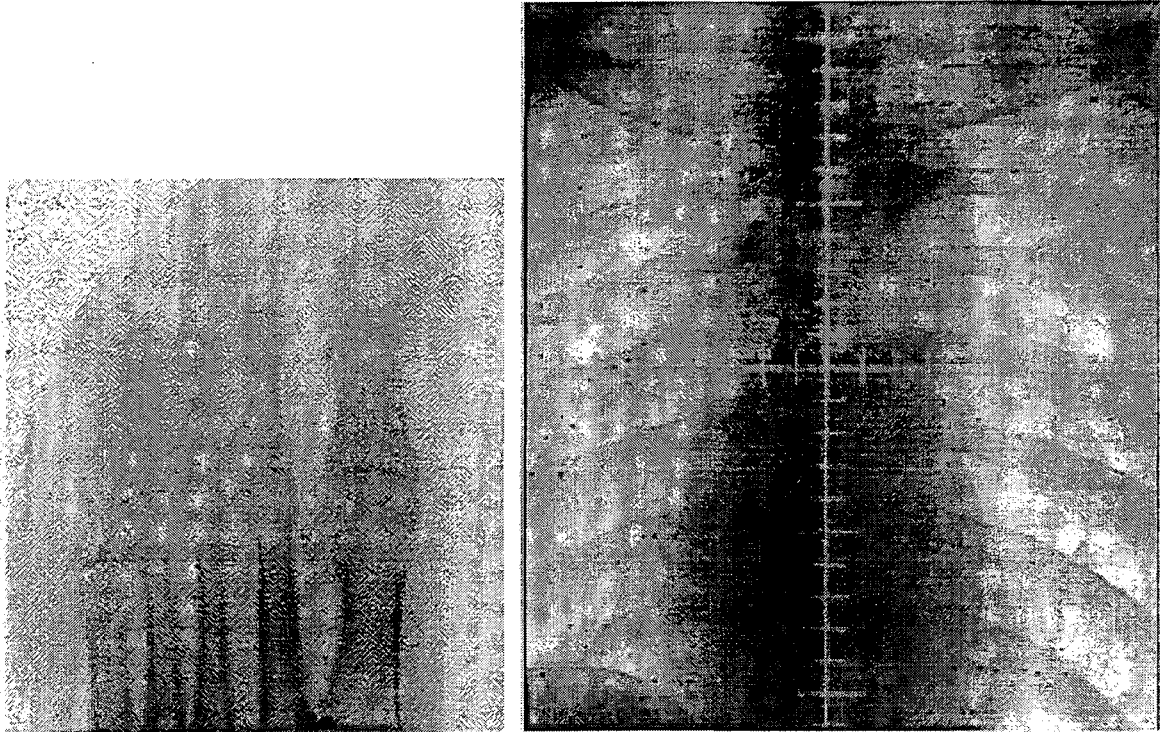
Fig. 2-12   diagnostic x-ray images obtained with the a-Si:H
x-ray imaging arrays shown in Fig. 2-11. X-ray
irradiation conditions were 65 ~ 75 kVp and 0.75 ~
10 mAsec. The a-Si:H imaging array in Fig. 2-11
was used in conjunction with a Kodak Lanex Fast
B screen (Gd_2O_2S:Tb).[23,26]

current level of the pixels is low during the operation.[30] The TFT thermal
noise is approximately proportional to the square root of the photodiode
capacitance, and from an array with 450 μm pixel pitch about 6,000
electrons rms of noise level was measured.[27] In Table 2-1, design
specifications and performance characteristics of a-Si:H based x-ray
imaging arrays made by Xerox company are listed.[27]

Table 2-1   Examples of design specifications and performance characteristics of large area x-ray imaging arrays based on a-Si:H which were manufactured by Xerox.[27]

	1992	1994
Design specifications		
Number of pixels	512 x 560	1536 x 1920
Pixel pitch	450 μm	127 μm
Array dimension	23.0 x 25.2 cm^2	19.5 x 24.4 cm^2
TFT dimension (width x length)	240 x 15 μm^2	20 x 11 μm^2
Performance characteristics		
Linearity	within ~ 1%	within ~ 1%
Image lag	< 5%	< 5%
Maximum frame rate	~ 20 fps	10 ~ 30 fps
Pixel noise	~ 1.0 fC	< 0.25 fC
Dynamic Range	~ 50,000	> 10,000

References

[1]   V. Perez-Mendez, J. Morel, S. N. Kaplan and R. A. Street, "Detection of Charged Particles in Amorphous Silicon Layers," Nucl. Instr. and Meth., 252, 478 (1986)

[2]   V. Perez-Mendez, S. N. Kaplan, W. Ward, S. Qureshi, and R. A. Street, "Signal, Recombination Effects and Noise in Amorphous Silicon Detectors," Nucl. Instr. and Meth., A260, 195 (1987)

[3]   R. A. Street, *Hydrogenated Amorphous Silicon*, Cambridge University Press, Cambridge (1991)

[4]   S. N. Kaplan, I. Fujieda, V. Perez-Mendez, S. Qureshi, W. Ward and R. A. Street, "Detection of Minimum-Ionizing Particles in Hydrogenated Amorphous Silicon," Nucl. Instr. and Meth., A273, 611 (1988)

[5]   V. Perez-Mendez, G. Cho, J. S. Drewery, T. Jing, S. N. Kaplan, S. Qureshi, D. Wildermuth, I. Fujieda and R. A. Street, "Amorphous Silicon Based Radiation Detectors," J. Non-Cryst. Solids, 137&138, 1291 (1991)

[6]   V. Perez-Mendez, G. Cho, I. Fujieda, S. N. Kaplan, S. Qureshi and R. A. Street, "The Application of Thick Hydrogenated Amorphous Silicon Layers to Charged Particle and X-Ray Detection," Mat. Res. Soc. Symp. Proc. 149, 621 (1989)

[7]   V. Perez-Mendez, S. N. Kaplan, G. Cho, I. Fujieda, S. Qureshi, W. Ward and R. A. Street, "Hydrogenated Amorphous Silicon Pixel Detectors for Minimum Ionizing Particles," Nucl. Instr. and Meth., A273, 127 (1988)

[8]   V. Perez-Mendez, "Charged Particle, Gamma Ray, and Light Detection in Amorphous Silicon Devices," Chapter 8 in *Amorphous & Microcrystalline Semiconductor Devices*, edited by J. Kanicki, Artech House, Boston (1991)

[9]   I. Fujieda, G. Cho, M. Conti, J. S. Drewery, S. N. Kaplan, V. Perez-Mendez, S. Qureshi and R. A. Street, "Improved Charge Collection of the Buried p-i-n a-Si:H Radiation Detectors," IEEE Tran. Nucl. Sci., 37, 124 (1990)

[10]   H. K. Lee, J. S. Drewery, W. S. Hong, T. Jing, S. N. Kaplan and V. Perez-Mendez, "Utilization of Photoconductive Gain in a-Si:H Devices for Radiation Detection," To be presented at MRS Meeting at San Francisco in April (1995)

[11]   H. K. Lee, G. Cho, J. S. Drewery, W. S. Hong, T. Jing, S. N. Kaplan, A. Mireshghi, V. Perez-Mendez and D. Wildermuth, "New a-Si:H Photo-Detectors for Long-Term Charge-Storage," Mat. Res. Soc. Symp. Proc., 297, 1023 (1993)

[12]   H. K. Lee, J. S. Drewery, W. S. Hong, T. Jing, S. N. Kaplan, A. Mireshghi and V. Perez-Mendez, "Hydrogenated Amorphous Silicon (a-Si:H) Based Gamma Camera - Monte Carlo Simulations," SPIE Vol. 2163, Medical Imaging 1994: Physics of Medical Imaging, 427 (1994)

[13]   I. Holl, E. Lorenz and G. Mageras, "A Measurement of the Light Yield of Common Inorganic Scintillators," IEEE Trans. Nucl. Sci., 35, 105 (1988)

[14]   I. Fujieda, G. Cho, J. S. Drewery, T. Gee, T. Jing, S. N. Kaplan, V. Perez-Mendez, D. Wildermuth and R. A. Street, "X-ray and Charged Particle Detection with CsI(Tl) Layer Coupled to a-Si:H Photodiode Layers," IEEE Trans. Nucl. Sci., NS-38, 255 (1991)

[15]   G. F. Knoll, *Radiation Detection and Measurement*, John Wiley & Sons, New York (1979)

[16]   R. S. Crandall, "Photoconductivity," Chapter 8 in *Semiconductors and Semimetals*, Vol. 21, Part B, edited by J. I. Pankove, Academic Press, Inc., Orlando (1984)

[17] S. Qureshi, V. Perez-Mendez, S. N. Kaplan, I. Fujieda, G. Cho and R. A. Street, "Material Parameters in a Thick Hydrogenated Amorphous Silicon Detector and Their Effect on Signal Collection," Mat. Res. Soc. Symp. Proc., 149, 649 (1989)

[18] R. A. Street, "Long-Time Transient Conduction in a-Si:H p-i-n Devices," Philo. Mag. B, 63, 1343 (1991)

[19] G. Cho, "Signal and Noise Analysis of a-Si:H Radiation Detector-Amplifier System," Ph.D. Thesis, UC Berkeley (1992)

[20] P. A. Tove and K. Falk, "Pulse Formation and Transit Time of Charge Carriers in Semiconductor Junction Detectors," Nucl. Instr. and Meth., 29, 66 (1964)

[21] I. Fujieda, S. Nelson, P. Nylen, R. A. Street and R. L. Weisfield, "Two Operation Modes of 2D a-Si Sensor Arrays for Radiation Imaging," J. Non-Crystalline Solids, 137&138, 1321 (1991)

[22] I. Fujieda, S. Nelson, R. A. Street and R. L. Weisfield, "Radiation Imaging with 2D a-Si Sensor Arrays," IEEE Trans. Nucl. Sci., NS-39, 1056, (1992)

[23] L. E. Antonuk, J. Yorkston, W. Huang, J. Boudry, E. J. Morton and R. A. Street, "Large Area Flat-Panel a-Si:H Arrays for X-ray Imaging," SPIE Vol. 1896, Medical Imaging 1993: Physics of Medical Imaging, 18 (1993)

[24] N. H. Clinthorne, "Are Hydrogenated Amorphous Silicon Arrays Usable for Tomographic Imaging?," IEEE Trans. Nucl. Sci., 41, 1516 (1994)

[25] R. A. Street, S. Nelson, L. Antonuk and V. Perez-Mendez, "Amorphous Silicon Sensor Arrays for Radiation Imaging," Mat. Res. Soc. Symp. Proc., 192, 441 (1990)

[26] L. E. Antonuk, J. Boudry, W. Huang, D. L. McShan, E. J. Morton, J. Yorkston, M. J. Longo and R. A. Street, "Demonstration of

Megavoltage and Diagnostic X-Ray Imaging with Hydrogenated Amorphous Silicon Arrays," Med. Phys., 19, 1455 (1992)

[27] L. E. Antonuk, J. Boudry, Y. El-Mohri, W. Huang, J. Siewerdsen, J. Yorkston and R. A. Street, "A High Resolution, High Frame Rate, Flat-Panel TFT Array for Digital X-Ray Imaging," SPIE Vol. 2163, Medical Imaging 1994: Physics of Medical Imaging, 118 (1994)

[28] J. Yorkston, L. E. Antonuk, W. Huang and R. A. Street, "Photoresponse Linearity of a-Si:H Imaging Pixels," Mat. Res. Soc. Symp. Proc., 297, 951 (1993)

[29] L. E. Antonuk, J. Yorkston, W. Huang, J. Siewerdsen and R. A. Street, "Considerations for High Frame Rate Operation of Two-Dimensional a-Si:H Imaging Arrays," Mat. Res. Soc. Symp. Proc., 297, 945 (1993)

[30] I. Fujieda, R. A. Street, R. L. Weisfield, S. Nelson, P. Nylen, V. Perez-Mendez and G. Cho, "High Sensitive Readout of 2D a-Si Image Sensors," Jpn. J. Appl. Phys., 32, 198 (1993)

Chapter 3 a-Si:H Based Gamma Camera

3.1 Introduction

In parallel with x-ray imaging of human anatomy, imaging physiological function using radiation emanating from inside the human body has become a useful method in clinical diagnosis of human disease. In radioisotope imaging the distribution of radionuclide-labeled agents, known as radiopharmaceuticals, is measured using an imaging instrument which is called a gamma camera. Fig. 3-1 shows a schematic view of radioisotope imaging technique and a planar scintigraphy of normal thyroid function obtained by use of a gamma camera[1] is shown in Fig. 3-2. In the following, the structure and operation principles of the conventional gamma camera is briefly described.
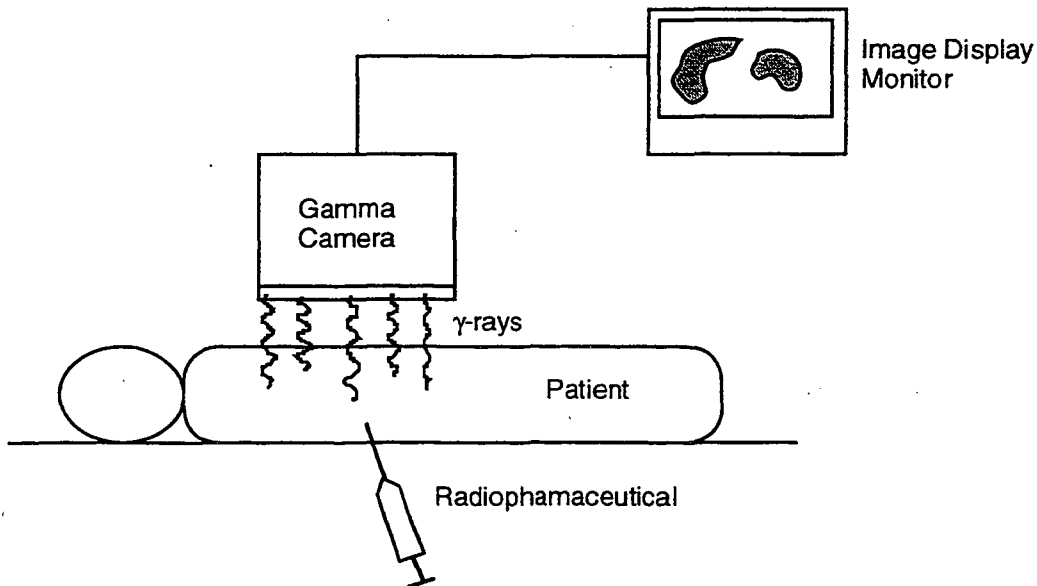
Fig. 3-1   Schematic view of radioisotope imaging technique.
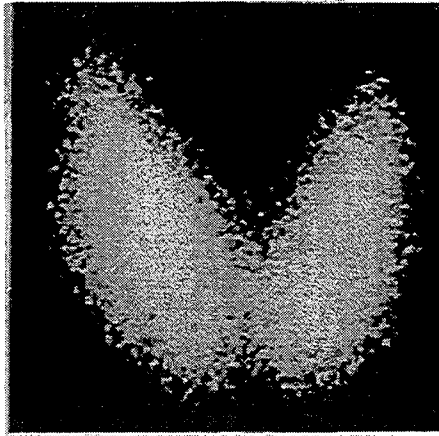
Fig. 3-2   Scintigraphy of a normally functioning thyroid
gland using ^{99m}Tc.

A conventional gamma camera consists of a multihole collimator, NaI(Tl) crystal as a scintillator, light guides, hexagonal array of photomultipliers and electronics for position encoding and pulse-height analysis as shown in Fig. 3-3. The whole is shielded by a lead container in order to minimize background which is due to the radiation which comes from outside the field of view of the camera.
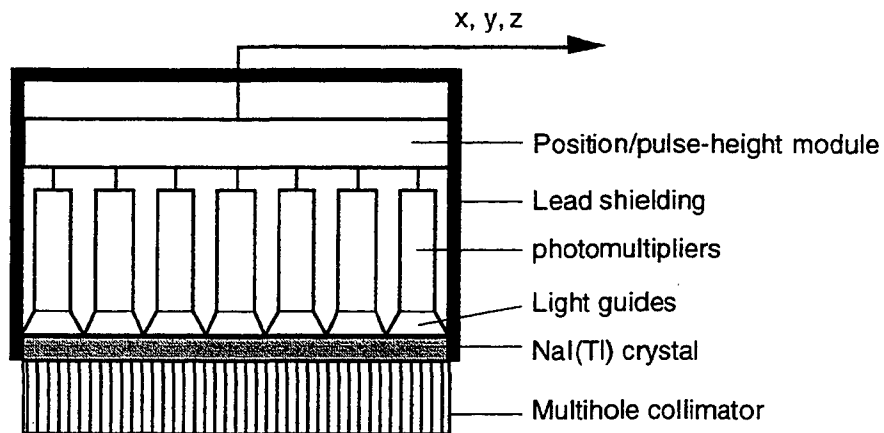
Fig. 3-3   The basic components of a conventional gamma
camera. A gamma camera provides information of
the position of γ event in the NaI(Tl) crystal (x,y) and
the γ energy (z).

37

The purpose of a collimator is to allow γ-rays originating from a selected area of an organ to reach a selected area of the camera. Thus a collimator establishes a one to one correspondence between different locations on the camera and those within the organ. The collimator also defines the geometrical field of view of the camera and essentially determines both the spatial resolution and sensitivity of the camera. Four types of collimators have been used with gamma cameras: pinhole, parallel hole, converging and diverging collimators. The choice of a particular type of collimator is basically determined by the size of the body region to be imaged and the desired resolution. For imaging organs which are similar in size to that of the camera, parallel hole collimators produce best images. For organs whose size is larger than that of the camera, diverging collimators are preferred. Converging collimators and pinhole collimators are appropriate for imaging small organs. Many of the gamma cameras in use have a large-area single crystal NaI(Tl) as a scintillator. This scintillator emits a visible light spectrum with a emission peak of 415 nm, which matches well the photon response spectrum of the photocathodes in bialkali photo-multipliers. Due to the high refractive index of NaI(Tl) (1.85) a light guide is usually used for good light transmission from NaI(Tl) to the photomultipliers. It is a transparent plastic with a refractive index close to that of NaI(Tl) and shaped to match the shape of the photomultiplier cathode. The photomultipliers are closely packed in the form of a hexagonal array containing 7, 19, 37, 61, and so on as shown in Fig. 3-4. The light from the crystal is divided among the hexagonal arrays of photomultiplier tubes. The position encoding electronics determines the position of the event in the scintillator by a centroid calculation which is
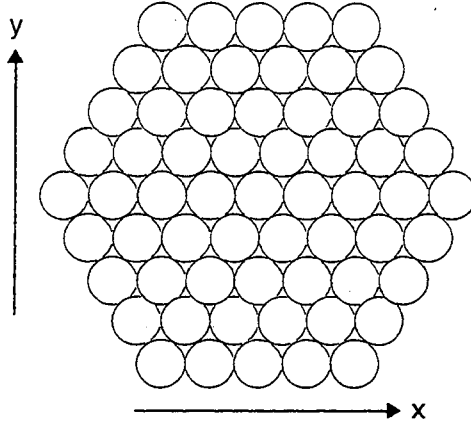
Fig. 3-4   The hexagonal arrangement of 61 photomultiplier
array in a typical gamma camera.

sometimes referred to as 'Anger logic'.[2]   The estimate of the x and y coordinates of the event, $\hat{x}$ and $\hat{y}$, are given by

$$\hat{x} = \frac{\sum_i x_i n_i}{\sum_i n_i}$$

and

$$\hat{y} = \frac{\sum_j y_j n_j}{\sum_j n_j}$$

where x_i and y_i are the x and y coordinates of the center of the photomultipliers and, n_i and n_j are the number of light photon counts or the pulse amplitudes in each photomultiplier.   The intrinsic spatial resolution of the camera is determined by the accuracy of the position computation rather than the number of discrete detectors and is limited by the counting statistics of the number of light photons at each photomultiplier, hence is a function of the γ-ray energy.   Generally this resolution is proportional to $1/\sqrt{E}$, where E is the γ-ray energy.[3]   The

intrinsic resolution of modern gamma cameras is typically 3~4 mm.[1] The z-signal, which is proportional to the total amount of light produced by a scintillation event in the crystal, hence is proportional to γ energy, is obtained by summing all the output signals from each photomultiplier, and is sent to the pulse height analyzer for energy selection to achieve scatter rejection. If the pulse height of the z-signal fails to fall within prescribed limits for the γ-ray energy of the isotope used, the pulse is rejected.

In the following sections conceptual design of a-Si:H based gamma cameras and Monte Carlo simulations on these devices, in order to investigate their feasibility, are described. Experimental results with the test devices for the a-Si:H based gamma camera are discussed in Chapter 4.

3.2   a-Si:H Based Gamma Cameras

Using similar technologies of a-Si:H imaging arrays developed for x-ray imaging as discussed in Chapter 2, radioisotope imaging in nuclear medicine with a-Si:H detector arrays may be possible. The proposed cameras would have a similar detection scheme except that the photomultiplier array and position encoding circuitry are replaced by a 2-D pixel photodetector array made of a-Si:H and thin film transistor (TFT) readout circuitry(Fig. 3-5).[4] The photodetector array and readout circuitry can be built on the same substrate and the thickness is a few mm at most, hence this camera would have less volume and weight than a conventional gamma camera.

Conventional   **Using a-Si:H**
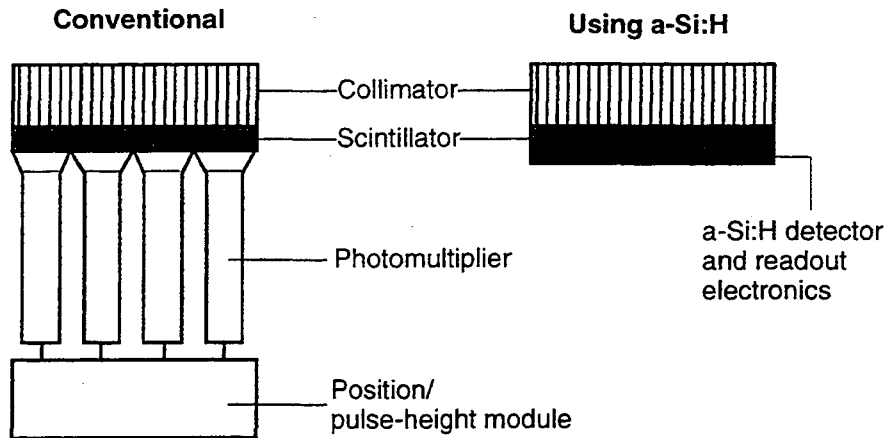
Fig. 3-5   Schematic diagram showing different structures of
a conventional gamma camera and an a-Si:H based
gamma camera. The a-Si:H parts in the a-Si:H
based gamma camera replace the photomultiplier
array and position sensing electronics in a
conventional gamma camera.

The main role of the photomultipliers in conventional gamma
cameras is to achieve a high signal from a single event in a scintillator
crystal by means of the gain mechanism inside the tubes. An a-Si:H based
gamma camera also needs a method to increase the signal from the
scintillator up to a measurable size, otherwise, the signal from a single
event would be embedded in the noise. There are two different methods to
solve this problem. One is to build an amplifier under each pixel
photodetector so that the signal from the pixel detector is amplified such as
in the photomultiplier tube (Type A). The other is to store the signal from
each event on a pixel itself by use of an additional storage capacitor attached
to the photodetector until the accumulated signal is big enough to be
measured (Type B). The structures and operation schemes of these two
types of a-Si:H based gamma camera are discussed in the following two
subsections.

41

3.2.1 Type A: a-Si:H Photodetector with Pixel Amplifier

a)   Structure

The structure of the type A camera is shown in Fig. 3-6. The same collimators for the conventional gamma cameras can also be used in a-Si:H based camera. As a scintillator CsI(Tl) is a good choice since it is the most appropriate with a-Si:H photodetectors as discussed in Chapter 2. The only difference in CsI(Tl) for x-ray imaging and γ-ray imaging is its thickness. In x-ray imaging, such as mammography, the spatial resolution is important so the scintillator should be thin enough to minimize the light spread inside the scintillator. Some of the x-rays, in this case, will be lost by penetrating the thin scintillator, but as the x-ray photons are incident in a form of a flux the signal size is big enough and the sensitivity of the scintillator is not a big problem. In γ-ray imaging, however, we have to collect a signal from a single event of γ-ray in the scintillator, hence the
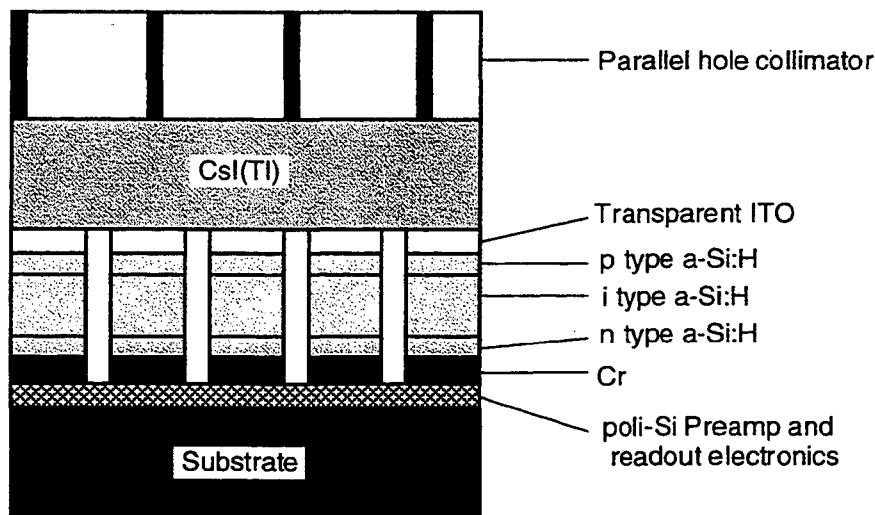
Fig. 3-6   Cross sectional diagram of type A a-Si:H gamma camera. 5 pixels of a-Si:H photodetectors are shown. Drawing scale is arbitrary.

42

scintillator should be thick enough not to miss the incoming single γ-ray. The intrinsic spatial resolution, of course, is worse than the case of x-ray imaging due to increased light spread in the scintillator, but as the total spatial resolution is mainly determined by the collimator, thicker scintillators than those in x-ray imaging devices can be used unless it affects the total spatial resolution significantly. Nevertheless, for a higher intrinsic spatial resolution, the scintillating crystal can be segmented and the gaps filled with light reflecting or absorbing material. The effect of the scintillator thickness on spatial resolution will be discussed in detail in Section 3.3. The structure of the photodetector is the same as in the x-ray imaging array, that is, an a-Si:H p-i-n photodiode with transparent top contact and metal layer for a bottom contact. The thickness of the intrinsic layer is ~1 μm, which is thick enough to absorb ~96% of the light incident on the photodiode.[5]

Each pixel of the a-Si:H photodetector is connected to the input node of a charge-sensitive pixel amplifier. This pixel amplifier is built beneath each photodetector so that the photodetector can have high fill factor on the imaging area. The constraints on the design of the pixel amplifier are as follows: (a) size of the amplifier should fit that of the pixel photodetector, (b) moderate gain in order to avoid external pickup or cross-talk when the signal is sent through a long data line, (c) sufficient bandwidth for the fast rise time of the input current from the photodetector, (d) low noise in order to achieve maximum signal to noise ratio, (e) fast readout speed to avoid pulse file up, (f) low power dissipation and (g) simple circuit for low cost fabrication and high reliability. In order to satisfy these limits, poly silicon is the best choice because it can be made on a large area as a-Si:H and has

better electronic characteristics than a-Si:H. For example, poly-Si TFT has a higher field effect mobility and lower threshold voltage than a-Si TFT. It has been found that a-Si:H TFTs cannot be used in making amplifiers due to its severe threshold voltage shift.[6,7] Polysilicon is composed of small crystalline silicon grains (5 nm ~ 5 μm).[8] It can be deposited on a substrate at a deposition temperature higher than 600°C, or can be made from amorphous silicon by high-temperature (600 ~ 900°C) thermal annealing or by laser-annealing.[9] Its electronic properties are worse than those of crystalline silicon but better than those of a-Si:H. Polysilicon is widely used in MOS integrated circuits usually for electrodes.[10] Also poly-Si TFTs have been investigated for applications to large-area electronics such as in LCD panels.[11] Fig. 3-7 shows a circuit diagram of the pixel amplifier based on poli-Si TFT technology. This pixel amplifier is composed of three stages.[7] The first stage is a low-noise charge sensitive amplifier which integrates the current signal from a photodetector and produces output signal as a voltage which is proportional to the charge generated in the photodetector. The second stage is a voltage amplifier for an additional gain and the final stage is a source follower output stage which sends an amplified signal through X and Y output data lines. A prototype pixel amplifier,[7] had a noise level of about 1,040 electrons, mainly due to 1/f noise, a dc gain of 110~150 and gain-bandwidth product of 300 MHz. The dynamic range of this amplifier was ~48 dB. Hence, poli-Si TFT technology may provide a low noise charge sensitive pixel amplifier. The field effect mobility of the poli-Si TFTs used in this prototype pixel amplifier was ~90 cm^2/Vsec, however, a new poli-Si TFT fabrication technology was developed recently using multishot excimer laser annealing at a low process temperature (< 600°C), and a high field effect
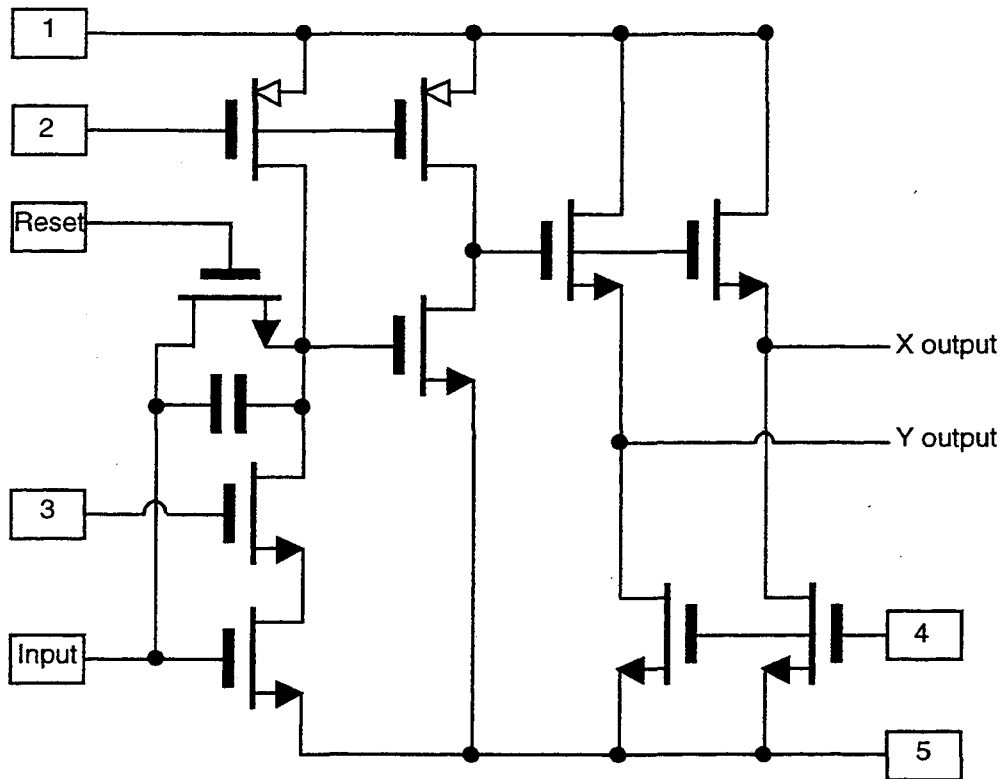
Fig. 3-7   Schematic circuit diagram of the poly-Si CMOS charge sensitive pixel amplifier for type A a-Si:H based gamma camera. Nodes 1~5 are for biasing.

mobility of 440 cm^2/Vsec was reported.[12] Using this technology, smaller pixel amplifiers with higher gain, faster charge transfer and lower noise are expected in the near future.

b)   Operation and Readout Scheme

The type A a-Si:H based gamma camera would be operated in event-by-event collection mode. With this mode the general operation scheme of the camera is similar to that of the conventional camera. The position of the interaction and the deposited energy in the scintillator can be obtained for each event. The readout electronics are shown in Fig. 3-8. Whenever a
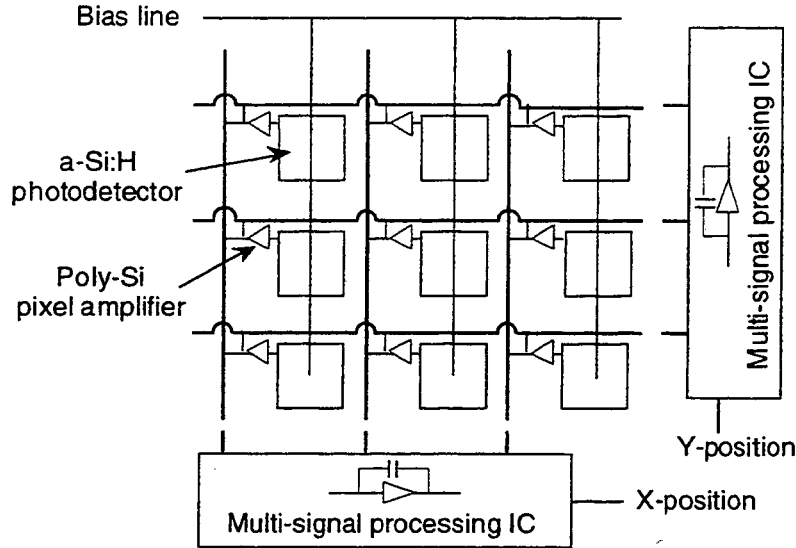
Fig. 3-8   Schematic diagram of a-Si:H pixel photodetector array with readout electronic circuitry of type A a-Si:H based gamma camera. Each pixel has a built-in amplifier made of poly-Si TFTs. This camera is operated in event-by-event collection mode.

γ-ray is absorbed in the scintillator several a-Si:H photodetectors are exposed to the visible light generated in the scintillator and these pixel detectors will produce signal distributions in both the X and Y signal output lines. Then the multi-signal processing IC outside the array determines the pixel position which corresponds to the maximum signal in both the X and Y directions, which is the position of the γ event in the scintillator. As the camera is composed of small pixel detectors on a flat surface, the position computation is much simpler than the conventional gamma camera.

Also there would be little nonlinearity effect in the obtained image. The image nonlinearity is one of the basic problems in the conventional gamma cameras which use photomultipliers and position encoding electronics. This is due to the nonlinearity of X and Y position signals with

displacement distance of a γ source across the face of the photomultiplier and generally produce pincushion or barrel distortion.[3] But in the a-Si:H based gamma camera the whole pixel detector array is made at the same time in a single deposition chamber, therefore, the light collection efficiency would be fairly uniform and the X and Y position signals would be linear with the displacement distance of a γ source across the surface of the detector array. As in the conventional gamma camera, the energy of the γ-ray which is absorbed in the scintillator of the type A a-Si:H based gamma camera is obtained by summing up all the signals in both the X and Y directions. This energy information is then sent to a pulse height analyzer, and if it falls within a predetermined energy range the event is recorded, otherwise it is rejected.

The type A a-Si:H based gamma camera would have some advantages over the conventional gamma cameras as stated above. But this camera would require an amplifier for each pixel, which makes the fabrication process complicated and also the cost high even with a simple circuit design. In terms of fabrication process, the type B camera which is described in the following section is much better than type A because it does not need a pixel amplifier but only an additional capacitor in each pixel.

3.2.2 Type B: a-Si:H Photodetector with Storage Capacitor

a)   Structure

As the type B a-Si:H based gamma camera needs only an additional storage capacitor in each pixel, its structure would be as simple as shown

47

in Fig. 3-9. The storage capacitor is composed of metal, insulator and metal, where silicon dioxide or silicon nitride can be used as the insulator. The other configuration of the camera is the same as the type A camera except that no pixel amplifiers are provided. The operation scheme, hence the readout electronics, are different from the type A camera.

b)   Operation and Readout Scheme

The type B a-Si:H based gamma camera would be operated in an integration mode, which means that the signal from each γ-ray interaction in the scintillator is collected by the photodetector and stored on the storage capacitor until the end of the γ scan.[5] Even a simple p-i-n photodetector without the storage capacitor can be operated in an integration mode. In this case, the signal generated in the p-i-n photodetector during the
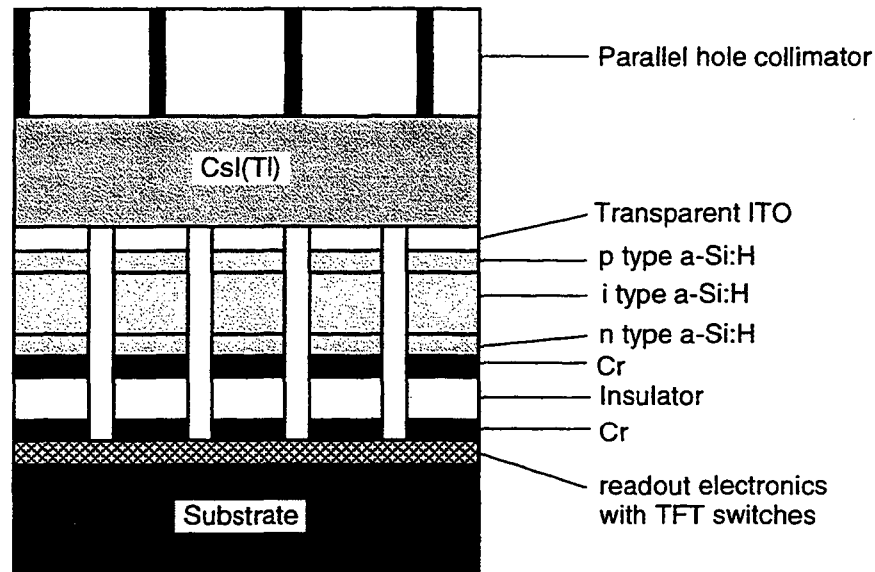
Fig. 3-9   Cross sectional diagram of type B a-Si:H based gamma camera which is simpler than type A camera. 5 pixels are shown and the drawing scale is arbitrary.

imaging period is collected by the internal field of the photodetector and stored on the photodetector itself by its intrinsic capacitance and the OFF-resistance of the TFT switch which is connected to the photodetector. By closing the TFT switch after the integration, the signal charge is read out. With an ordinary p-i-n photodetector, however, the signal charge decays exponentially with time during the integration period. This charge loss is due to the leakage through the photodetector and OFF-state TFT switch because of their finite resistance. The charge loss can be reduced by making the TFT smaller and lowering the temperature. With p-i-n photodetector only, decay constants of a few tens of seconds with the photodetector capacitance of 10~100 pF and γ-ray imaging with 20 sec integration time were reported.[13,14] Therefore, for a γ scan of 3 min with a 1 mm x 1 mm x 1 μm (105 pF) p-i-n photodetector alone, 9 successive readouts with 20 sec integration period would be needed. With an addition of the storage capacitor to the normal p-i-n a-Si:H photodetector, there is no need to successively read out the signal charge because there is no leakage of charge as it is blocked by the insulator. But thermally generated dark current in the p-i-n photodetector would also be collected and integrated on the storage capacitor.[5] This thermally generated background charge can be measured separately for a given integration period and subtracted from the measured total signal. If the thermal generation current is too high, however, the background charge will dominate the signal charge and saturate the storage capacitor, therefore the signal charge cannot be stored with full efficiency. The thermal generation current, however, can be reduced significantly by lowering the ambient temperature. The effect of the temperature on the thermal generation current is discussed in detail in Chapter 4, where the experimental results with test devices of the type B

49

a-Si:H based gamma camera in an integration mode are also discussed. With the type B a-Si:H based gamma camera, 3 min of integration time can be achieved as discussed in Chapter 4.

A schematic diagram of readout electronics for the type B camera is shown in Fig. 3-10. Each pixel, which is composed of a-Si:H p-i-n photodetector and a storage capacitor, is connected to a TFT switch. The TFT switch can be made of either a-Si:H or poly-Si. a Poly-Si TFT is, of course, faster than a-Si:H TFT because the field effect mobility is higher,[15] but at the end of the γ scan only one readout from each pixel is needed, so a-Si:H TFT can also be used. The advantage of the a-Si:H TFT over the poli-Si TFT is that it can be made laterally at the same level with the p-i-n photodetector, while poli-Si TFT should be made first and the p-i-n photodetector then deposited on top of the poli-Si TFT. The fabrication
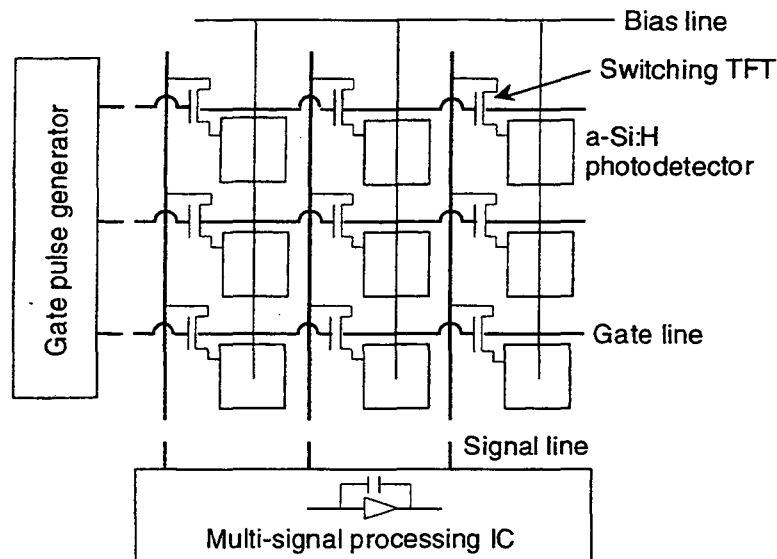
Fig. 3-10   Schematic diagram of readout electronics in type B a-Si:H based gamma camera. There are no pixel amplifiers like the type A camera, instead a simple TFT switch is connected to each pixel and this switch is operated by the gate pulse generator.

process of an a-Si:H photodetector and TFT switch is, therefore, simpler than an a-Si:H photodetector and poli-Si TFT fabrication. Laterally made a-Si:H TFTs have been successfully used in a-Si:H optical and x-ray imaging arrays.[16-19] If a high fill factor of the photodetector array is needed, fabrication of the poli-Si TFT readout electronics beneath the photodetector array would be an appropriate choice.

The readout scheme would be, basically, the same as in the x-ray imaging. After the whole γ scan, the gate pulse generator triggers the TFT switches row by row and the stored signal charge is sequentially sent to the signal processing unit outside the detector array.

As the signal charge is accumulated on a storage capacitor in each pixel, no information of the signal can be obtained until the end of the γ scan period. Moreover, the pixel cannot distinguish the true signal (γ-ray which did not interact inside the patient's body) from the false signal (γ-ray which had a single or many Compton scatterings inside the patient's body). Hence, the storage capacitor will store both the true and false signal charge. As the history of the signal charge on a certain pixel is unknown, scattering rejection with a pulse height analyzer is impossible. This is the primary disadvantage of the type B camera, although its structure and operation scheme is simple. The images obtained will be more blurred than the images with the conventional gamma camera or the type A a-Si:H based gamma camera due to the scattered γ-rays inside the patient's body. If, however, the blurring characteristics are known and the effect is not too severe, the image may be restored by appropriate image processing. Wiener filtering is one of the methods for this purpose, and the image restoration of simulated images using this filter is described in Section 3.5.

3.3 Monte Carlo Simulations

Gamma Cameras based on a-Si:H imaging technology have not been made yet. Therefore, in order to predict their performance as gamma cameras and test their feasibility, Monte Carlo simulation codes were made using Fortran 77. The performance of the type A a-Si:H based gamma camera which was described in the Section 3.2.1 would be similar to that of the conventional gamma cameras, hence most of the simulations were concentrated on obtaining the characteristics of the type B a-Si:H based gamma camera which would be operated in the integration mode.

3.3.1 Materials Used in the Simulations

a) Phantom

As the density of the human body is somewhat similar to that of water, water was used as a phantom material in the simulations. Water is frequently used to replace the human body in many simulations and the attenuation coefficients for photons in water are easily available. They are plotted in Fig. 3-11 for the photon energy range of 10 keV to 150 keV.

b) Radioisotopes

As radiation sources ^{99m}Tc and ^{201}Tl which emit γ-rays with the energy of 140 keV and 70 keV, respectively, were used. These are conventional isotopes for cardiac imaging in nuclear medicine. ^{99m}Tc is produced in the β^- decay of ^{99}Mo. As it is in the metastable state it decays to
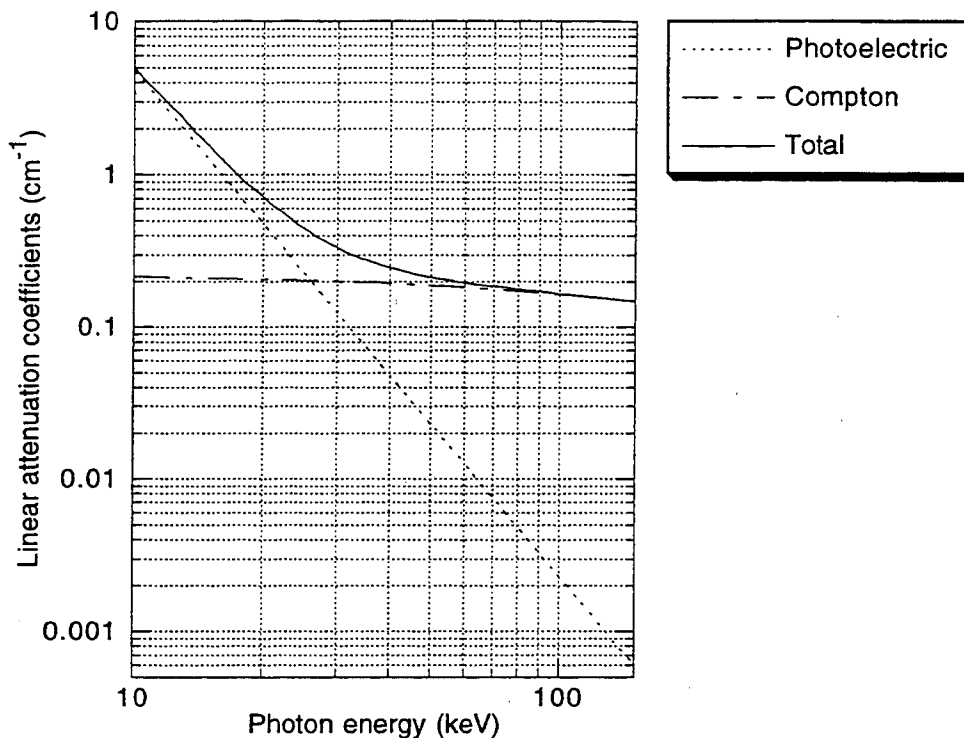
Fig. 3-11   Linear attenuation coefficients of photons in water.

the ground state by isomeric transition, emitting a 140 keV γ photon, and has a half-life of 6 hours. [99m]Tc is the most widely used radionuclide generator produced radioisotope. [201]Tl is produced by charge particle bombardment. When [203]Tl is bombarded with proton it becomes [201]Pb emitting three neutrons. This [201]Pb decays to ^{201}Tl mostly by electron capture (>99%), and ^{201}Tl decays to the ground state, emitting a ~70 keV γ-ray with a half-life of 73 hours.[20]   The characteristics of these two radionuclides are summarized in Table 3-1.

c)   Collimator

A parallel-hole collimator was assumed and, in order to save calculation time, the spatial resolution data of one of the commercially

Table 3-1   Properties of ^{99m}Tc and ^{201}Tl

Isotope	γ-ray energy (keV)	Mode of decay	Half-life (hours)	Production method
^{99m}Tc	140	Isomeric transition	6	Radionuclide generator
^{201}Tl	70	Electron capture	73	Proton bombardment

available collimators[26] were used to select the γ photons with right directions rather than Monte Carlo calculations of the photon trajectories in the collimator. Details are described in Section 3.3.2 b).

d)   Scintillator

As discussed in the previous sections CsI(Tl) is the best choice for a scintillator coupled to a-Si:H photodetectors.   In the simulations un-segmented CsI(Tl) crystal was assumed. The attenuation coefficient data for γ photons in CsI(Tl) is plotted in Fig. 3-12. The visible light yield from CsI(Tl) was assumed to be 5.2 x 10^4 photons/1 MeV deposited-energy, on average, and the angular distribution to be isotropic.[21]

e)   a-Si:H Pixel Photodetector Array

As the photodetector array, the pixel photodetector configuration in the type B a-Si:H based gamma camera, that is, normal a-Si:H p-i-n photodiodes with storage capacitors, was used in the simulations. The detector area in the simulations was 12.8 x 12.8 cm^2 with various pixel sizes. The detector quantum efficiency was assumed to be 70 %, which is
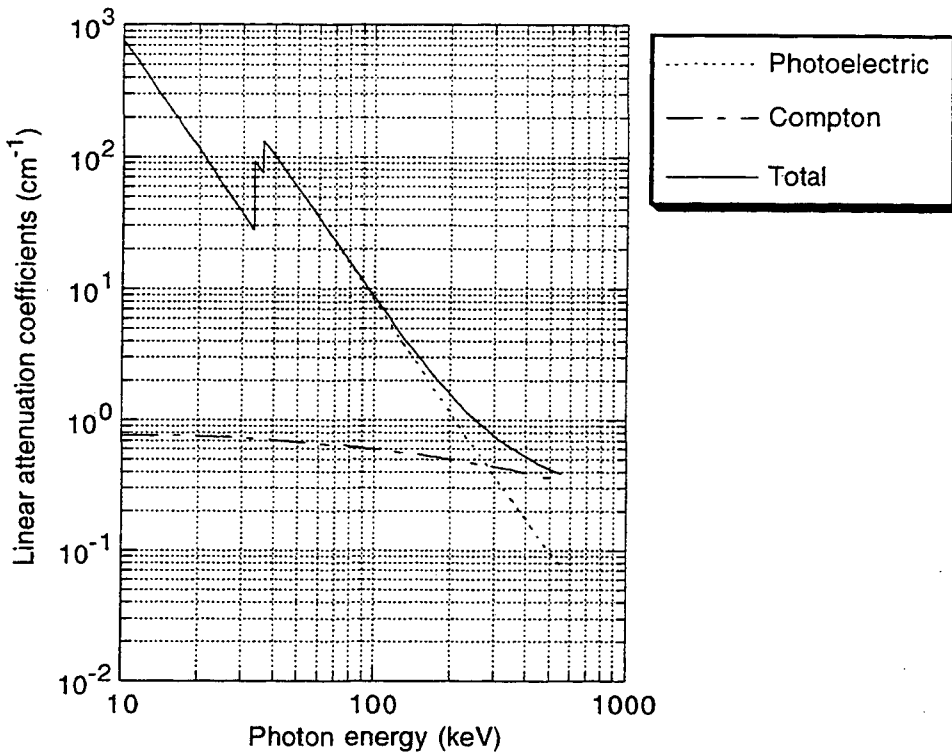
Fig. 3-12   Linear attenuation coefficients of photons in CsI(Tl).

lower than previously reported values of ~ 80 %.   Therefore 70 % is a conservative assumption.

3.3.2   Physics Involved in the Simulations

a)   Photon interactions in the phantom and the scintillator.

A photon can interact with a medium in various ways according to the probability of occurrence of a specific interaction, which generally depends on the energy of the photon and the material properties of the medium.   The kinds of the interactions induced by photons can be categorized into two groups.   One is for the major processes which include

the well known photoelectric effect, Compton scattering and pair production, and the other is for the minor processes which include coherent scattering from electrons, fluorescence radiation, Bremsstrahlung and annihilation radiation.[22]   For the γ-ray energy range of 70 ~ 140 keV, the cross sections of the pair production is zero and all of the interaction mechanisms in the minor process category are negligible compared to the photoelectric effect and the Compton scattering. So, only the photoelectric effect and the Compton scattering were considered as the photon interactions in the phantom and scintillator in the simulations.   The position of the interaction and the direction of the scattered photon were calculated based on the cross section data in Fig. 3-11 and 3-12. The details of these calculations are as follows.

i)   Next Interaction Position

A γ photon either from the γ source or Compton scattering event will have an interaction inside the medium or escape from it. In order to find which is the case, the distance from the γ source or previous scattering position to the next interaction position is needed. When a γ-ray is traveling a distance s, the probability, $p(s)ds$, of having an interaction between s and $s+ds$, is

$$p(s)ds = \Sigma_t(E)e^{-\Sigma_t(E)s}\,ds ,\qquad\qquad (3\text{-}1)$$

where $\Sigma_t(E)$ is the total linear attenuation coefficient of a photon with an energy E. The integration of p(s) from $s = 0$ to infinity gives unity, hence p(s) is a probability density function (PDF) and the cumulative distribution function (CDF) corresponding to this PDF is

$$P(s) = \int_0^s p(s')ds' = 1 - e^{-\Sigma_t(E)s}. \qquad (3\text{-}2)$$

Then, using the inverse distribution method,[23] s, which is the traveling distance of the photon from the last event to the next interaction, can be obtained as

$$s = P^{-1}(\xi) = -\frac{1}{\Sigma_t}\ln\xi, \quad 0 < \xi \le 1, \qquad (3\text{-}3)$$

where ξ is a random number which is uniform between 0 and 1. So, if a photon at a position $\mathbf{r}_1(x_1, y_1, z_1)$ is heading to the direction of $\omega(\omega_x, \omega_y, \omega_z)$, then the position $\mathbf{r}_2(x_2, y_2, z_2)$ where the photon will have an interaction with the medium is

$$\begin{aligned} x_2 &= x_1 + s\,\omega_x \\ y_2 &= y_1 + s\,\omega_y \\ z_2 &= z_1 + s\,\omega_z \end{aligned} \qquad (3\text{-}4)$$

where ω_x, ω_y and ω_z are the x, y and z components of the directional unit vector ω and s is obtained from Eq. (3-3). If $\mathbf{r}_2$ is out of the phantom or scintillator geometry, then that photon does not have an interaction in the corresponding medium any more.

ii)   Selection of Interaction Type

Whenever a γ interaction position is given in the phantom or in the scintillator the type of the interaction is determined by the following simple rejection techniques : First, select a random number, ξ. If ξ is greater or equal to $\Sigma_p(E)/\Sigma_t(E)$, then this photon has a photoelectric absorption interaction on that position. Otherwise, it has a Compton scattering on that position.

57

ii)   <u>Direction of Compton scattered γ-ray</u>

When a γ photon is involved in the photoelectric effect, it is absorbed in the medium and it is terminated. But, if it is Compton scattered it loses part of its energy and is deflected. Therefore, a new direction and a new energy of the scattered photon should be computed and this can be done using the angular dependent cross section of the Compton scattering. The differential cross section of the Compton scattering according to the famous Klein-Nishina's formula is[24]

$$\frac{d\,\sigma_c(\alpha,\vartheta)}{d\,\Omega} = r_o^2 \left[\frac{1}{1+\alpha(1-\cos\vartheta)}\right]^3 \left(\frac{1+\cos^2\vartheta}{2}\right)\left\{1+\frac{\alpha^2(1-\cos\vartheta)^2}{(1+\cos^2\vartheta)[1+\alpha(1-\cos\vartheta)]}\right\}, \quad (3\text{-}5)$$

where, Ω is the solid angle, α is the energy of the incident photon in electron rest energy unit, r_o is the classical radius of the electron and θ is the deflection angle of the scattered photon. The total cross section ($\sigma_c(\alpha)$) of the Compton scattering is obtained by the integration of Eq. (3-5) from $\cos\theta = -1$ to 1, and is express as

$$\sigma_c(\alpha) = 2\pi r_o^2 \left\{\frac{1+\alpha}{\alpha^2}\left[\frac{2(1+\alpha)}{1+2\alpha} - \frac{1}{\alpha}\ln(1+2\alpha)\right] + \frac{1}{2\alpha}\ln(1+2\alpha) - \frac{1+3\alpha}{(1+2\alpha)^2}\right\}. \quad (3\text{-}6)$$

The cross sections in Eq. (3-5) and (3-6) are independent of the atomic numbers of the elements which constitutes the given medium. So the angle of scattering can be selected by the same procedure for any medium. The PDF to be sampled can be expressed as

$$p(\alpha,\vartheta) = \frac{1}{\sigma_c(\alpha)}\frac{d\,\sigma_c(\alpha,\vartheta)}{d\,\Omega}. \quad (3\text{-}7)$$

Now, as the PDF is known selection of the deflection angle, θ, is possible. There are many procedures to select θ from Eq. (3-7), including

the rejection technique, inverse CDF method and direct sampling etc. Among these, the direct sampling method proposed by Koblinger[23] is good for high energy photons (E > 1.4 MeV), and the rejection method proposed by Kahn[25] is very efficient for low energies (E ≤ 1.4 MeV). The rejection method was used in the simulation. The flow chart of this method is shown in Fig. 3-13 and the angular distribution of the Compton scattered photons obtained using this method is plotted in Fig. 3-14, which shows that as the incident photon energy increases the scattering is more in the forward direction, as is the normal behavior in Compton scattering.
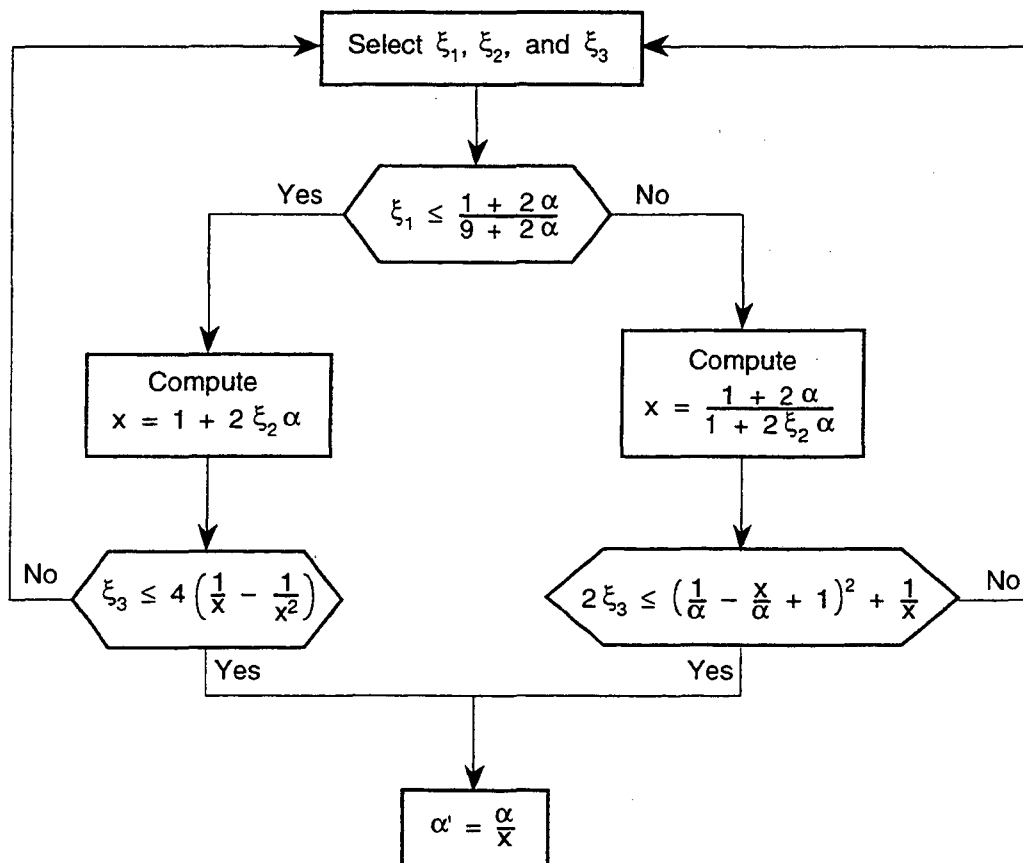
Fig. 3-13   The flow chart of the rejection method for sampling from the Klein-Nishina distribution. $x = 1 + \alpha(1 - \cos\vartheta)$ is the ratio of the photon energy before scattering(α) to after scattering(α').
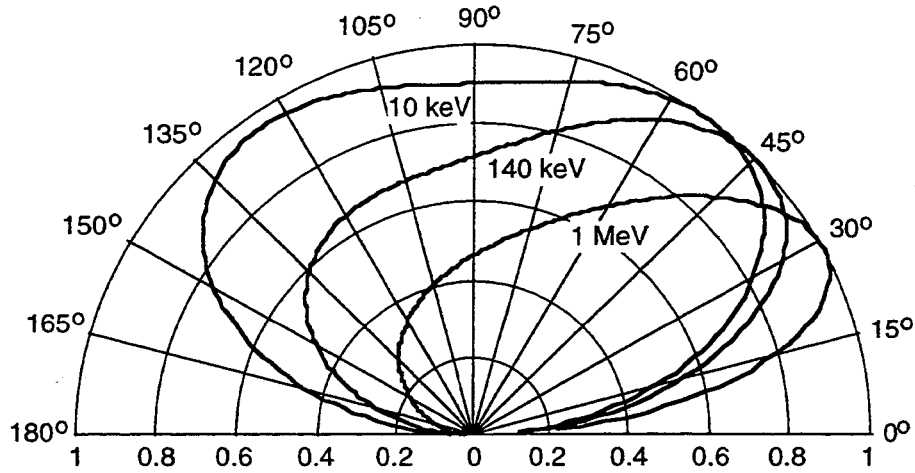
Fig. 3-14   Number vs. angle distribution of Compton scattered
photons obtained by the rejection method.

Once θ is selected, the directional unit vector $\omega'(\omega_x, \omega_x, \omega_x)$ of the
scattered photon (see Fig. 3-15) can be found by the following equations.

For $-1 < \omega_z < 1$,

$$\omega'_x = \sqrt{\frac{1-\mu^2}{1-\omega_z^2}}\left[\omega_y\cos\varphi + \omega_x\,\omega_z\sin\varphi\right] + \omega_x\mu ,$$

$$\omega'_y = \sqrt{\frac{1-\mu^2}{1-\omega_z^2}}\left[-\omega_x\cos\varphi + \omega_y\,\omega_z\sin\varphi\right] + \omega_y\mu , \qquad (3\text{-}8a)$$

$$\omega'_z = -\sqrt{(1-\omega_z^2)(1-\mu^2)}\,\sin\varphi + \omega_z\mu .$$

And, for $\omega_z = \pm 1$,

$$\omega'_x = \sqrt{1-\mu^2}\,\cos\varphi ,$$

$$\omega'_y = \sqrt{1-\mu^2}\,\sin\varphi , \qquad (3\text{-}8b)$$

$$\omega'_z = \omega_z\,\mu ,$$

$$\omega = \omega_x \mathbf{i} + \omega_y \mathbf{j} + \omega_z \mathbf{k}$$

$$\omega' = \omega'_x \mathbf{i} + \omega'_y \mathbf{j} + \omega'_z \mathbf{k}$$

$$= \omega'_1 \mathbf{u_1} + \omega'_2 \mathbf{u_2} + \omega'_3 \mathbf{u_3}$$

$$\omega'_1 = \sin\theta \cos\varphi$$

$$\omega'_2 = \sin\theta \sin\varphi$$

$$\omega'_3 = \cos\theta$$
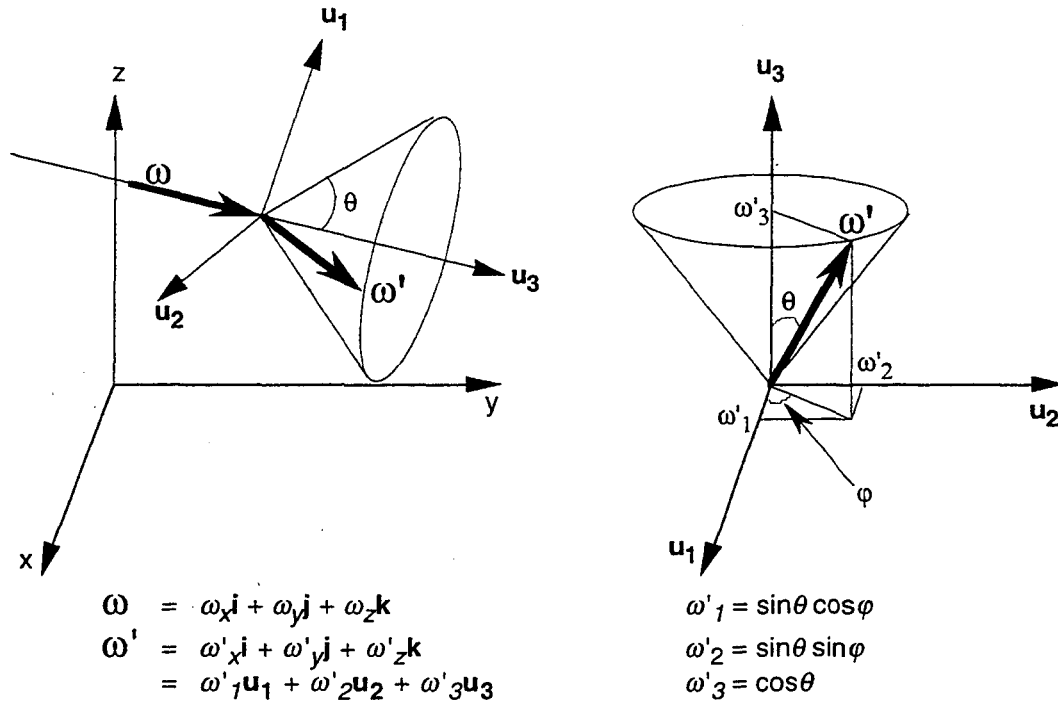
Fig. 3-15   Relationship of directions between the incident photon and Compton scattered photon. ω'_x, ω'_y, and ω'_z are expressed in Eq. (3-8a) and (3-8b).

where, μ is $\cos\theta$. As the distribution of the scattered photons across the azimuthal angle, φ, is uniform, φ can be selected by $\varphi = 2\pi\xi$, where ξ is a random number.

The energy of the scattered photon, E', is calculated by

$$E' = \frac{m_o c^2}{1 - \mu + 1/\alpha} , \qquad (3\text{-}9)$$

where, $m_o c^2$ is the rest mass energy of the electron.

b)   Photon Rejections in the Collimator

A parallel-hole collimator is composed of a large number (usually more than 20,000 for high resolution) of small square holes (hole size = 1 ~

61

3 mm), and it is complicate to calculated the photon behavior when it enters the collimator. Therefore, for the sake of the simplicity of the calculation and time saving, spatial resolution data for the typical low-energy high-resolution parallel-hole collimator were used.[26] The hole size, septal thickness and collimator thickness of this collimator is 1.4 mm, 0.254 mm and 25.2 mm, respectively, and the spatial resolution as a function of source-to-collimator distance is shown in Fig. 3-16. The procedure for selecting the appropriate γ photons in the collimator using the data in Fig. 3-16 is as follows. When a γ photon from the phantom reaches the top of the collimator its position on that plane, (x_c, y_c), is

$$x_c = x_p - z_p \frac{\omega_x}{\omega_z}$$

$$y_c = y_p - z_p \frac{\omega_y}{\omega_z},$$

(3-10)
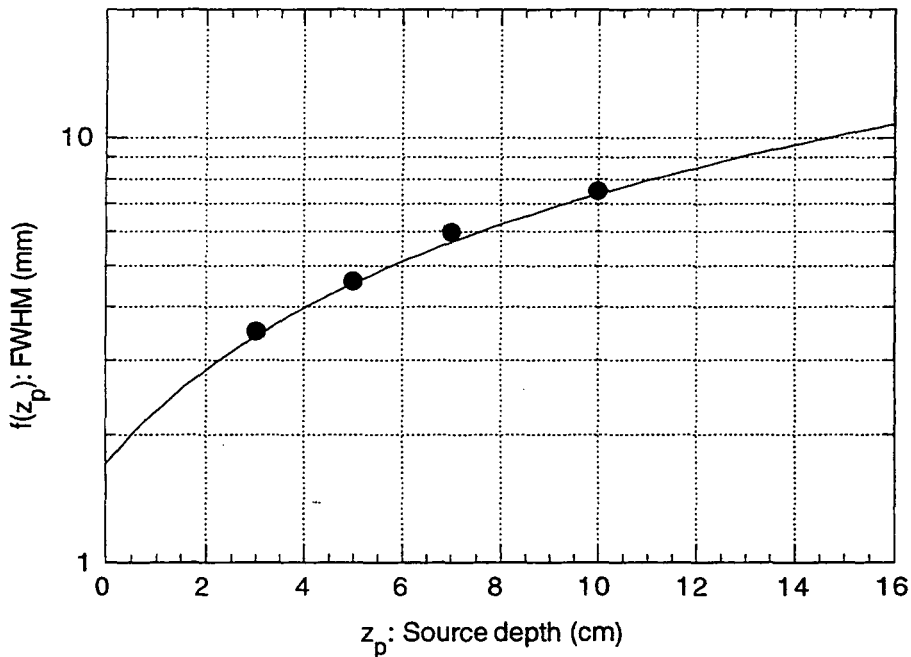
Fig. 3-16 Spatial resolution of Picker low-energy high-resolution parallel collimator. The closed circles are explained in the text.

where, (x_p, y_p, z_p) is the position in the phantom where the γ photon had a last event before it comes to the collimator, and $(\omega_x, \omega_y, \omega_z)$ is the directional unit vector of the γ photon. It was assumed in the simulation that if a parameter, r_c, defined as

$$r_c \equiv \sqrt{(x_c - x_p)^2 + (y_c - y_p)^2}$$

is smaller than $f(z_p)/2$, the γ photon was transmitted. Otherwise it is killed by the collimator. The quantity $f(z_p)$ is the spatial resolution of the collimator at a source depth of z_p and is given in Fig. 3-16. To test this assumption a program was made which gives the photon distributions after collimation, with various source depths, and the spatial resolutions obtained from these distributions are plotted in Fig. 3-16 as closed circles, which shows this assumption is valid.

c)   Emission of Visible Photons in CsI(Tl)

The emission of visible light in the scintillator by the γ-ray interaction is due to combinations of the interactions which are categorized as the minor processes as described in Section 3.3.2 a). In order to simplify the computation, isotropic emission of visible light with a constant wavelength was assumed whenever a γ photon has an interaction in CsI(Tl). The number of the visible light photons emitted by an interaction of a γ photon with CsI(Tl) was assumed to follow a normal distribution with a mean value of $5.2 \times 10^4 \cdot E_\gamma$ photons,[21] where E_γ is the γ-ray energy in MeV which is absorbed in the scintillator. The method of sampling from a normal distribution is well described in Reference 23.

START

Generate New γ

Calculate Cross Sections in Water

Calculate New Energy and Direction

Calculate Next Collision Position

Determine
(1) Still in Phantom ?
(2) Out of Boundary ?
(3) Enter Collimator ?

(1)

(2)

Determine
(1) Photoelectric ?
(2) Compton Scattering ?

(1)

(2)

Water Phantom

(3)

Determine
Transmitted ?
or Killed ?
in Collimator

Killed

Collimator

Transmitted

Calculate Cross Sections in CsI(Tl)

Calculate Next Collision Position

Determine
Still in Scintillator?
or Out of Boundary ?

Out of Boundary

Still in Scintillator

Determine
Photoelectric ?
or Compton Scattering ?

Compton

Generate Visible Photons with Isotropic Direction and Follow the Trajectories

Record the Photon which Arrives at the Photodetector

Calculate New Energy and Direction of γ

Photoelectric

Generate Visible Photons with Isotropic Direction and Follow the Trajectories

Record the Photon which Arrives at the Photodetector

CsI(Tl) and photodetector

Full Acquisition ?

No

Yes

STOP

Fig. 3-17   The flow chart of the Monte Carlo simulations of γ-ray imaging for type B a-Si:H based gamma camera.

The flow chart of the Monte Carlo simulation code is drawn in Fig. 3-17 and its content is listed in Appendix.

3.3.3 Simulation Results

a)   Scintillator and Photodetector Response

The response of the CsI(Tl) and the photodetector array in type B a-Si:H based gamma camera were simulated with various thicknesses of CsI(Tl) and pixel sizes of the photodetectors. The γ-ray absorption property of CsI(Tl) as a function of its thickness with the γ energy of 70 and 140 keV is shown in Fig. 1-18. From the graph, a 2 mm thick CsI(Tl) is sufficient to absorb the 70 keV γ-rays (99% absorbed), while a 5 mm thick CsI(Tl) is
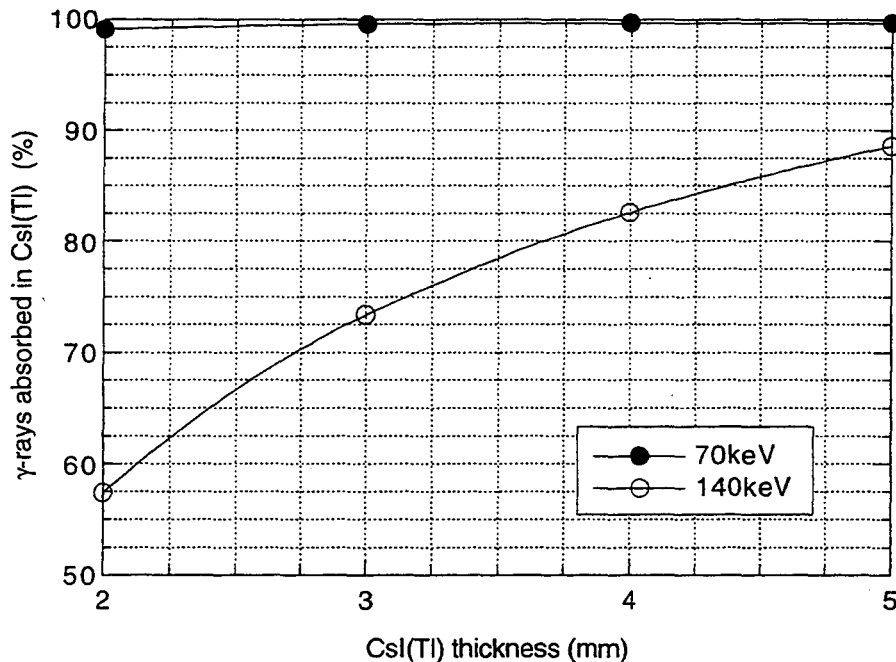
Fig. 3-18   Percentage of γ-rays absorbed in CsI(Tl) as a function of CsI(Tl) thickness.

required to absorb 89% of 140 keV γ-rays.

In order to obtain the intrinsic resolution of the camera, several simulations were performed with the collimator removed. A point source of γ in vacuum was assumed to emit γ-rays which were incident on the CsI(Tl) crystal perpendicular to its surface. The results are plotted in Fig. 3-19 for various cases of γ-ray energies, CsI(Tl) thicknesses and pixel sizes. With 140 keV γ-ray, the resolution is insensitive to CsI(Tl) thickness. The reason is as follows. The amount of light generation in CsI(Tl) at this γ energy is almost uniform through the γ's passage in CsI(Tl) due to the low cross section of CsI(Tl) at this energy and the distribution of the light generated near the bottom of the CsI(Tl) eventually determines the spatial resolution, hence the thickness of CsI(Tl) is not a dominant factor to
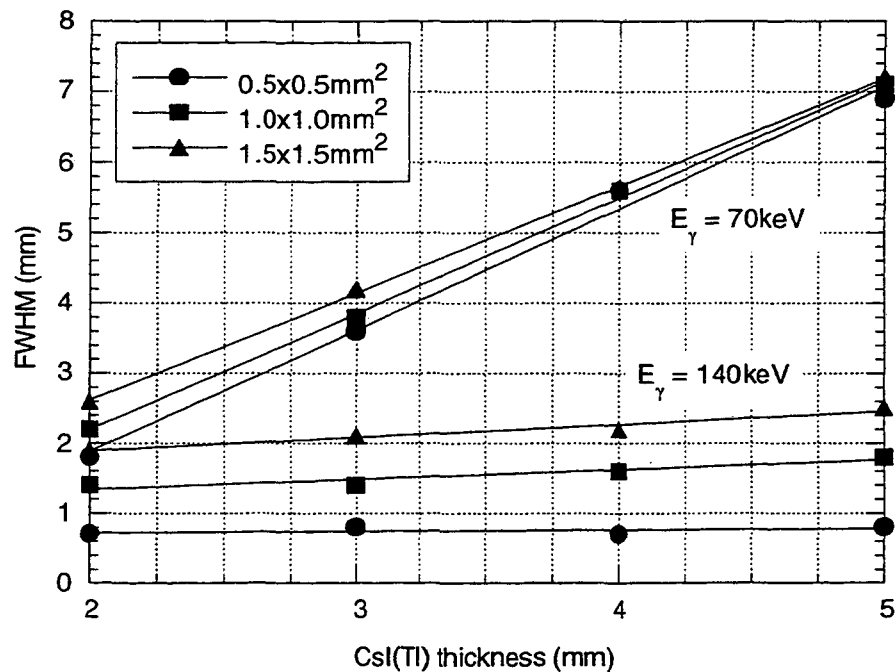
Fig. 3-19   Intrinsic resolution of a-Si:H based gamma cameras as a function of CsI(Tl) thickness with different pixel sizes and γ-ray energies.

determine the intrinsic spatial resolution in this case. By the same reason, the resolution is sensitive to the pixel size at this energy, that is, the solid angle of a pixel when viewed from a position near the bottom of the scintillator changes much as the pixel size changes. For 70 keV γ energy, CsI(Tl) has a high cross section and the resolution is sensitive to the thickness of CsI(Tl) and insensitive to the pixel size of the photodetector, which can be explained with the same physical concept as in the case of 140 keV.

From the above results, a CsI(Tl) crystal of 2 mm is suitable for 70 keV γ-ray imaging and thickness of 5 mm or more is adequate for 140 keV γ-ray imaging. With a pixel size of 1 mm x 1 mm, the intrinsic spatial resolution is 2.2 mm with 70 keV γ-ray and 2 mm thick CsI(Tl), and 1.8 mm with 140 keV γ-ray and 5 mm thick CsI(Tl), which are better than those of the conventional gamma camera (3 ~ 4 mm).[1] By reducing the pixel size of the photodetectors in a-Si:H based gamma camera better intrinsic spatial resolution can be achieved, but there is no need for this because the major contributor to the total spatial resolution is the collimator.

b)   Effect of Scattering in the Phantom

As mentioned before, the major concern of the Monte Carlo simulations was to investigate the effect of the Compton scattering in the patient's body when a type B a-Si:H based gamma camera was used. For this, the point spread function (PSF) from a point source in a water phantom was simulated. A γ source with 70 keV or 140 keV was located 5 cm or 10 cm from the collimator surface in order to see the Compton

scattering effect with different γ energy and source depth. For 70 keV γ-rays, 2 mm thick CsI(Tl) was used, and for 140 keV γ-rays, 5 mm thick CsI(Tl) was used.

Fig. 3-20 shows the profiles of the PSFs obtained from the simulations. The peak of the PSF corresponds to the response of the gamma camera and the FWHM is equal to $\sqrt{R_c^2 + R_i^2}$, where R_c is the spatial resolution of the collimator and R_i is the intrinsic spatial resolution of the gamma camera shown in Fig. 3-19. The exponential tail of the PSF is due to the scattering in the phantom and agrees well with the measurements by others.[27] As the source depth increases, the exponential tail broadens because of the increased number of the scattering events in the phantom. Due to the higher ratio of the cross section for
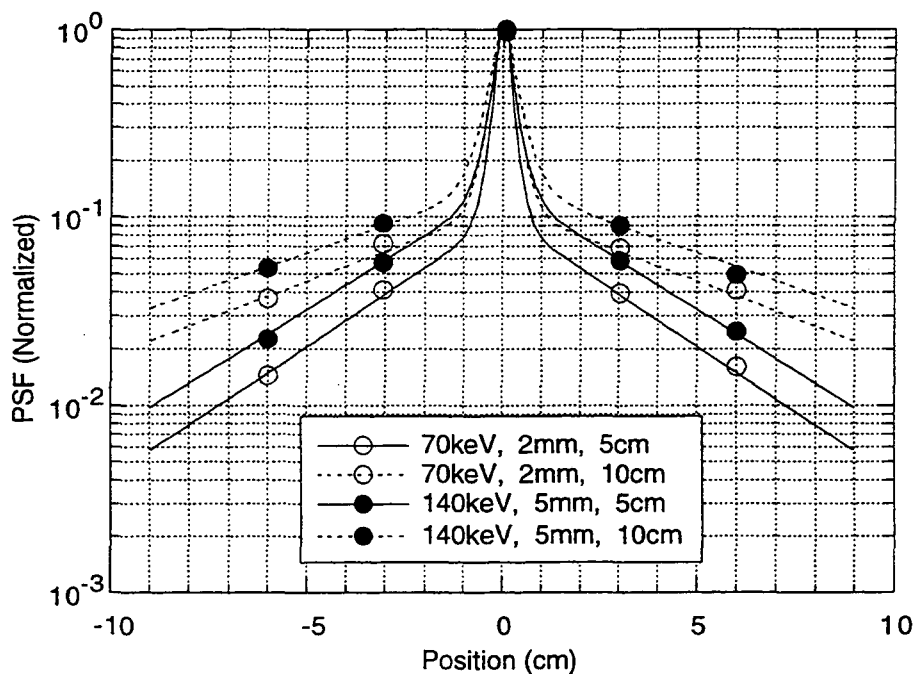
Fig. 3-20   PSF from a point source in water with different γ energies and source depths; γ energy: 70 and 140 keV; source depth: 5 and 10 cm; CsI(Tl) thickness: 2 and 5 mm.

Compton scattering to photoelectric absorption in water, the PSF of 140 keV γ-rays has higher scattering component than that of 70 keV γ-rays. The statistics of the γ photon interactions obtained from the simulations are summarized in Table 3-2.

From the results in Fig. 3-20, it is expected that the projection image obtained with type B a-Si:H based gamma camera will be blurred due to the scatterings in the patient's body. However, using a deconvolution method, the blurring effect due to scattering can be significantly reduced as shown in Section 3.4.

Table 3-2   Statistics of γ photons from the simulations. 5.0×10^6 γ photons were simulated. Water phantom size = $40 \times 40 \times 6$ cm^3. Collimator and detector area = 14.1×14.1 cm^2.

For 70 keV γ's

Source depth (cm)	Interactions		Photon status			
	Photoelectric absorption	Compton scattering	Absorbed	Escaped	Collimator-arrived	Detected
5	1.4×10^6 (9.76 %)	1.3×10^7 (90.24 %)	1.4×10^6 (28.67 %)	2.4×10^6 (48.91 %)	1.1×10^6 (22.42 %)	2.1×10^4 (0.43 %)
10	2.8×10^6 (11.96 %)	2.1×10^7 (88.04 %)	2.8×10^6 (56.82 %)	1.5×10^6 (30.99 %)	6.1×10^5 (12.19 %)	1.2×10^4 (0.23 %)

For 140 keV γ's

Source depth (cm)	Interactions		Photon status			
	Photoelectric absorption	Compton scattering	Absorbed	Escaped	Collimator-arrived	Detected
5	4.8×10^5 (3.47 %)	1.3×10^7 (96.53 %)	4.8×10^5 (9.58 %)	3.3×10^6 (65.12 %)	1.3×10^6 (25.30 %)	2.3×10^4 (0.45 %)
10	1.4×10^6 (5.64 %)	2.4×10^7 (94.36 %)	1.4×10^6 (28.66 %)	2.7×10^6 (54.82 %)	8.3×10^5 (16.52 %)	1.5×10^4 (0.30 %)

c) Phantom Images

In order to obtain a projection image of γ source distribution, a water phantom consisting of three regions was assumed. The size of the phantom was 30 x 30 x 15 cm^3. In the cold region there is no γ source, the warm region, whose size is 8 x 4 x 4 cm^3, contains ^{99m}Tc with the activity of 83.5 kBq/ml, and the small sized (8 x 8 x 8 mm^3) hot region contains ^{99m}Tc with higher activity of 918.5 kBq/ml. Both the warm and the hot region are located at the center of the cold region. The geometry of the phantom is shown in Fig. 3-21 and its parameters are listed in Table 3-3. In the simulations, two images were obtained using two different gamma cameras; one is the type B a-Si:H based gamma camera and the other is a ZLC 75 Siemens camera[28] which is one of the conventional gamma cameras. The same collimator was used in both of the cameras and the parameters of these gamma cameras used in the simulations are also listed in Table 3-3. The two images obtained from the simulations are shown in Fig. 3-22 along with the true object image of the phantom. For the same acquisition time of 3 min, the type B a-Si:H based gamma camera collected more data (3.0 x 10^6 γ's) than the conventional gamma camera (9.6 x 10^5 γ's) because the a-Si:H based gamma camera recorded more of the
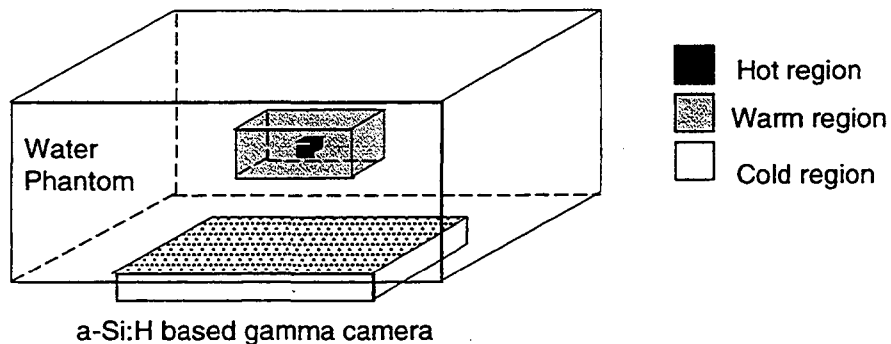
Fig. 3-21   The geometry of the water phantom with hot, warm and cold sources.

scattered γ-rays than the conventional camera. The simulated image using type B a-Si:H based gamma camera is more blurred than the image obtained using a conventional gamma camera, evidently due to the scatterings.

Table 3-3   Parameters of the water phantom and the type B a-Si:H based gamma camera and a conventional gamma camera used in the simulations

Water Phantom

Region	Size (cm^3)	Location	γ source	Activity (kBq/ml)
Cold	30 x 30 x 15	cold region defines the phantom size	none	0
Warm	8 x 8 x 4	center of the phantom	^{99m}Tc	83.5
Hot	0.8 x 0.8 x 0.8	center of the phantom	^{99m}Tc	918.5

Type B a-Si:H based gamma camera

Scintillator	Pixel size	No. of pixels
5 mm thick CsI(Tl)	1 x 1 mm^2	128 x 128

Conventional Gamma Camera

Intrinsic resolution	Energy window
3.8 mm	10% below the source γ energy
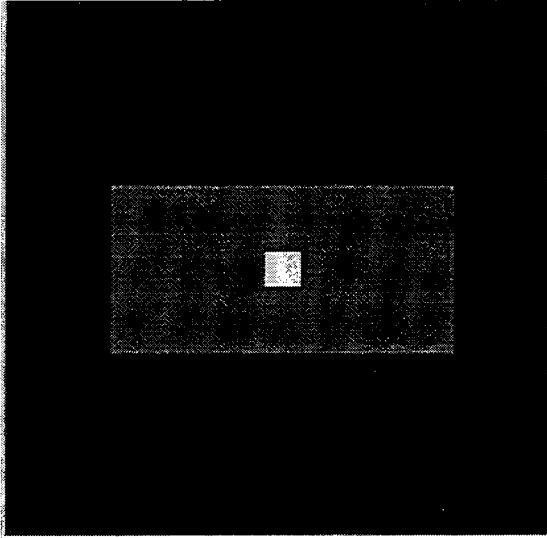
(a)
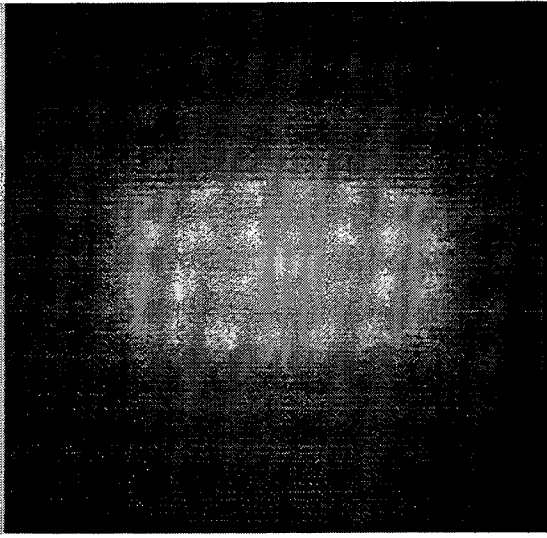
(b)
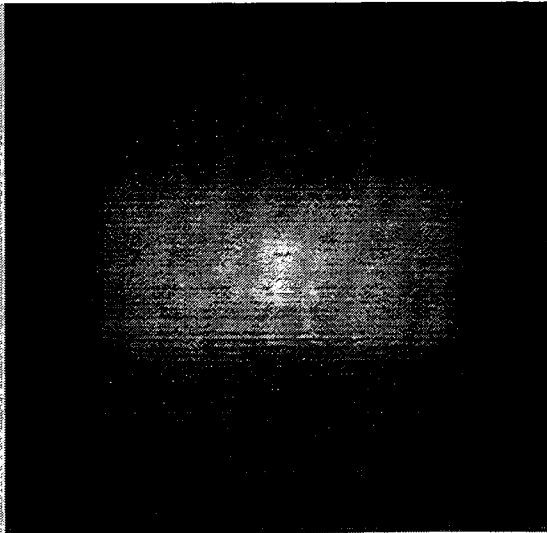
(c)

Fig. 3-22   Images obtained from simulations:
(a) true object image,
(b) with type B a-Si:H based gamma camera,
(c) with a conventional gamma camera.

3.4 Image Analyses

3.4.1 Noise Analyses

There are three types of noise sources in the image obtained with an a-Si:H based gamma camera: (1) the noise due to the random process of radiation emission and absorption, (2) the noise due to the fluctuations in the conversion of γ-ray energy to visible light and (3) the noise from photodetectors and readout electronics.[29] The image shown in Fig. 3-22 (b) contains the noise of (1) and (2). This noise is count-dependent Poisson noise and is generally observed in nuclear medicine images.[30-33] Thermal noise, shot noise and 1/f noise in the photodetector and readout electronics are the sources of noise type (3),[29,34-37] and this noise may be approximated as a Gaussian noise.[29] As the dark current in the photodetector is very low (less than 0.1 nA/cm^2), the shot and 1/f noise can be neglected and the dominant noise source would be the thermal noise due to TFT ON-state resistance. This thermal noise is proportional to the capacitance of the photodetector and the temperature,[37] so it can be reduced either by making the pixel size smaller or reducing the operating temperature, which is also needed for long-term charge storage in the storage capacitor. At room temperature, the reported mean value of the noise with similar pixel size as the one used in the simulation was ~1.6 fC/pixel.[36] The total number of visible photons collected to form the image shown in Fig. 3-22 (b) was 4.7 x 10^9. Hence, by simple calculation, the average stored signal charge is 46 fC/pixel, and the electronic thermal noise is not significant. Nevertheless, to be conservative, a Gaussian noise

with a mean value of 2 fC/pixel was added to the image in Fig. 3-22 (b) and the resultant image is shown in Fig. 3-23. This image was used as an input image in the image restoration which is discussed in the next section.

3.4.2 Image Restoration

The image obtained with the type B a-Si:H based gamma camera, which is shown in Fig. 3-23, is degraded by the scatterings in the phantom and noise. Even conventional gamma cameras have scattering effects depending on the size of the energy window and there have been many approaches to minimize the scattering effects. Most of the methods require the information of the energy spectra of the detected γ-rays. However, as the energy spectra of the detected γ-rays are unavailable in type B a-Si:H based gamma camera, a deconvolution method was used for image restoration.
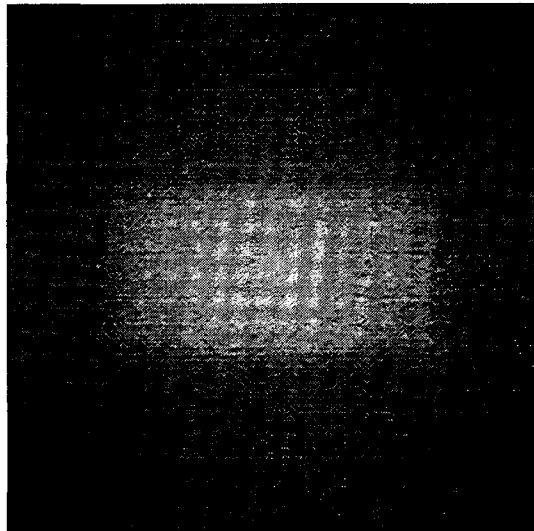
Fig. 3-23   Image obtained with type B a-Si:H based gamma camera with added electronic noise. A Gaussian noise with a mean value of 2 fC/pixel was added to the image in Fig. 3-22 (b).

The image in Fig. 3-23 can be mathematically expressed as

$$g(x,y) = h(x,y)*f(x,y) + n(x,y) \qquad (3\text{-}11)$$

where, $g(x,y)$ is the obtained image in Fig. 3-23, $f(x,y)$ is the true object image in Fig. 3-22 (a), $h(x,y)$ is the PSF of the system which contains the blurring effect due to the scattering in the phantom and camera resolution, and $n(x,y)$ is the noise which was discussed in the previous section. "*" in Eq. (3-11) denotes convolution. Using a deconvolution theorem Eq. (3-11) can be expressed in frequency domain as

$$G(u,v) = H(u,v)F(u,v) + N(u,v) \qquad (3\text{-}12)$$

where, $G(u,v)$, $H(u,v)$, $F(u,v)$ and $N(u,v)$ is a Fourier transformation of $g(x,y)$, $h(x,y)$, $f(x,y)$ and $n(x,y)$, respectively. A simple deconvolution using an inverse filter in this case is, of course, not adequate because it will amplify the noise at high frequencies. Even the pseudoinverse filter, which is a stabilized version of the inverse filter, is still sensitive to noise.[38] Wiener filtering is a method of restoring images in the presence of blur as well as noise. This filter produces the minimum mean-square error between the true object image and the restored image and is often used in the image restoration process of nuclear medicine images.[30-32] The Wiener filter in the frequency domain is expressed as

$$WF(u,v) = \frac{1}{H(u,v)} \frac{|H(u,v)|^2}{|H(u,v)|^2 + PN(u,v)/PF(u,v)} \qquad (3\text{-}13)$$

where, $PN(u,v)$ and $PF(u,v)$ is the power spectrum of the noise and the true object image, respectively. As the PSF of the a-Si:H based gamma camera depends on the source depth, as shown in Fig. 3-20, a PSF which is

averaged over the source depth from 5 cm to 11 cm was used to obtain $H(u,v)$ in the filter. Theoretically, the power spectrum of the Poisson noise is a constant and equal to the total number of counts.[30-32] In our case $PN(u,v)$ was set equal to k*M, where M is the total image count and k is an adjustment factor. In order to use the Wiener filter, the information about the object power spectrum is needed, but this is rarely available in nuclear medicine images. In our case the true object power spectrum was estimated from the obtained image by restoring it with a Wiener filter with a constant $PN(u,v)/PF(u,v)$ ratio.[39]

The final restored image is shown in Fig. 3-24. The blurring due to scattering is significantly reduced and the overall image quality is greatly improved compared to the image in Fig. 3-23. The image profile of this image in x-direction is compared to those of the simulated raw images in Fig. 3-25, which shows a reasonable restoration of the blurred image again.
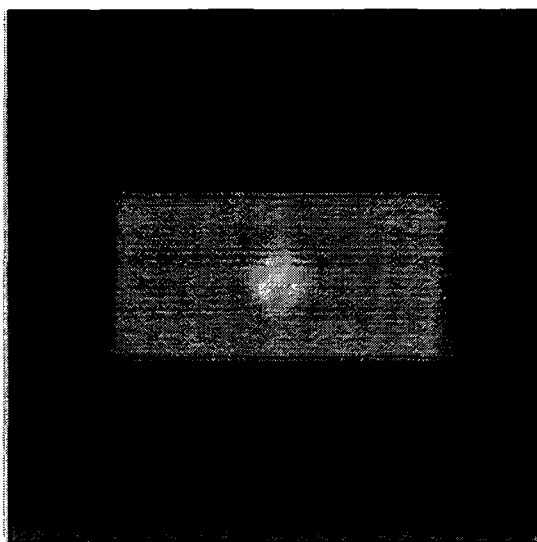
Fig. 3-24   The final restored image using the Wiener filter.
Image in Fig. 3-23 was used as the input image.
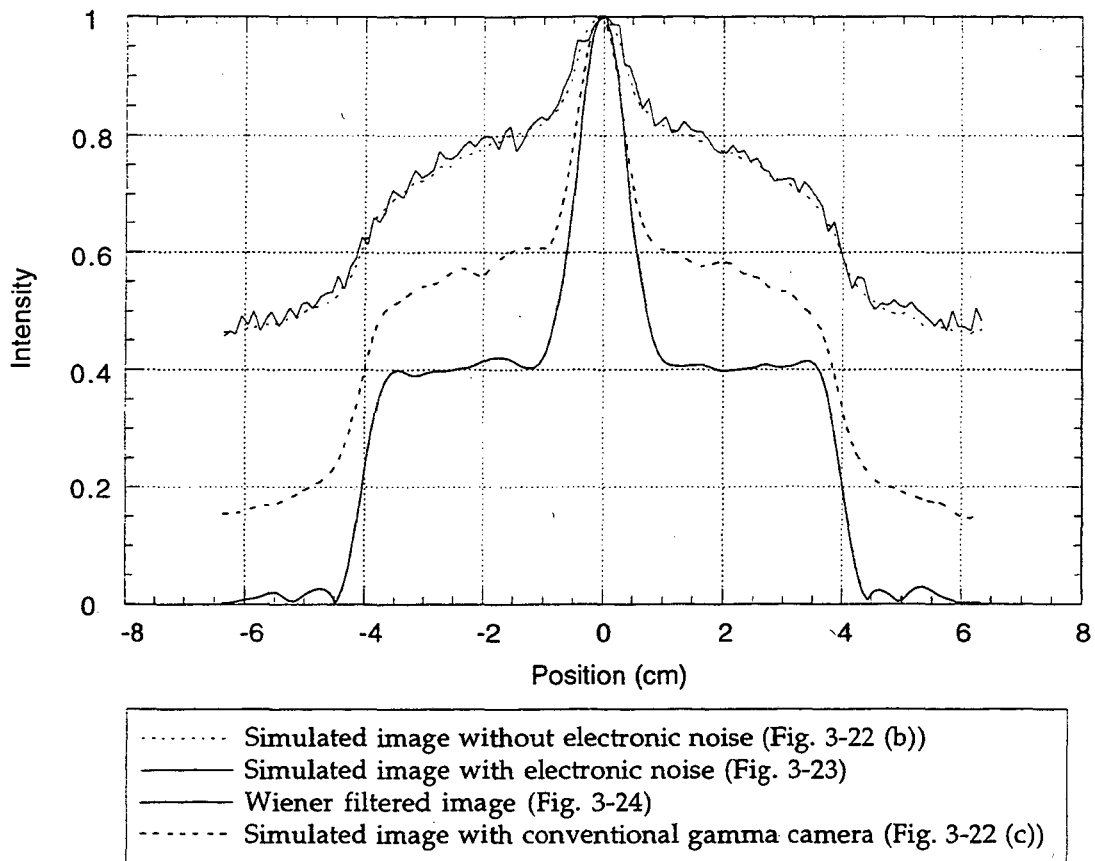
Fig. 3-25   Profiles of images in x-direction. The intensity is
normalized to the maximum count.

In order to test the effect of mismatch in PSF, two PSFs with different source depths were used in the Wiener filter and the profiles of the resulting images are compared in Fig. 3-26 with the one obtained with an averaged PSF. As shown in this figure the restored images are not sensitive to the mismatches in the PSF. This implies an important fact that although a strictly correct PSF is unavailable in real imaging, an approximated PSF can be used.

Finally, in order to be fair, the simulated image with a conventional gamma camera in Fig. 3-22 (c) was also restored using the Wiener filter,
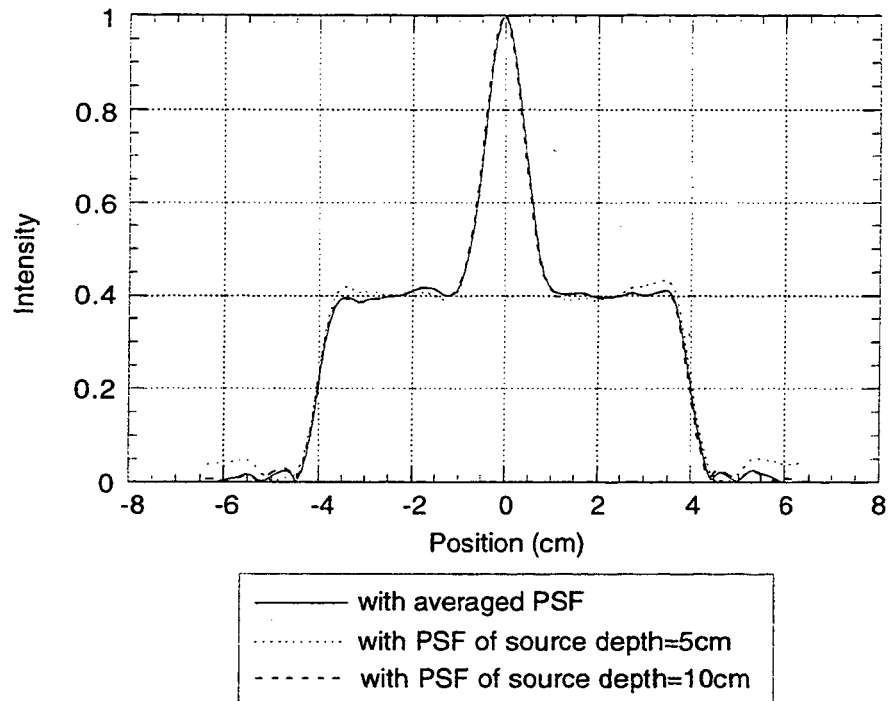
Fig. 3-26   Profiles of restored images using different PSFs. Although PSFs are different depending on the source depth, the restored images are insensitive to the mismatches in the PSFs.

and the profiles of the resultant image is compared in Fig. 3-27 with those of the restored image in Fig. 3-24 and the true object image in Fig. 3-22 (a). The overall qualities of the restored images are similar, but the restored image of the conventional gamma camera shows a somewhat better contrast than the restored image of the type B a-Si:H based gamma camera. This is due to the relatively larger background counts in the image obtained with the type B a-Si:H based gamma camera, as scattered γ photons contribute mostly to the background.
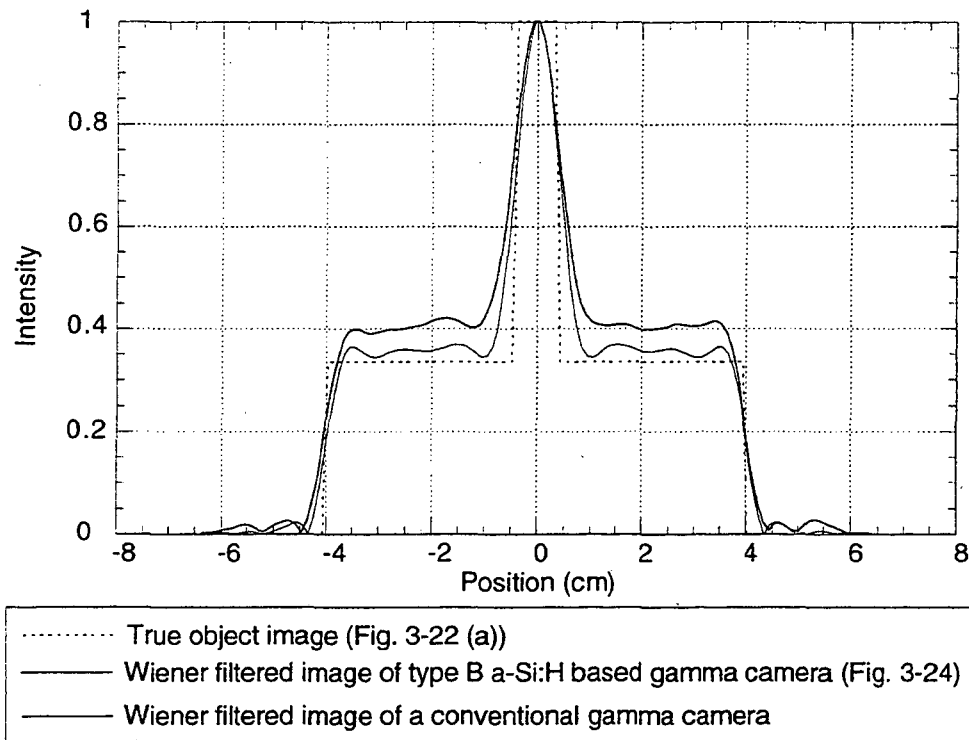
Fig. 3-27   X-directional profiles of the restored images and the
            true object image. The raw images obtained with a
            type B a-Si:H based gamma camera(Fig. 3-23) and
            with a conventional gamma camera(Fig. 3-22 (c))
            were restored using the Wiener filter.

3.5   Discussion

Using technologies similar to those for a-Si:H x-ray imaging arrays,
prototypes of a-Si:H based gamma cameras were conceptually designed and
investigated by Monte Carlo simulations. The proposed a-Si:H based
gamma cameras would have advantages of compactness and light weight
compared to the conventional gamma cameras.

From the Monte Carlo simulations the required thickness of CsI(Tl)
could be estimated such that 2 mm was thick enough for imaging of 70 keV

79

γ's from ^{201}Tl and 5 mm or more was needed for 140 keV γ's from ^{99m}Tc. The intrinsic resolution of a-Si:H based gamma cameras obtained from the simulations was 1 ~ 2.5 mm, which is better than that of the conventional gamma cameras (3 ~ 4 mm).

According to the structures and operation schemes, two types of gamma cameras were proposed. The type A camera with a pixel amplifier in each photodetector would have a similar operation scheme as the conventional gamma cameras and energy selection is also expected to be possible. But the fabrication of this camera is more complicated than the type B camera due to the complexity of the pixel amplifiers. However, the fabrication complexity and cost may be lessened as technology is developed, then the type A a-Si:H based gamma camera would be feasible.

As the type B camera is operated in the integration mode it would not be limited by the high event rate which is sometimes a problem in the conventional gamma cameras. But, it cannot reject the scattered γ-rays, and the blurring effect in the obtained image is inevitable as shown from the Monte Carlo simulations. This blurring, however, can be reduced by using an adequate image restoration method such as Wiener filtering. In the Wiener filtering the averaged PSF of the camera was good enough to restore the blurred raw image as the restoration process is insensitive to the small mismatches in the PSF.

Although the blurring effect due to the γ scattering in the image obtained with the type B a-Si:H based gamma camera could be reduced, the restored image showed a little poorer contrast compared with the restored image of the conventional gamma camera. As the scattering would be

severer when imaging an organ located deeper inside a patient's body, the usage of the type B a-Si:H based gamma camera would be limited to imaging shallow organs such as thyroid or imaging small animals.

References

[1]   R. J. Ott, M. A. Flower, J. W. Babich and P. K. Marsden, "The Physics of Radioisotope Imaging," Chapter 6 in *The Physics of Medical Imaging*, Edited by S. Webb, Adam Hilger, Bristol and Philadelphia (1988)

[2]   H. O. Anger, "Scintillation Camera," Rev. Sci. Instrum., 29, 27 (1958)

[3]   J. A. Sorenson and M. E. Phelps, *Physics in Nuclear Medicine*, 2nd Ed., W. B. Saunders Co., Philadelphia (1987)

[4]   H. K. Lee, J. S. Drewery, W. S. Hong, T. Jing, S. N. Kaplan, A. Mireshghi and V. Perez-Mendez, "Hydrogenated Amorphous Silicon (a-Si:H) Based Gamma Camera - Monte Carlo Simulations," SPIE Vol. 2163, Medical Imaging 1994: Physics of Medical Imaging, 427 (1994)

[5]   H. K. Lee, G. Cho, J. S. Drewery, W. S. Hong, T. Jing, S. N. Kaplan, A. Mireshghi, V. Perez-Mendez and D. Wildermuth, "New a-Si:H Photo-Detectors for Long-Term Charge Storage," Mat. Res. Soc. Symp. Proc., 297, 1023 (1993)

[6]   W. B. Jackson and M. D. Moyer, "Creation of Near-Interface Defects in Hydrogenated Amorphous Silicon-Silicon Nitride Heterojunction: the Role of Hydrogen," Phys. Rev., B36, 6217 (1987)

[7]   G. Cho, J. S. Drewery, W. S. Hong, T. Jing, S. N. Kaplan, H. K. Lee, A. Mireshghi, V. Perez-Mendez and D. Wildermuth, "Signal Readout in a-Si:H Pixel Detectors," IEEE Trans. Nuc. Sci., 40, 323 (1993)

[8]   R. Sinclair, A. H. Carim, J. Morgiel and J. C. Bravman, "Microstructures of Polysilicon," Mat. Res. Soc. Symp. Proc., 106, 27 (1988)

[9]   T. I. Cox, V. G. I. Deshmukh, J. R. Hill, H. C. Webber, N. G. Chew and A. G. Cullis, "Electrical and Structural Properties of Pulse

Laser-Annealed Polycrystalline Silicon Films," IEEE Trans. Elect. Devices, ED-30, 737 (1983)

[10] T. Kamins, "Deposition and Characteristics of Polysilicon Films for Integrated-Circuit Applications," Mat. Res. Soc. Symp. Proc., 106, 3 (1988)

[11] T. Noguchi, H. Hayashi and T. Ohshima, "Polysilicon Super Thin Film Transistor Technology," Mat. Res. Soc. Symp. Proc., 106, 293 (1988)

[12] H. Kuriyama, T. Kuwahara, K. Wakisaka, S. Kiyama, S. Tsuda and S. Nakano, "High-Quality Poli-Si Films Using An Excimer Laser Annealing Method for Giant-Microelectronics Application," Presented at the Electrochemical Society 186th Meeting at Miami in Oct. (1994)

[13] I. Fujieda, S. Nelson, P. Nylen, R. A. Street and R. L. Weisfield, "Two Operation Modes of 2D a-Si Sensor Arrays for Radiation Imaging," J. Non-Crystalline Solids, 137&138, 1321 (1991)

[14] I. Fujieda, S. Nelson, R. A. Street and R. L. Weisfield, "Radiation Imaging with 2D a-Si Sensor Arrays," IEEE Trans. Nucl. Sci., 39, 1056 (1992)

[15] G. Cho, M. Conti, J. S. Drewery, I. Fujieda, S. N. Kaplan, V. Perez-Mendez, S. Qureshi and R. A. Street, "Assessment of TFT Amplifiers for a-Si:H PIXEL Particle Detectors," IEEE Trans. Nucl. Sci., 37, 1142 (1990)

[16] R. A. Street, R. Weisfield, S. Nelson, P. Nylen and X. D. Wu, "Page Sized a-Si:H 2-Dimensional Imaging Arrays," Mat. Res. Soc. Symp., 297, 957 (1993)

[17] L. E. Antonuk, J. Boudry, W. Huang, D. L. McShan, E. J. Morton and J. Yorkston, "Demonstration of Megavoltage and Diagnostic X-Ray Imaging with Hydrogenated Amorphous Silicon Arrays," Med. Phys., 19, 1455 (1992)

[18]   L. E. Antonuk, J. Yorkston, W. Huang, J. Boudry, E. J. Morton and R. A. Street, "Large Area Flat-Panel a-Si:H Arrays for X-Ray Imaging," SPIE Vol. 1896, Medical Imaging 1993: Physics of Medical Imaging, 18 (1993)

[19]   L. E. Antonuk, J. Boudry, Y. El-Mohri, W. Huang, J. Siewerdsen, J. Yorkston and R. A. Street, "A High Resolution, High Frame Rate, Flat-Panel TFT Array for Digital X-Ray Imaging," SPIE Vol. 2163, Medical Imaging 1994: Physics of Medical Imaging, 118 (1994)

[20]   E. Browne, J. M. Dairiki, R. E. Doebler, A. A. Shihab-Eldin, L. J. Jardine, J. K. Tuli and A. B. Buyrn, *Table of Isotopes*, 7th Ed., Edited by C. M. Lederer and V. S. Shirley, John Wiley & Sons, Inc., New York (1978)

[21]   I. Holl, E. Lorenz and G. Mageras, "A measurement of the Light Yield of Common Inorganic Scintillators," IEEE Trans. Nuc. Sci., 35, 105 (1988)

[22]   J. J. Fitzgerald, G. L. Brownell and F. J. Mahoney, *Mathematical Theory of Radiation Dosimetry*, Gordon and Breach Science Pub., Inc., New York (1967)

[23]   I. Lux and L. Koblinger, *Monte Carlo Particle Transport Methods: Neutron and Photon Calculations*, CRC Press, Boca Raton (1990)

[24]   R. D. Evans, *The Atomic Nucleus*, McGraw-Hill Book Comp., Inc., New York (1955)

[25]   H. Kahn, "Applications of Monte Carlo," AECU-3259 Report, Rand Corporation, Santa Monica (1954)

[26]   Picker Inc., *Specifications of Picker Low-Energy Parallel-Hole Collimators,*

[27]   P. Msaki, B. Axelsson and S. A. Larsson, "Some Physical Factors Influencing the Accuracy of Convolution Scatter Correction in SPECT," Phys. Med. Biol., 34, 283 (1989)

[28] Siemens Inc., "ZLC 370/750 series : Collimator Performance Specifications," *Gamma Camera Catalogue.*

[29] N. H. Clinthorne, "Are Hydrogenated Amorphous Silicon Arrays Usable for Tomographic Imaging?," IEEE Trans. Nucl. Sci., 41, 1516 (1994)

[30] M. A. King, P. W. Doherty and R. B. Schwinger, "A Wiener Filter for Nuclear Medicine Images," Med. Phys. 10, 876 (1983)

[31] M. T. Madsen, "A Method for Obtaining An Approximate Wiener Filter," Med. Phys., 17, 126 (1990)

[32] B. C. Penney, S. J. Glick and M. A. King, "Relative Importance of the Error Sources in Wiener Restoration of Scintigrams," IEEE Trans. Medical Imaging, 9, 60 (1990)

[33] M. J. Belanger, A. B. Dobrzeniecki and J. C. Yanch, "Noise Characteristics of a SPECT Simulation System," Presented at IEEE Nuclear Science Symposium and Medical Imaging Conference, San Francisco, November (1993)

[34] R. A. Street, S. Nelson, L. Antonuk and V. Perez-Mendez, "Amorphous Silicon Sensor Arrays for Radiation Imaging," Mat. Res. Soc. Symp. Proc., 192, 441 (1990)

[35] G. Cho, S. Qureshi, J. S. Drewery, T. Jing, S. N. Kaplan, H. K. Lee, A. Mireshghi and D. Wildermuth, "Noise in a-Si:H p-i-n Detector Diodes," IEEE Trans. Nucl. Sci., 39, 641 (1992)

[36] I. Fujieda, S. Nelson, R. A. Street and R. L. Weisfield, "Characteristics of a-Si Pixel Arrays for Radiation Imaging," Mat. Res. Soc. Symp. Proc., 219, 537 (1991)

[37] I. Fujieda, R. A. Street, R. L. Weisfield, S. Nelson, P. Nylen, V. Perez-Mendez and G. Cho, "High Sensitivity Readout of 2D a-Si Image Sensors," Jpn. J. Appl. Phys., 32, 198 (1993)

[38] A. K. Jain, *Fundamentals of Digital Image Processing*, Prentice-Hall International, Inc., Englewood (1989)

[39] T. R. Miller and K. S. Sampathkumaran, "Design and Application of Finite Impulse Response Digital Filters," Eur. J. Nucl. Med., 7, 22 (1982)

Chapter 4   Long-Term Charge Storage in a-Si:H Pixels

4.1   Introduction

In Chapter 3, an a-Si:H based gamma camera which is operated in the integration mode (type B) was proposed. Each pixel in this camera is composed of a normal a-Si:H p-i-n photodiode and a storage capacitor (see Fig. 3-9). The purpose of the capacitor is to store and accumulate the signal charge, which is generated in the intrinsic region of the p-i-n photodiode by the light coming from the scintillator, until it is big enough not to be embedded in the noise. During the γ scan, however, as the photodiode is reverse biased, dark reverse current will flow even without the scintillation light. As the photodiode is connected to the storage capacitor in series, the signal charge as well as the background charge due to the dark current in the photodiode cannot get out of the pixel but accumulates on the storage capacitor. If accumulation of the background charge is satisfactorily small during the γ scan, we can easily measure the true signal from the obtained signal simply by subtraction of the thermal generation charge, which is measured separately without γ sources for the same γ scan period. If this is not the case, however, the maximum γ scan period is limited by the accumulation of the background charge.

In order to determine the conditions under which the proposed type B a-Si:H based gamma camera can work in an integration mode with an appropriate integration time, test pixels which consist of a-Si:H p-i-n photodiodes and capacitors were made and signal charge storing performance was investigated.

87

In this chapter, the results obtained from the experiments on test devices and theoretical analyses of the dark current are discussed in connection with the charge storage time. It will be shown that the principal source of the dark current in a reverse biased a-Si:H p-i-n diode is from thermal generation of charge carriers in the bulk i-region, that this thermally induced dark current is the limiting factor for the charge storing detector operation, and that it can be made sufficiently small for a successful operation over a wide and linear dynamic range of signal.

4.2   Theory of Dark Reverse Current in a-Si:H p-i-n Diodes

The sources of the dark current in a reverse biased a-Si:H p-i-n diode are bulk thermal generation current, contact injection current and edge leakage current.[1] The injection current density can be expressed as[2]

$$J_{inj} = A^* T^2 \exp\left(-\frac{q\phi_B}{kT}\right) \tag{4-1}$$

where, A^* is the effective Richardson constant and ϕ_B is the barrier height. For the Schottky diodes, the contact injection current is usually higher than the thermal generation current because the barrier height is low. But for a-Si:H p-i-n diodes, as the barrier height is high the contact injection current is negligible. However, if the p- or n- layer is too thin, the contact injection current may flow by tunneling. For well fabricated devices, the edge leakage current is seldom a problem, and for large area devices, this current can be neglected also because the edge current is proportional to the perimeter, while the bulk thermal generation current or the contact injection current is proportional to the device area. In a-Si:H p-i-n diodes,

the thermal generation current in the bulk of the i-layer is considered to be the dominant source of the dark reverse current. This thermal generation current is due to the thermal emission of electrons and holes from the deep states. In the following subsections, the thermal generation current is discussed in connection with the field enhancement effects.

4.2.1 Thermal Generation Current without Field Enhancement

A simple thermal generation current model can be developed using Shockley-Read-Hall formalism and several assumptions[1,3]. Based on the SRH model, the thermal emission rate of electrons from a single generation center is

$$e_n(E_t) = \omega_o \exp\left(-\frac{E_c - E_t}{kT}\right) , \qquad (4\text{-}2)$$

where E_t is the energy level of the generation center and ω_o is the attempt-to-escape frequency given by $\omega_o = \sigma_n \langle v_n \rangle N_c kT$ where σ_n is the electron capture cross section of the states at E_t, $\langle v_n \rangle = (3kT/m)^{1/2}$ is the average thermal velocity of electrons in the conduction band and N_c is the conduction band density of states. Usually, ω_o is in the range of $10^{11} \sim 10^{13}$ sec^{-1}[4]. The generation centers, which are mainly dangling bonds in a-Si:H, are distributed in energy between the conduction band and the valence band. And the number of electrons occupying the defect states of an energy level E_t is $N(E_t)f(E_t)$ where $N(E_t)$ is the density of the defect states at E_t and $f(E_t)$ is the Fermi distribution function. Hence, the total thermal emission rate of electrons from the recombination centers per unit volume is

$$\int_{E_v}^{E_c} N(E) f(E) e_n(E) \, dE \quad .$$

(4-3)

In steady state, the thermal generation is dominated by the emission from the generation centers located within kT of the quasi-Fermi energy level E_{Fq}.[3,5] For these traps the emission rates of electrons and holes are equal, and the quasi-Fermi level E_{Fq} can be calculated by simply setting the emission rate for electrons equal to the hole emission rate,[1]

$$E_{Fq} = \frac{E_g}{2} + \frac{kT}{2} \ln \frac{\omega_p}{\omega_n} \quad ,$$

(4-4)

where E_g is the mobility gap of a-Si:H, and ω_p and ω_n is the attempt-to-escape frequency of holes and electrons, respectively. Assuming that the density of states is constant within kT of E_{Fq}, Eq. (4-3) can be simplified as

$$\int_{E_v}^{E_c} N(E) f(E) e_n(E) \, dE$$
$$\approx N_g kT e_n(E_{Fq})$$

(4-5)

where N_g is the density of states at E_{Fq}.

With sufficiently high reverse bias, the diffusion current can be neglected and full collection of the generated carriers by the depletion field without recombination can be assumed. In this case, using Eq. (4-5), the thermal generation current can be expressed as

$$I_{tho} = q A \int_0^d N_g(x) kT \left[e_n(E_{Fq}, x) \frac{d-x}{d} + e_p(E_{Fq}, x) \frac{x}{d} \right] dx \quad ,$$

(4-6)

where q is the charge of an electron, A is the area of the diode, d is the thickness of the diode, $e_n(E_{Fq}, x)$ and $e_p(E_{Fq}, x)$ is the emission rate of electrons and holes from the generation centers located at E_{Fq} and x. As

the emission rates for electrons and holes are equal at E_{Fq}, Eq. (4-6) can be simplified further as

$$I_{tho} = q \ A \ kT \int_0^d N_g(x) \, e_n(E_{Fq}, x) \, dx \ .$$

(4-7)

Now, with the assumption of spatially uniform generation centers and quasi-Fermi level within the i-region, the thermal generation current in steady state can be expressed as

$$
\begin{aligned}
I_{tho} &= q \, A \, d \, N_g \, kT \, e_{no} \\
&= q \, A \, d \, N_g \, kT \, \omega_o \exp\!\left(-\frac{E_i}{kT}\right) ,
\end{aligned}
$$

(4-8)

where E_i is the difference between the conduction band and the quasi-Fermi level E_{Fq}, and e_{no} is the thermal emission rate from the generation centers located at E_{Fq}, which is given by

$$e_{no} = \omega_o \exp\!\left(-\frac{E_i}{kT}\right) \ .$$

(4-9)

Of course, Eq. (4-8) cannot explain the voltage-dependent current behavior in a-Si:H p-i-n diodes (see Fig. 4-1, for example), as this model does not include the effect of the electric field, but at low field this equation is a good approximation to explain the temperature dependence of dark current behavior.[3]

4.2.2 Thermal Generation Current with Field Enhancement

When a reverse bias is applied on a-Si:H p-i-n diode, a depletion region forms in the i-layer and the thermal emission process is enhanced by the imposed electric field. The effect of the reverse bias on thermal

generation current is shown in Fig. 4-1. In this figure the thermal generation current is plotted as a function of time after applying various reverse biases. During the depletion period, the current decreases and finally it reaches a steady state. The dependence of the steady state thermal generation current on the applied reverse bias is apparent.

The enhancement of thermal generation current by the reverse bias is due to the lowering of the potential barrier of the generation centers and tunneling effect.[6] The change in the potential barrier when an electric field is applied is schematically shown in Fig. 4-2. When no field is present, an electron in the generation center sees a Coulomb potential barrier which is symmetric in all directions (Fig. 4-2 (a)), but with the external field which is imposed by the reverse bias, the potential barrier loses its symmetry and
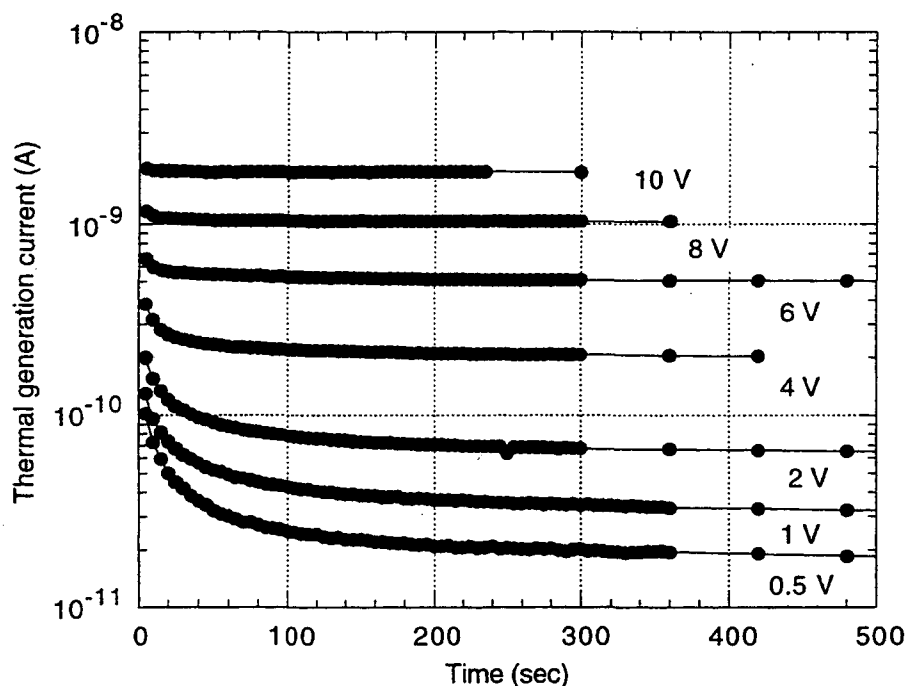
Fig. 4-1   Thermal generation current in a 1 μm a-Si:H p-i-n diode as a function of time after applying various reverse biases. After depletion process the thermal generation current reaches steady state and its steady state value is dependent on the reverse bias.

92

$$q\varphi_{Coulomb}(x) = -\frac{q^2}{4\pi\varepsilon x} \qquad q\varphi_{external}(x) = -qFx \qquad q\varphi_{final}(x) = -\frac{q^2}{4\pi\varepsilon x} - qFx$$

(a)   (b)   (c)

Fig. 4-2   The potential barrier change with an external field. (a) is the Coulomb potential barrier before the external field is applied, (b) is the potential due to a uniform external field and (c) is the final potential barrier shape which is a superimposition of (a) and (b). The barrier height is lowered by ΔE in x-direction.

is lowered in x-direction (Fig. 4-2 (c)). There are three types of thermal emission which are assisted by the external electric field: (1) Poole-Frenkel effect, (2) tunneling, and (3) phonon assisted tunneling.[1,6-8] These emission processes are schematically shown in Fig. 4-3.

a)   <u>Poole-Frenkel Effect</u>

The maximum barrier height of the lowered potential barrier in Fig. 4-2 (c) is located x_o from the center, where x_o can be simply calculated as $x_o = (q/4\pi\varepsilon_{Si}F)^{1/2}$, where ε_{Si} is the dielectric constant of a-Si:H and F is the external electric field. Hence, the lowering of the barrier height ΔE at x_o can be obtained using the equation in the inset of Fig. 4-2 (c) and is

$$\Delta E = \sqrt{\frac{q^3 F}{\pi\varepsilon_{Si}}} = \beta_{PF}\sqrt{F} \quad , \tag{4-10}$$

Fig. 4-3   The three emission processes which are enhanced
by the external electric field.

where $\beta_{PF} = (q^3 / \pi \varepsilon_{Si})^{1/2}$ is the Poole-Frenkel constant. Due to this barrier lowering by ΔE, an electron with an energy between E_c and $E_c - \Delta E$ is considered to be in the conduction band. Therefore, the emission rate in x-direction is increased by a factor of $\exp(\Delta E / kT)$, which is called the Poole-Frenkel effect. The resulting enhanced thermal emission rate is given by

$$(e_n)_{PF} = e_{no} \exp\left(\frac{\Delta E}{kT}\right) , \tag{4-11}$$

where e_{no} is the thermal emission rate when no electric field is present and is given in Eq. (4-9). The expression in Eq. (4-11) is derived for one-dimension. The three-dimensional emission rate can be obtained by an integration over the whole space and can be expressed as[9]

$$(e_n)_{PF} = e_{no} \left\{ \left(\frac{kT}{\Delta E}\right)^2 \left[1 + \left(\frac{\Delta E}{kT} - 1\right)\exp\left(\frac{\Delta E}{kT}\right)\right] + \frac{1}{2} \right\} . \tag{4-12}$$

Assuming spatially uniform electric field, the thermal generation current by Poole-Frenkel effect with one-dimensional case can be expressed as

$$I_{thPF} = I_{tho} \exp\left(\frac{\Delta E}{kT}\right)$$

$$= q\,A\,d\,N_g\,kT\,\omega_o \exp\left(-\frac{E_i - \beta_{PF}\sqrt{F}}{kT}\right) \quad , \tag{4-13}$$

where I_{tho} is the thermal generation current obtained without considering the field enhancement effect, and is given in Eq. (4-8). In the depletion region of a-Si:H, however, the electric field is not uniform due to the positive space charge. It is a linear function of distance from the p-i interface and has a maximum magnitude (F_M) at the p-i interface and a minimum magnitude (F_m) at the n-i interface as shown in Fig. 4-4. Assuming the reverse bias V_d is higher than the voltage for full depletion, the field is expressed as

$$F(x) = F_o\left(\frac{1}{2} - \frac{x}{d}\right) + \frac{V_d}{d} \quad , \tag{4-14}$$

where $F_o = qdN_d^*/\varepsilon_{Si}$ is the field at the p-i interface when the i-region is just
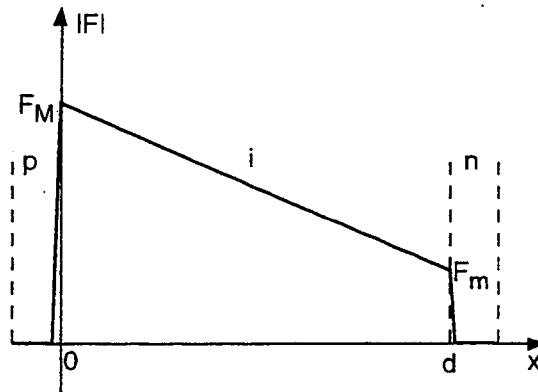
Fig. 4-4 Electric field shape in a-Si:H p-i-n diode when a reverse bias V_d is more than enough to fully depleted the i-region. Its magnitude is maximum at p-i interface and is a linear function of distance.

fully depleted, and N_d^* is the ionized dangling bond density. Including the spatial dependence of the field, the thermal generation current with Poole-Frenkel effect can be derived as

$$I_{thPF} = \frac{I_{tho}}{d} \int_0^d \exp\left(\frac{\beta_{PF}\sqrt{F(x)}}{kT}\right) dx$$

$$= \frac{2I_{tho}}{F_o\gamma^2}\left[\left(\gamma\sqrt{F_M} - 1\right)\exp\left(\gamma\sqrt{F_M}\right) - \left(\gamma\sqrt{F_m} - 1\right)\exp\left(\gamma\sqrt{F_m}\right)\right] \qquad , \quad (4\text{-}15)$$

where $F_M = V_d/d + F_o/2$, $F_m = V_d/d - F_o/2$ and $\gamma = \beta_{PF}/kT$.

The calculated thermal generation current with Poole-Frenkel effect is compared with measurements in Fig. 4-5. With high biases ($V_d > 2$ V), both of Eq. (4-13) and (4-15) fit the measured values well, but with lower biases, as the electric field is less uniform, the current calculated using Eq. (4-13) cannot fit the measured current, while Eq. (4-15), which was derived considering the non uniform field effect, can fit the measured current behavior in the whole voltage region. $N_d^* = 7 \times 10^{14}$ cm^{-3} and $E_i = 0.9$ V was assumed and $\beta_{PF} = 0.038$ eV/$\sqrt{V/\mu m}$ was used to fit the measured current shape. The value of β_{PF} is about 1.7 times larger than the theoretical value of 0.022, which may be interpreted that the Poole-Frenkel effect is enhanced because the surrounding generation centers give screening effect resulting in lowering of the barrier height further.[8]

b)   Tunneling

At high field the width of the potential barrier can be reduced so that an electron can penetrate through the barrier by tunneling. This process is specially important at low temperature where the probability of thermal
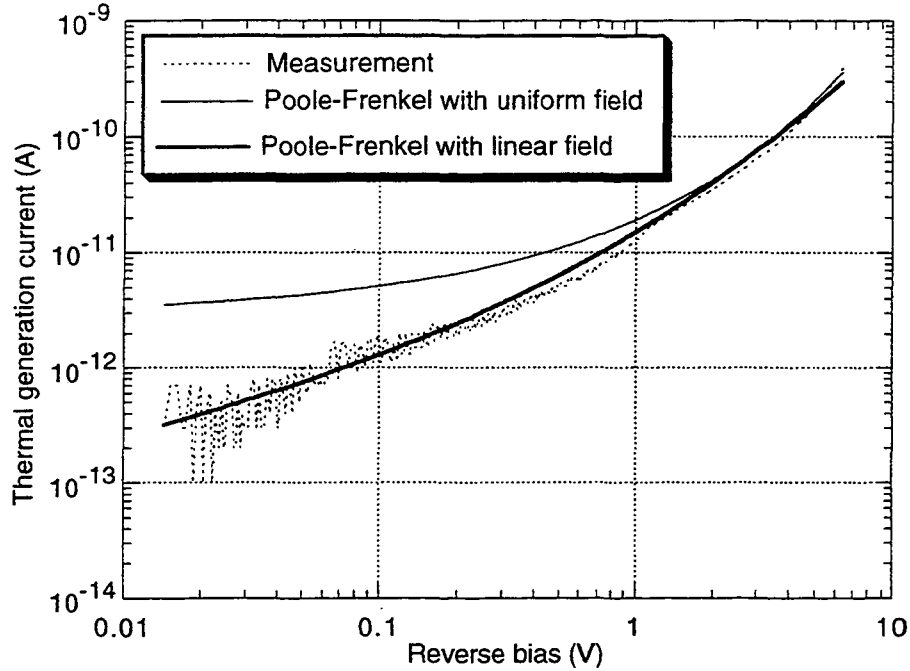
Fig. 4-5   Measured and calculated thermal generation
currents as functions of reverse bias for a 1μm thick
a-si:H p-i-n diode.

emission is low. The pure tunneling is independent of temperature and is
isoenergetic transition from the ground state of the generation center to the
conduction band.[7]   The tunneling rate is proportional to the barrier
transparency factor B, which is expressed using the WKB approximation
as[8, 10,11]

$$B = \exp\left\{-\frac{4\pi}{h}\int [2m(V(x)-E)]^{1/2}\,dx\right\} .$$ (4-16)

The tunneling rate $(e_n)_{TU}$ for one-dimensional Dirac potential well
was derived by Korol and is given by[12]

$$(e_n)_{TU} = \left(\frac{U}{3\hbar}\right)\left(\frac{U}{E_i}\right)^{1/2}\exp\left[-\left(\frac{E_i}{U}\right)^{3/2}\right] ,$$ (4-17)

where the characteristic energy U is defined as

$$U = \left(\frac{3q\hbar F}{4\sqrt{2m^*}} \right)^{2/3} \quad , \tag{4-18}$$

where $\hbar$ is the Planck constant and m^* is the effective mass of an electron which is about $0.4m_e$ in a-Si:H.[13] For a-Si:H, U is about $(2.32\text{x}10^{-4}\ F)^{2/3}$ [eV], where F is in [V/μm]. The expression in Eq.(4-17) is, however, not completely correct to use with a-Si:H because in a-Si:H, the generation centers induce Coulomb potential wells. For Coulomb wells, the tunneling rate was derived by Rosencher[7] with modification of the barrier transparency factor, and for one-dimensional well it is given by

$$(e_n)_{TU} = \left(\frac{U}{3\hbar} \right)\left(\frac{U}{E_i} \right)^{1/2} \exp\left\{ -\left(\frac{E_i}{U} \right)^{3/2}\left[1 - \left(\frac{\Delta E}{E_i} \right)^{5/3} \right] \right\} \quad . \tag{4-19}$$

For three-dimensional Coulomb well, the emission rate by tunneling is

$$(e_n)_{TU} = \left(\frac{U}{6\hbar} \right)\left(\frac{U}{E_i} \right)^{2} \exp\left\{ -\left(\frac{E_i}{U} \right)^{3/2}\left[1 - \left(\frac{\Delta E}{E_i} \right)^{5/3} \right] \right\} \quad . \tag{4-20}$$

Actually, there is no significant difference in the resulting value whether Eq. (4-17) or (4-19) is used for thin a-Si:H p-i-n diodes, because the value of $\Delta E/E_i$ in Eq. (4-19) is very small, but for thick diodes with high electric field, this term cannot be neglected.

c)   Phonon Assisted Tunneling

Phonon assisted tunneling is an emission process which is a combination of Poole-Frenkel effect and pure tunneling. In this process an electron is excited to an energy level E by phonon coupling and this electron tunnels through the thin potential barrier, as shown in Fig. 4-3. The rate of

98

excitation to E is (note that the reference level of E is the conduction band not the valence band)

$$e_n(E) = \omega_o \exp\left(-\frac{E_i - E}{kT}\right) \ . \tag{4-21}$$

Hence, the rate for electrons to jump to this energy level followed by tunneling is

$$\begin{aligned}
e'_n(E) &= e_n(E) \exp\left\{-\left(\frac{E}{U}\right)^{3/2}\left[1 - \left(\frac{\Delta E}{E}\right)^{5/3}\right]\right\} \\
&= \omega_o \exp\left\{-\frac{E_i - E}{kT} - \left(\frac{E}{U}\right)^{3/2}\left[1 - \left(\frac{\Delta E}{E}\right)^{5/3}\right]\right\} \ .
\end{aligned} \tag{4-22}$$

By integrating Eq. (4-22) over the whole depth of the potential well the emission rate by phonon assisted tunneling can be obtained as[7]

$$(e_n)_{PAT} = \frac{e_{no}}{kT} \int_{\Delta E}^{E_i} \exp\left\{\frac{E}{kT} - \left(\frac{E}{U}\right)^{3/2}\left[1 - \left(\frac{\Delta E}{E}\right)^{5/3}\right]\right\} dE \tag{4-23}$$

for one-dimensional well, and for three-dimensional well,

$$(e_n)_{PAT} = \frac{e_{no}}{2kT} \int_{\Delta E}^{E_i} \left(\frac{U}{E}\right)^{3/2} \exp\left\{\frac{E}{kT} - \left(\frac{E}{U}\right)^{3/2}\left[1 - \left(\frac{\Delta E}{E}\right)^{5/3}\right]\right\} dE \ . \tag{4-24}$$

The thermal emission rates by the previous three emission processes are compared in Fig. 4-6 and 4-7 with varying reverse bias and temperature, respectively. At room temperature, the pure tunneling process is negligible even at very high field. In the operation range of < ~10 V for 1 μm thick a-Si:H p-i-n diodes, the Poole-Frenkel process is most dominant as shown in Fig. 4-6. With a reverse bias of 5 V on 1 μm thick diode, the tunneling effect cannot be seen in Fig. 4-7, and for the whole temperature region, the emission rate by the Poole-Frenkel effect is higher
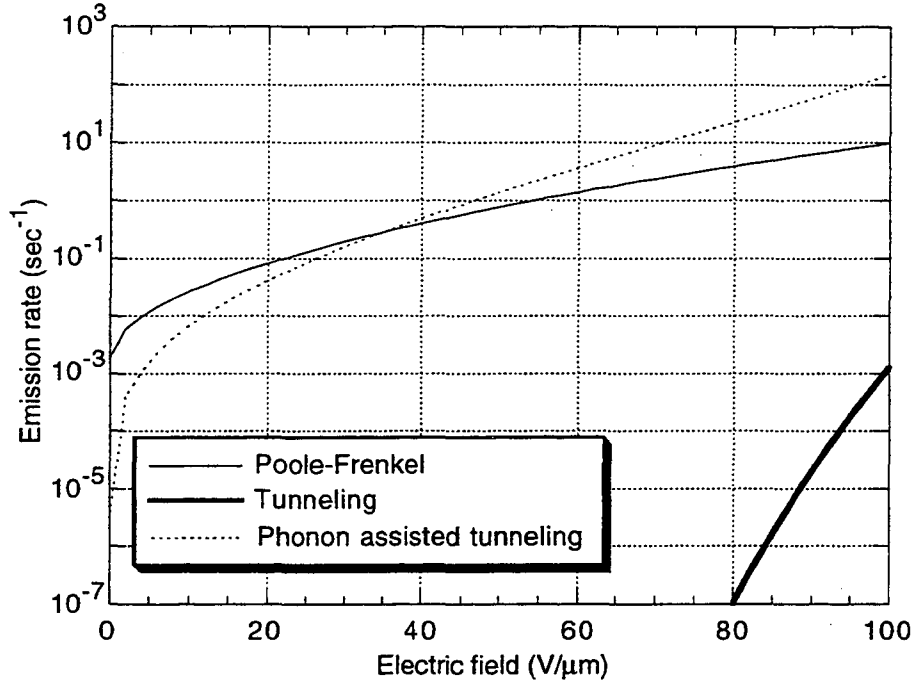
Fig. 4-6   Calculated emission rates of Poole-Frenkel effect,
            tunneling and phonon assisted tunneling as
            functions of electric field. 1 μm thick a-Si:H p-i-n
            diode with $E_i = 0.9V$ at room temperature was used.

than phonon assisted tunneling, which, however, cannot be neglected since it contributes about 10% of the whole emission processes. The ratio of the emission rate at room temperature to at -40 °C is about four orders of magnitude, indicating the thermal generation process significantly depends on the temperature, hence the thermally generated background charge in the photodetector pixel can be reduced remarkably at low temperatures, as confirmed from the experiments in Section 4.4.

From the above discussions, the Poole-Frenkel process is the dominant source of the thermal generation with our operating biases and temperatures, and the equation based on this single process could fit the measurements (see Fig. 4-5) with slight modification in β_{PF}.
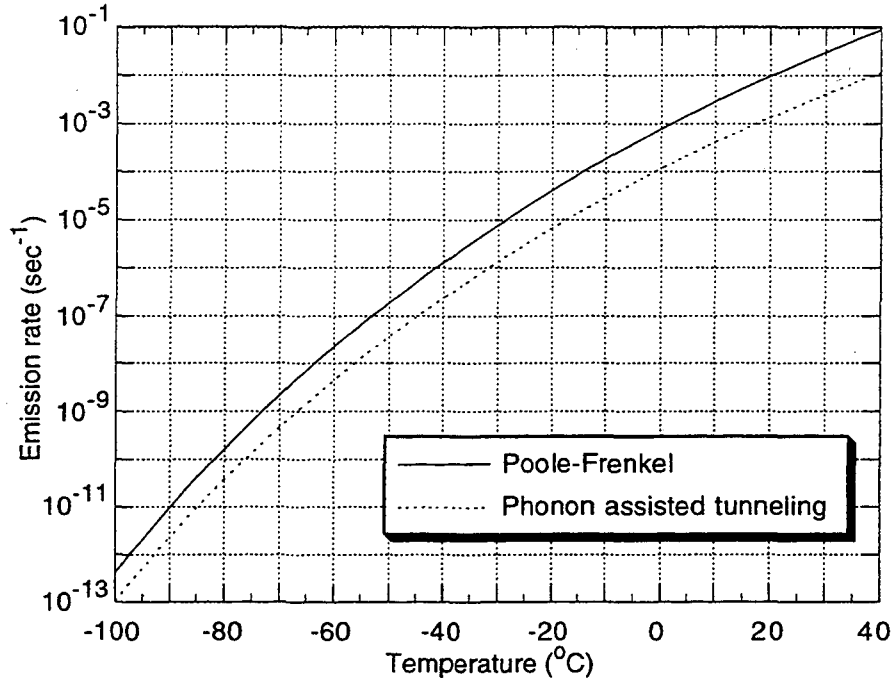
Fig. 4-7 Temperature effect on Poole-Frenkel emission and
phonon assisted tunneling. 1 μm thick a-Si:H p-i-n
diode with E_i = 0.9 V with a reverse bias of 5 V was
used. In the range of the temperature shown, the
pure tunneling process cannot be seen with this
bias.

4.3   Experimental

In the experiments, temperature effect on the thermal generation
current, accumulation of thermally generated background charge on the
storage capacitor and signal charge collection after long storage periods
were tested with sample devices.

4.3.1 Devices

The test devices were fabricated using the PECVD technique. The
structure of the test devices is shown in Fig.4-8. The thicknesses of the p, n
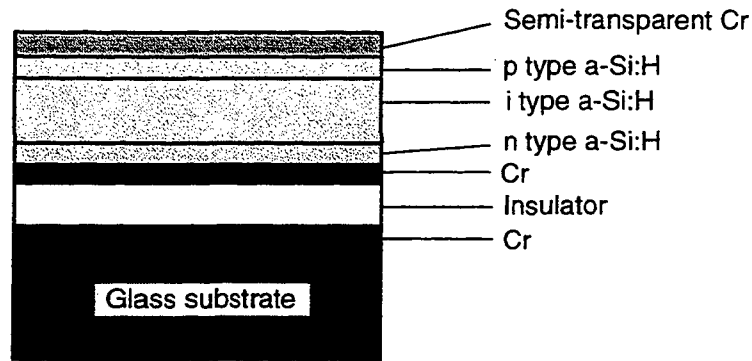
Fig. 4-8   A schematic diagram of the test pixel. The thickness of the p-i-n photodiode is ~1μm and 200 ~ 300 nm SiO_2 or Si_3N_4 was used for the insulator material. The area of the pixel is 0.11 cm^2.

and i-layers were 30 nm, 20 nm and 1 μm, respectively. The top Cr contact was made thin for light penetration and had a circular shape . The storage capacitor was composed of Cr, insulator and Cr. Oxide (SiO_2) or nitride (Si_3N_4) was used as the insulator. The thickness of the insulator was made thin (200 ~ 300 nm) in order to make the storage capacitor have a high capacitance so that it could accommodate large amount of charge and also the divided voltage across the p-i-n photodiode could be high. The capacitance of the insulator, C_i, was 2400 ~ 3900 pF and that of the p-i-n photodiode, C_d, was ~1150 pF for a pixel area of 0.11 cm^2.

4.3.2 Experimental System

The principle of signal charge storage and the experimental system are schematically shown in Fig.4-9. In order to simulated the light from the scintillator, an LED (λ = 665 nm) was used and pulse generator 1 controlled it by sending randomly distributed pulses during the integration period (charge storing period). During the integration period (t_0 ~ t_1), pulse

generator 2 provided a reverse bias to the test pixel, and after the integration time (t_1) the bias was set to zero for discharging (readout) of the stored charge. When a step pulse of the reverse bias, $-V_a$, is applied to the pixel, the p-i-n photodiode acts like a capacitor and charge builds up on its surface as well as on the storage capacitor due to the displacement current. The RC time constant of this charge-build-up on the storage capacitor is equal to the product of the total capacitance of the test pixel and a series resistance of the pixel which is mainly the contact resistance. The amount of the displacement charge is $V_a C_d C_i/(C_d+C_i)$, where C_d and C_i is the capacitance of the p-i-n photodiode and the storage capacitor, respectively. During readout, this displacement charge will also be discharged together with the signal charge. Hence, to select the signal charge only, the external capacitor C_c and R_c were used, where C_c was equal to the total capacitance of the test pixel and R_c was equal to the contact resistance of the test pixel ($\sim 100k\Omega$). Pulse generator 3 provides R_c-C_c components with a pulse of the same magnitude (V_a) as the pulse from pulse generator 2 but with opposite polarity (+). By applying this pulse on the R_c-C_c components synchronously with the sequence of the detector biasing pulse from pulse generator 2, the displacement charge can be separated from the signal charge. In the experiments, 98% of the displacement charge could be canceled by this method. The stored signal charge and thermally generated background charge was discharged by switching the applied bias to 0 V. The discharging current was read by the digital oscilloscope and the amount of the stored charge was obtained by integration of the current in the computer. The test pixel was contained in a heat insulated container and the operating temperature was controlled by dry ice.
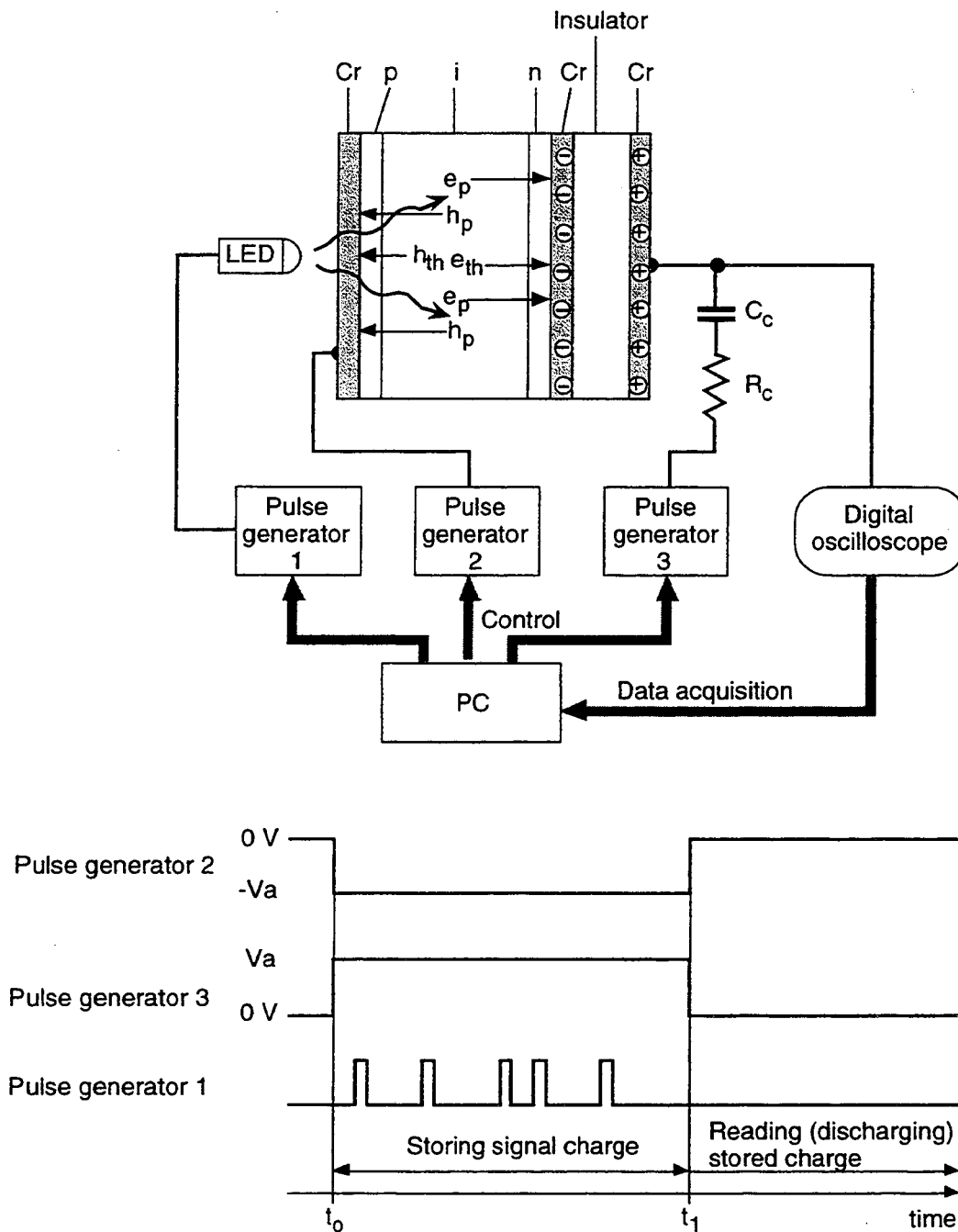
Fig. 4-9   Schematic diagram of the experimental system. A PC was used to control the pulse generators and also for data acquisition. Pulse generator 1 controls the LED light during the integration period (storing period). Pulse generator 2 and 3 provided biases for the detector system. The time sequence of the pulses are shown at the bottom. See text for details.

4.4   Results from Experiments

4.4.1   Temperature Effect on Thermal Generation Current

When a reverse bias, V_a, is initially applied on the pixel, the initial voltage across the p-i-n photodiode, V_d, and the storage capacitor, V_i, is

$$V_d = \frac{C_i}{C_i + C_d} V_a$$

$$V_i = \frac{C_d}{C_i + C_d} V_a \quad .$$

Due to the reverse bias V_d, thermally generated charge flows along the electric field and is accumulated on the storage capacitor. As this background charge builds up on the capacitor the voltage across the capacitor will increase and the voltage across the photodiode will decrease, correspondingly. Hence, the thermal generation current will flow until the capacitor is saturated with the charge Q_{sat} $(= V_a C_i^2/(C_d+C_i))$, so that the voltage across it is equal to V_a. The time taken to saturate the capacitor with the background charge depends on the thermal generation current. If the thermal generation current is too large, the capacitor will be saturated in a short time and the light induced signal charge cannot be obtained. In order to see the temperature effect on the background charge, measurements were done without light at various temperatures. The thermal generation current and the stored background charge as functions of storage time are shown in Fig. 4-10 and 4-11. At room temperature, the thermal generation current is initially very large, but as the voltage across the photodiode drops quickly the current decreases correspondingly. At
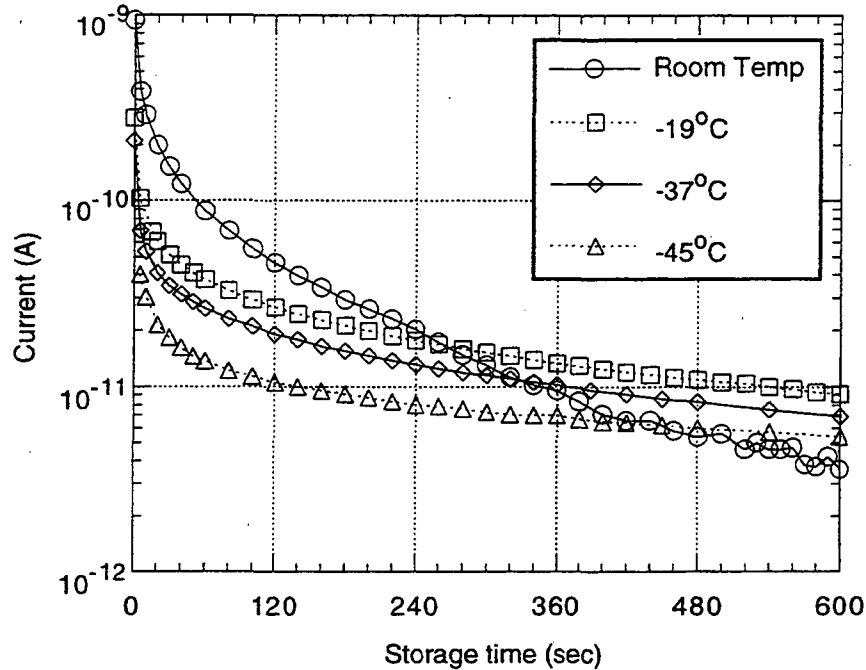
Fig. 4-10   Time dependent thermal generation current after
applying 10 V of reverse bias on the test pixel at
various temperatures.

this temperature, 10 min after applying 10 V of V_a on the test pixel, the
thermally generated charge accumulates almost up to the saturation level
and there is little room for the signal charge. At -45°C, however, as the
thermal generation current is low, the amount of the stored background
charge after 10 min is about 21 % of the saturation level, and it takes as long
as 9 hours to reach the saturation level. Therefore, at -45 °C, about 79 % of
the saturation level can be used to accommodate the light induced signal
charge with a storage time of 10 min.

4.4.2   Signal Charge Measurement

The relationships between the input light amount and collected
charge after 5 min of storage time at two different temperature are shown

106
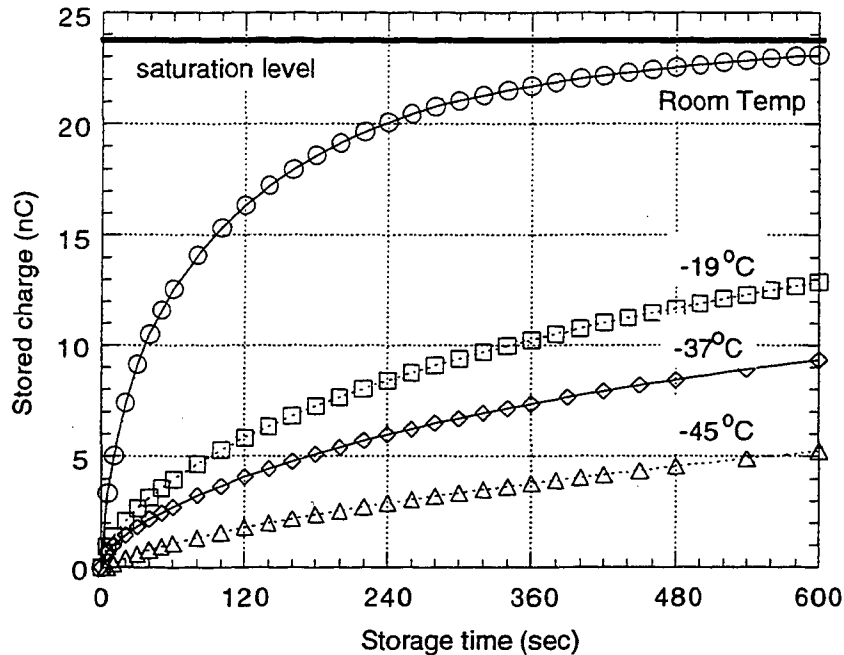
Fig. 4-11   Accumulation of thermally generated background charge on the storage capacitor as a function of storage time. 10 V of reverse bias was applied. The capacitor is almost saturated with background charge with the storage time of 10 min at room temperature.

in Fig.4-12. The signal charge can be obtained by subtracting the background charge from the measured total stored charge. The background charge was measured separately. For 5 min storage time, the stored background charge at room temperature is so large, that the maximum storage of the signal charge is only ~10 % of the saturation level, while ~70% of the saturation level can be used for signal charge storage at -37°C. At low temperature, it is shown that, even with a long storage time of 5 min, there is a linear relationship between the input light amount and the output signal up to about 85% of the saturation level. According to the experimental results, the type B a-Si:H based gamma camera can be operated in integration mode at low temperature.
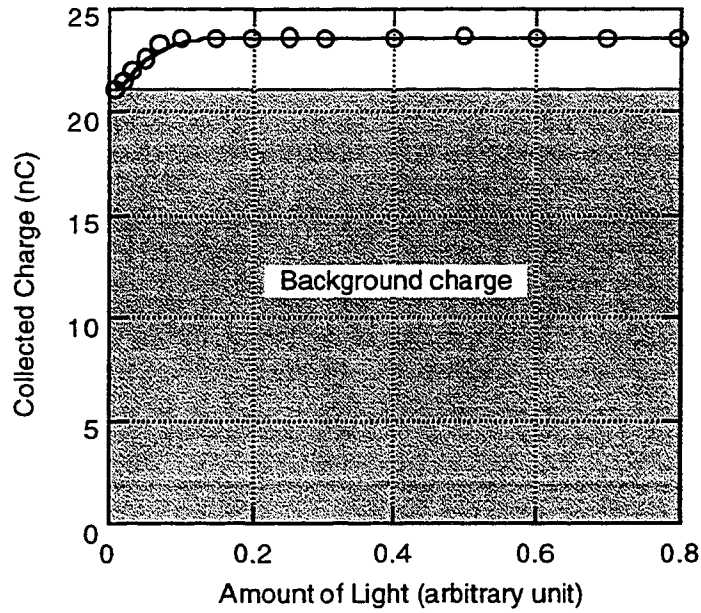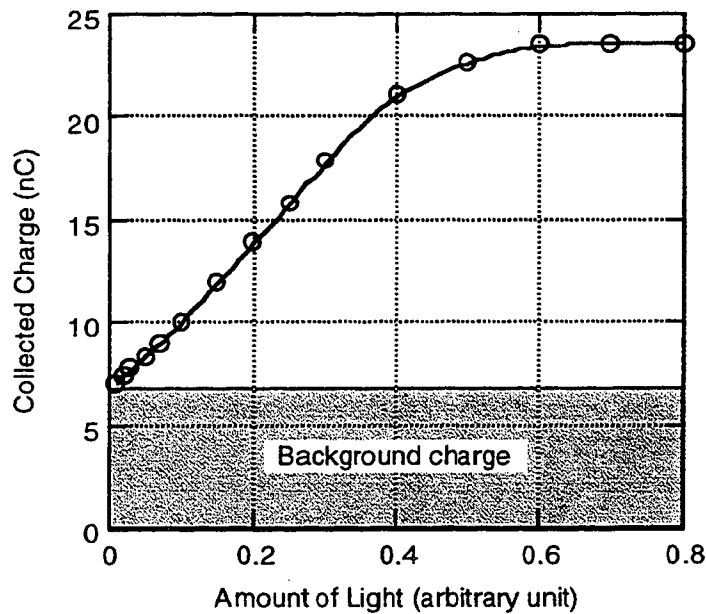
Fig. 4-12   Relationship between the input light amount and the collected signal charge after 5 min of storage time. (a) was measured at room temperature and (b) was measured at -37 °C. 10 V of reverse bias was applied. There is a linear relationship between input and output up to 85% of the saturation level.

The operating temperature can be easily controlled by attaching the camera to a thermoelectric cooling device and shielding with heat insulating materials. The thermoelectric cooling device utilizes the Peltier effect and can reduce the temperature down to about 195 K.[14]

4.5 Analyses

4.5.1 Time-Dependent Thermal Generation Current

Using the thermal generation current model discussed in Section 4.2, the time dependent behavior of the thermal generation current, hence the storage of background charge, of the photodetector pixel in type B a-Si:H based gamma camera can be derived using simple circuit analyses. When a bias V_a is applied on the pixel, the a-Si:H p-i-n photodiode can be considered as a voltage dependent current source after the initial short RC transient (~100 μsec). Then the circuit of the detector components can be drawn as in Fig. 4-13, and using Eq. (4-15) and assuming the voltage drop across the resistor R_o is negligible, a differential equation which describes this circuit can be derived as

$$
\begin{aligned}
\frac{dV_i(t)}{dt} &= \frac{I_{thPF}(t)}{C_i} \\
&= \frac{2I_{tho}}{C_i F_o \gamma^2} \left\{ \left[\gamma \left(\frac{V_a - V_i(t)}{d} + \frac{F_o}{2} \right)^{\frac{1}{2}} - 1 \right] \exp\left[\gamma \left(\frac{V_a - V_i(t)}{d} + \frac{F_o}{2} \right)^{\frac{1}{2}} \right] \right. \\
&\quad \left. - \left[\gamma \left(\frac{V_a - V_i(t)}{d} - \frac{F_o}{2} \right)^{\frac{1}{2}} - 1 \right] \exp\left[\gamma \left(\frac{V_a - V_i(t)}{d} - \frac{F_o}{2} \right)^{\frac{1}{2}} \right] \right\}
\end{aligned} \tag{4-25}
$$
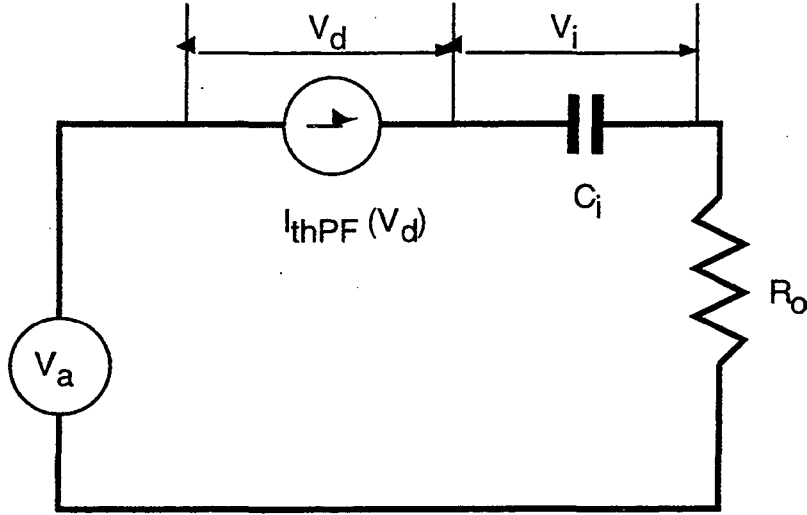
Fig. 4-13   A simplified circuit of the detector components. The a-Si:H p-i-n diode is replaced with a voltage dependent current source $I_{thPF}(V_d)$. The contact resistance of the detector is the main source of the series resistor R_o (~100 kΩ)

But, as this equation cannot be solved analytically, simplification of Eq. (4-15) is needed. We may assume that the electric field is much higher at the p-i interface than at the n-i interface, i.e., $F_M \gg F_m$, and that the lowering of the barrier height ΔE at p-i interface is much higher than the thermal energy kT, i.e., $\gamma\sqrt{F_M} \gg 1$. Then,

$$I_{thPF}(t) \approx \frac{2I_{tho}}{F_o\gamma}\sqrt{F_M(t)}\exp\left(\gamma\sqrt{F_M(t)}\right) .\qquad (4\text{-}26)$$

The thermal generation current equations in Eq. (4-15) and (4-26) are for steady state values. When a reverse bias is applied on a p-i-n diode, the depletion process starts and the initial current is much higher than the steady state value. The decay time of the depletion current is about 200 - 300 sec at room temperature and, because it is thermally activated (with an activation energy of ~E_i,[3]), longer at lower temperature. Now, as we are trying to develop the time dependent behavior, we must also consider this

110

effect by multiplying Eq. (4-26) by a thermal activation correction term, $\exp(\delta/kT)$:

$$I_{thPF}(t) = \frac{2I_{tho}}{F_o\gamma}\exp\left(\frac{\delta}{kT}\right)\sqrt{F_M(t)}\exp\left(\gamma\sqrt{F_M(t)}\right) \ . \tag{4-27}$$

The simplified differential equation using Eq. (4-27) is,

$$\frac{dV_i(t)}{dt} = \alpha\left(\frac{V_a - V_i(t)}{d} + \frac{F_o}{2}\right)^{\frac{1}{2}}\exp\left[\gamma\left(\frac{V_a - V_i(t)}{d} + \frac{F_o}{2}\right)^{\frac{1}{2}}\right] \ , \tag{4-28}$$

where

$$\alpha = \frac{2I_{tho}}{C_iF_o\gamma}\exp\left(\frac{\delta}{kT}\right) \ . \tag{4-29}$$

Solving this equation with the initial condition of $V_i(o) = C_dV_a/(C_i+C_d)$, the electric field as a function of time $F_M(t)$ can be obtained as

$$F_M(t) = \left[\frac{1}{\gamma}\ln\left(\frac{\alpha\gamma}{2d}t + e^{-\gamma\sqrt{F_{Mo}}}\right)\right]^2 \ , \tag{4-30}$$

where

$$F_{Mo} = \frac{C_iV_a}{d(C_i + C_d)} + \frac{F_o}{2} \ . \tag{4-31}$$

Therefore, the time dependent thermal generation current can be obtained by inserting $F_M(t)$ in Eq. (4-30) into (4-27), which produces

$$I_{thPF}(t) = \frac{\alpha C_i}{\gamma}\left|\ln\left(\frac{\alpha\gamma}{2d}t + e^{-\gamma\sqrt{F_{Mo}}}\right)\right|\exp\left[\left|\ln\left(\frac{\alpha\gamma}{2d}t + e^{-\gamma\sqrt{F_{Mo}}}\right)\right|\right] \ , \tag{4-32}$$

and the stored background charge is

$$Q_{th}(t) = C_i[V_i(t) - V_i(0)]$$

$$= C_i \left\{ \frac{C_i V_a}{C_i + C_d} - d \left[F_M(t) - \frac{F_o}{2} \right] \right\} . \qquad (4\text{-}33)$$

By assigning proper value to the correction parameter δ in Eq. (4-29), a good fit of the time-dependent thermal generation current and stored background charge with the measurements were obtained. For the best fit $\delta = 0.5$ eV was given with $E_i = 0.9$ eV and $\beta_{PF} = 0.038$ eV$/\sqrt{V/\mu m}$. The calculated thermal generation currents and stored background charge are compared with those obtained from the measurements in Fig. 4-14, which shows an excellent agreement between the measurements and the theoretical model of the thermal generation current.

4.5.2 Estimation of the Maximum Storage Time

Using the time-dependent current model described in the previous subsection, the operating parameters of the photodetector pixels with any geometry can be estimated. For example, the storage time t_s at which the accumulated background charge is κ % of the saturation level is expressed as

$$t_s = \frac{2d}{\alpha \gamma} \left\{ \exp\left[-\gamma \left(\frac{F_o}{2} + \frac{C_i V_a}{d(C_i + C_d)} (1 - \kappa/100) \right)^{1/2} \right] - e^{-\gamma \sqrt{F_{Mo}}} \right\} . \quad (4\text{-}34)$$

Defining the maximum storage time of the pixels t_M as the time taken to accumulate the background charge up to 10% of the saturation level of the storage capacitor, the effects of temperature, applied bias and detector thickness on the maximum storage time are shown in Fig. 4-15 (a) and (b).

112
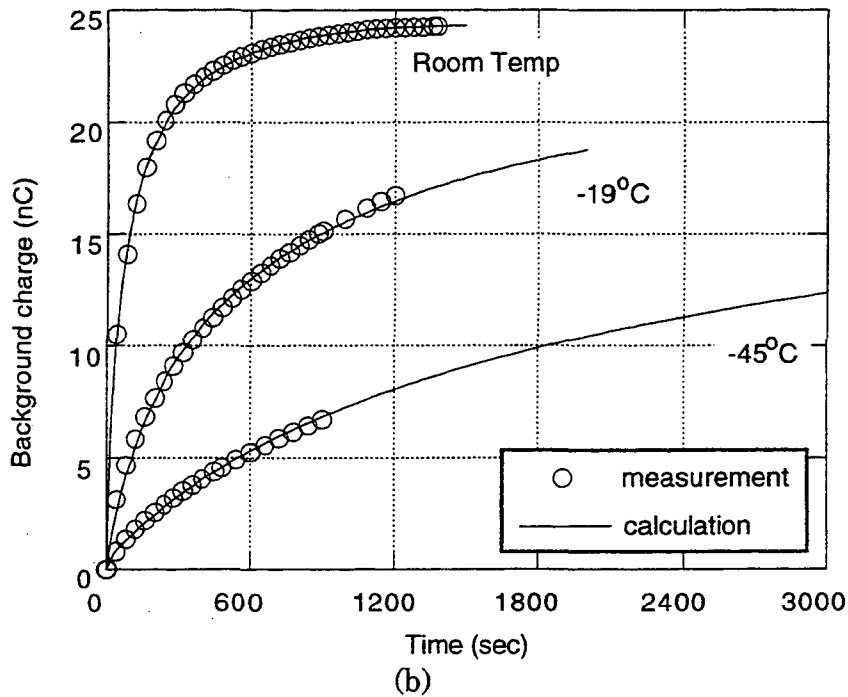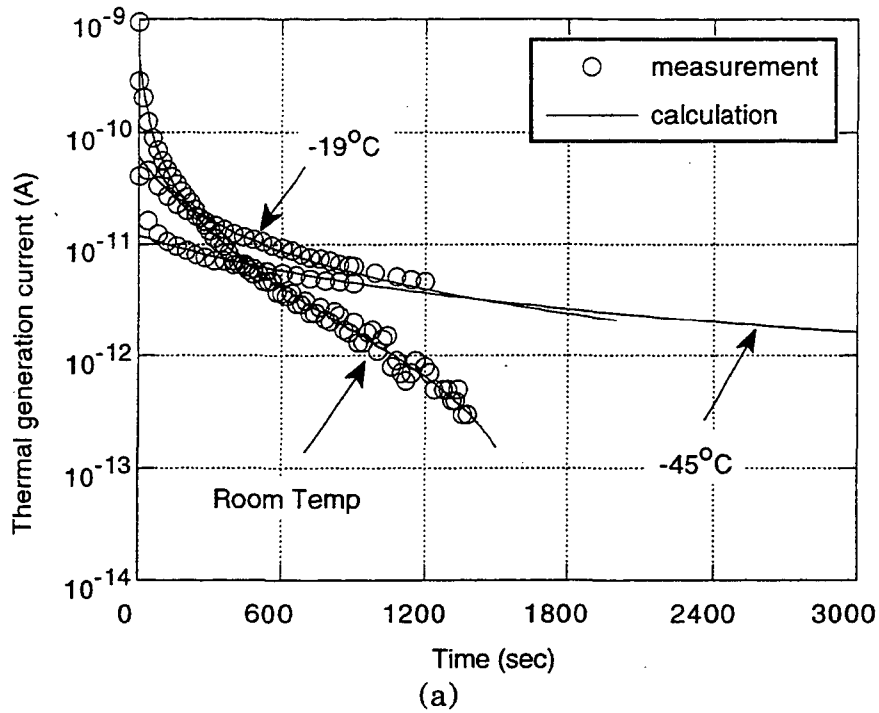
Fig. 4-14 Comparisons of measurements and theoretical calculations for (a) the time-dependent thermal generation current and (b) the stored background charge at various temperatures. The thickness of the p-i-n diode is 1 μm and the operating bias V_a is 10 V.

(a)

(b)
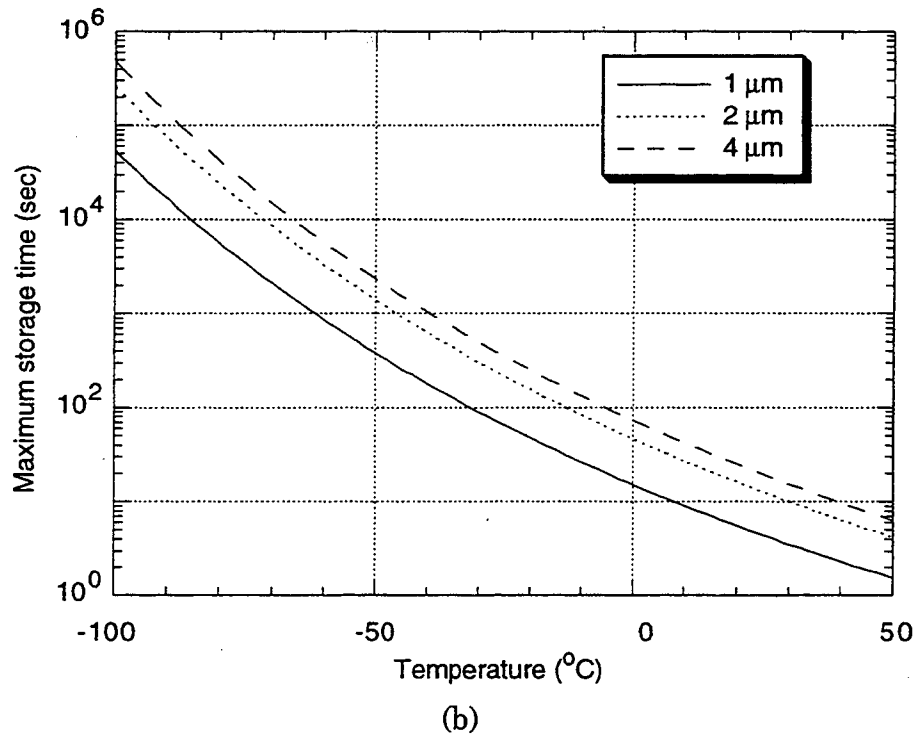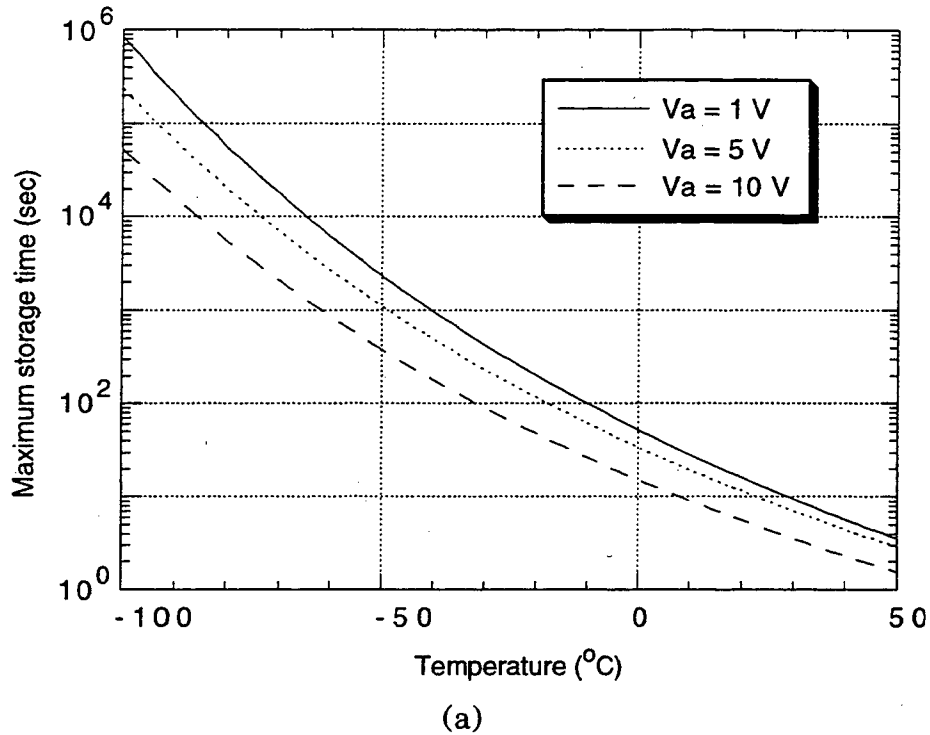
FIG. 4-15 The maximum storage time t_M as a function of temperature with (a) various operating biases with 1 μm thick diode and (b) various p-i-n diode thicknesses with 10 V of operating bias. t_M was defined as the time taken to accumulate the background charge up to 10 % of the saturation level.

114

In both graphs, the dependence of the t_M on the temperature is significant, hence the maximum storage time can be manipulated simply by controlling the temperature. It is shown in Fig. 4-15 (a) that for the same thickness of the a-Si:H p-i-n photodiode, a lower operating voltage produces longer storage time, but it has to be sufficient to fully deplete the i-region, otherwise the photo-induced signal charge cannot be collected with full efficiency. In Fig. 4-15 (b), the effect of the thickness of a-Si:H p-i-n diode on the storage time is shown and thicker diode is better at the same operating bias, which is the same trend as in Fig. 4-15 (a). Using these graphs the required operating temperature for a predetermined storage time can be estimated. For a storage time of 5 min with a detector thickness of 1 µm, for example, the temperature required to suppress the background charge down to 10 % of the saturation level is -26 °C with $V_a = 1$ V and -47 °C with $V_a = 10$ V.

4.6   Discussion

A study of an a-Si:H photodetector which is able to store the light induced charge for a long time was described. This detector is composed of a normal a-Si:H p-i-n photodiode and a storage capacitor in series. In pixel type, this detector can be used as the imaging array in type B a-Si:H based gamma camera which is proposed in Chapter 3.

The effect of temperature on the thermally generated background charge was tested using test pixels. According to the experimental results, this detector is not adequate to operate at room temperature because for 5 min of storage time, for example, the background charge is already ~90%

of the saturation level of the storage capacitor, hence the signal charge cannot be stored efficiently. But at lower temperatures, this detector works well, with a much lower amount of background charge. At -45°C with a storage time of 5 min, about 85% of the saturation level could be used to store the signal charge. By subtracting the background charge which was measured separately without light source, the signal charge could be measured easily even with a storage time of longer than 5 min at low temperatures, and this signal charge was linearly proportional to the input light amount up to about 85% of the saturation level, which indicates that there was no loss or distortion of the signal during the storage time.

The thermal generation current which produces nearly all of the background charge in this type of storing photodetector was extensively analyzed. The Poole-Frenkel effect was found to be the most significant source of the thermal generation, and both the steady state and time-dependent current were modeled based on the Poole-Frenkel thermal emission process. The current model gave an excellent fit to the measurements and, using this model, the operating conditions of the photodetector can be estimated. For a long storage time and low background charge, a thick device with a low operating voltage at low temperature is preferred, subject to the constraint that the voltage is high enough to fully deplete the i-region. For a storage time of 5 min, an operating temperature of -26 °C was estimated with a 1 μm thick a-Si:H p-i-n diode and operating bias of 1 V.

References

[1]   R. A. Street, "Long-Time Transient Conduction in a-Si:H p-i-n Devices," Philos. Mag. B, 63, 1343 (1991)

[2]   S. M. Sze, *Physics of Semiconductor Devices*, 2nd Ed., John Wiley & Sons, New York (1981)

[3]   R. A. Street, "Thermal Generation Currents in Hydrogenated Amorphous Silicon p-i-n Structures," Appl. Phys. Lett., 57, P.1334 (1990)

[4]   D. V. Lang, J. D. Cohen and J. P. Harbison, "Measurement of the Density of Gap States in Hydrogenated Amorphous Silicon by Space Charge Spectroscopy," Phys. Rev. B, 25, 5285 (1982)

[5]   J. D. Cohen and D. V. Lang, "Calculation of the Dynamic Response of Schottky Barriers with a Continuous Distribution of Gap States," Phys. Rev. B, 25, 5321 (1982)

[6]   G. Vincent, A. Chantre and D. Bois, "Electric Field Effect on the Thermal Emission of Traps in Semiconductor Junctions," J. Appl. Phys., 50, 5484 (1979)

[7]   E. Rosencher, V. Mosser and G. Vincent, "Transient-Current Study of Field-Assisted Emission from Shallow Levels in Silicon," Phys. Rev. B., 29, 1135 (1984)

[8]   R. M. Hill, "Poole-Frenkel Conduction in Amorphous Solids," Philos. Mag., 23, 59 (1971)

[9]   J. L. Hartke, "The Three-Dimensional Poole-Frenkel Effect," J. Appl. Phys., 39, 4871 (1968)

[10]   J. G. Simmons, "Generalized Formula for the Electric Tunnel Effect between Similar Electrodes Separated by a Thin Insulating Film," J. Appl. Phys., 34, 1793 (1963)

[11] S. Chaudhuri, D. D. Coon and G. E. Derkits, "Rate of Field Ionization from S States with a Quantum Defect," Phys. Rev. A, 23, 1657 (1981)

[12] E. N. Korol, "Ionization of Impurity States in Semiconductors by an Electric Field," Sov. Phys. Solid State, 19, 1327 (1977)

[13] R. A. Street, *Hydrogenated Amorphous Silicon*, Cambridge University Press, Cambridge, (1991)

[14] C. Kittel and H. Kroemer, *Thermal Physics*, 2nd Ed., W. H. Freeman and Co., San Francisco (1980)

Chapter 5   Photoconductive Gain

5.1   Introduction

Using a-Si:H p-i-n photodiodes, many applications in the detection of visible light, x-rays, γ-rays, charged particles and neutrons have been investigated since the first experimental success of detecting x-rays using a-Si:H.[1-6]   The basic principle involved in these previously reported radiation detection techniques is to measure the signal which is induced by motion of the charge carriers along the depletion field in the reverse biased p-i-n diode as discussed in Chapter 2.   The maximum number of charge carriers collected in a reverse biased p-i-n diode is equal to the number of photons which had interactions in the i-region of the diode, hence the maximum gain, which is defined as the ratio of the collected charge to the number of interacted photons, is unity.

The photoconductive gain mechanism in a-Si:H, which is primarily due to hole trapping and subsequent charge neutralization,[7-9] has been investigated with various structures such as metal-i-metal, n-i-n, p-i-n and n-i-p-i-n, and photoconductive gains of more than 100 for the steady state photocurrent were reported.[7,10-13]   Optical imaging devices utilizing this gain mechanism, which were based on Schottky diodes or n-i-n devices with coplanar or sandwich structures have been successfully made from a-Si:H.[14-20]

For radiation detection using a-Si:H, CsI(Tl) is usually coupled to a-Si:H devices to convert the radiation to visible light, and the fluorescence

decay time of CsI(Tl) is about 1 μsec.[21] Hence, the duration of light exposure is about 1 μsec for a fast transit charged particle or a γ-ray, and a few milliseconds for an x-ray exposure in medical imaging. For normal a-Si:H, it takes hundreds of microseconds or even a few milliseconds to achieve steady state photoconductive gain.[11,15] Therefore during the short period of light exposure from CsI(Tl) in radiation detection using a-Si:H devices, the full photoconductive gain may not be achieved. The transient photoconductive gain during a short period light exposure is not completely understood yet, but if a moderate gain can be obtained during a rather short period, this photoconductive gain mechanism may be applied to radiation detection such as a single charged particle or γ-ray detection and x-ray imaging.

In this chapter, the experimental results of the gain with a-Si:H p-i-n, n-i-n and n-i-p-i-n devices for rather short period of light pulses are discussed.

5.2   Principles

5.2.1 Primary Photocurrent and Secondary Photocurrent

There are two types of photosensitive devices made of insulating or semiconducting materials: photoconductors and photodiodes.[19] The typical structures of a photodiode and a photoconductor are schematically shown in Fig. 5-1 (a) and (b). Usually, photodiodes have a sandwich structure, and photoconductors have gap geometry with coplanar
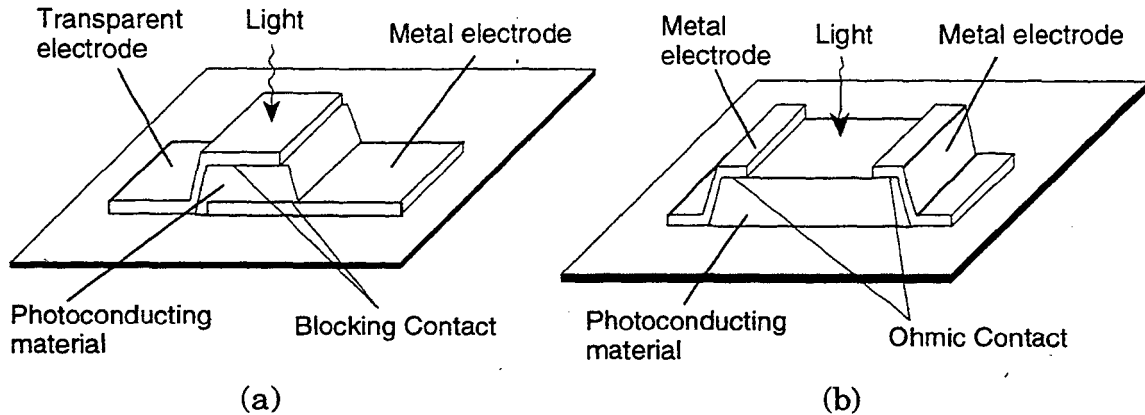
Fig. 5-1   Typical structures of (a) photodiode and (b) photoconductor. The contacts in a photodiode are blocking in reverse bias while those in a photo-conductor are ohmic.

electrodes as shown in the figure, but, sometimes, sandwich structured photoconductors are also made.[11,20,22] The basic difference in these two devices is the type of the contacts. The contacts in photoconductors are ohmic, while photodiodes have blocking contacts when they are reverse biased. Due to this difference in the contacts, both the dark current and the photocurrent behaviors in photoconductors and reverse biased photodiodes are quite different.

A blocking contact prevents injection of charge carriers through it, hence the dark current in a reverse biased photodiode is mainly due to the thermal generation current in the bulk of the device, and the maximum photocurrent is simply limited by the optical generation rate therefore the gain is limited to unity. The photocurrent in reverse biased photodiodes is termed primary photocurrent.[7,19,24] The flow of charge carriers in a reverse biased photodiode is shown in Fig. 5-2 (a). a-Si:H p-i-n devices are photodiodes since in reverse bias the n- and p- layer prevents injection of holes and electrons, respectively. The maximum photocurrent density of a
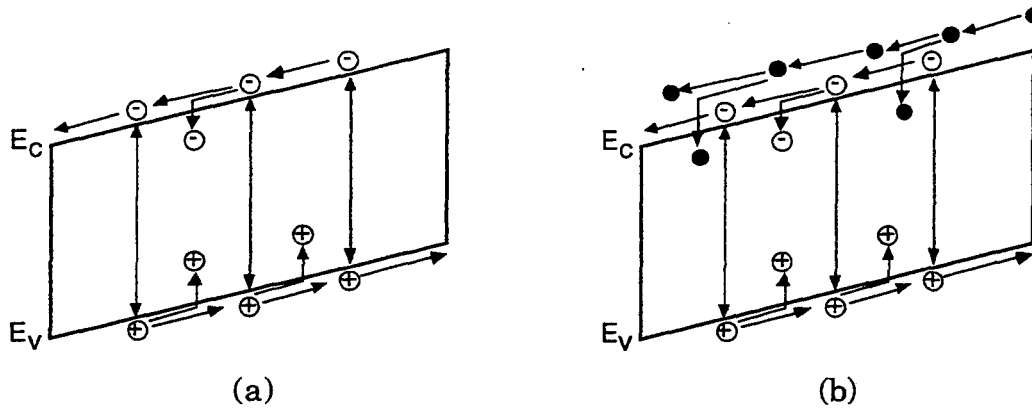
Fig. 5-2   Schematic representation of photo-generated charge carrier flow
in (a) reverse biased photodiode and (b) photoconductor. Circles
with a minus represent photo-induced electrons and circles with
a plus represent photo-induced holes. Solid circles in a
photoconductor represent injected electrons from the cathode.
Note that in a photodiode free carriers are generated only by
photon interactions, while in a photoconductor injection of
carriers (electrons in this case) enhances the photocurrent.

reverse biased photodiode which is exposed to a uniform light which

generates F electron-hole pairs per second per unit volume is

$$J_{pri} = qFd \quad .$$
(5-1)

where q is the charge of an electron and d is the thickness of the diode. In

Eq. (5-1) the recombination of the charge carriers during their transit was

neglected, that is, a full collection efficiency was assumed, which is a

satisfying assumption when the reverse bias is sufficiently high such that

the mean free path of the minority carriers is longer than the diode

thickness and both the majority and minority charge carrier densities are

low.   The photoresponse speed of a-Si:H photodiodes is fast (less than

10 nsec) compared to that of photoconductors,[19] but the signal is small,

hence they are suitable for high speed large signal measurements.

122

In photoconductors or forward biased photodiodes, the contacts are ohmic, hence injection current flows when a bias is applied. Due to this injection current, the dark current in forward biased photodiodes or photoconductors is much higher than the corresponding reverse biased photodiodes. The ohmic contacts can always supply the current required by the photoconductor and this mode of photocurrent is referred to as a secondary photocurrent.[7,19,24] In this case, whenever a charge carrier which is induced by a photon reaches an electrode, it is replenished at the other electrode. Therefore the photocurrent keeps flowing until all the photo-induced carriers disappear by recombination. Various cases of secondary photocurrents are well described in Reference 24. The transport mechanism of the secondary photocurrent is schematically shown in Fig. 5-2 (b), in which single carrier (electron) injection is assumed. Usually, photoconductors or forward biased photodiodes have a high photo-signal but slow photoresponse and high dark current, therefore their usage is limited to low event rate or steady state measurements of small signals. Derivations of the secondary photocurrent and the photoconductive gain in photoconductors are as follows. Consider a photoconductor which is made of an insulator or a semiconductor with a single trap level and a single recombination level. Assuming electrons are the majority carriers and the contribution of hole photoconductivity is negligible, the continuity equations of electrons are

$$\frac{dn_f}{dt} = F + \frac{n_t}{\tau_{rel}} - \frac{n_f}{\tau_{tr}} - \frac{n_f}{\tau_l}$$

$$\frac{dn_t}{dt} = \frac{n_f}{\tau_{tr}} - \frac{n_t}{\tau_{rel}} \qquad ,$$

(5-2)

where n_f and n_t are the free and trapped electron density, respectively, F is the optical generation rate which is assumed constant, τ_{rel} is the thermal excitation time of trapped electrons, τ_{tr} is the trapping time of free electrons in the conduction band and τ_l is the recombination lifetime of free electrons. n_f/τ_{tr} corresponds to the trapping rate of free electrons by the single trap level, and n_t/τ_{rel} is the thermal release rate of the trapped electrons from the trap. In Eq. (5-2), free and trapped electron densities are assumed to be spatially uniform, and the thermal generation rate from the recombination centers is neglected because the number of electrons in the conduction band is mostly determined by the injected electrons rather than the thermally generated electrons. If we assume that $\tau_{tr} << \tau_{rel}$ and $\tau_{tr} << \tau_l$, the solution of Eq. (5-2) is

$$n_f(t) = F \left\{ \tau_l \left[1 - \exp\left(-\frac{t}{\tau_{res}} \right) \right] + \tau_{tr} \left[1 - \exp\left(-\frac{t}{\tau_{tr}} \right) \right] \right\} \qquad (5-3)$$

where τ_{res} is the response time of the photoconductor defined as

$$\tau_{res} = \frac{\tau_{rel}}{\tau_{tr}} \tau_l \qquad (5-4)$$

If there are no traps the response time is equal to the recombination lifetime of electrons τ_l. If the time of interest t is much greater than τ_{tr}, Eq. (5-3) is reduced to the well known transient equation[24]

$$n_f(t) = F\tau_l \left[1 - \exp\left(-\frac{t}{\tau_{res}} \right) \right] \qquad (5-5)$$

Using Eq. (5-3), the secondary photocurrent density can be derived as

124

$$J_{sec}(t) = \frac{qn_f(t)d}{t_r}$$

$$= \frac{qFd\tau_l}{t_r} \left\{ 1 - \exp\left(-\frac{t}{\tau_{res}}\right) + \frac{\tau_{tr}}{\tau_l}\left[1 - \exp\left(-\frac{t}{\tau_{tr}}\right)\right]\right\} \quad . \tag{5-6}$$

where t_r is the transit time of a free electron from one contact to another. By dividing the secondary photocurrent in Eq. (5-6) by the maximum primary photocurrent in Eq. (5-1), the photoconductive gain is expressed as

$$G(t) = G_{ss}\left\{ 1 - \exp\left(-\frac{t}{\tau_{res}}\right) + \frac{\tau_{tr}}{\tau_l}\left[1 - \exp\left(-\frac{t}{\tau_{tr}}\right)\right]\right\} \tag{5-7}$$

where $G_{ss} = \tau_l/t_r$ is the well known steady state photoconductive gain which was originally derived by Rose.[23,24] In steady state the ratio of τ_{rel} to τ_{tr} is equal to n_t/n_f, hence the response time in Eq. (5-4) can be expressed as

$$\tau_{res} = \frac{n_t}{n_f}\tau_l \tag{5-8}$$

which is in agreement with Rose's definition of response time.[23]

5.2.2 Photocurrent in a-Si:H Photoconductors

Since a-Si:H has a distribution of trap levels in the forbidden gap, simple expressions of the continuity equations as in Eq. (5-2) are not adequate. Assuming K levels of traps in the forbidden gap, the continuity equations for a-Si:H photoconductors are[25,28,29]

$$\frac{dn_f}{dt} = F + \sum_i^K \left(\frac{n_{t,i}}{\tau_{rel,i}} \right) - n_f \sum_i^K \left(\frac{1}{\tau_{tr,i}} \right) - \frac{n_f}{\tau_l}$$

$$\frac{dn_{t,i}}{dt} = \frac{n_f}{\tau_{tr,i}} - \frac{n_t}{\tau_{rel,i}}, \qquad i = 1, 2, \dots K$$

(5-9)

Of course it is not possible to solve these $K+1$ set of differential equations analytically, but from the current expression in Eq. (5-6), we can expect that the rise of the photocurrent in a-Si:H photoconductors may be expressed with multicomponent exponentials.[25-27] The expected photocurrent density equation in a-Si:H photoconductors is

$$J_p(t) = J_{ss}\left(1 - \sum_i a_i e^{-t/\tau_i} \right)$$

(5-10)

where $J_{ss} = J_{pri}G_{ss}$ is the photocurrent density at steady state, τ_i is a response time which corresponds to the i-th trap and a_i is a weighting factor which represents the influence of the i-th trap to the photocurrent. The summation of a_i is equal to 1. It is not easy to extract physically meaningful information from a_i due to the complexity of the differential equations, but we may conjecture that based on the expression in Eq. (5-6) a_i may be related to the trapping time to the i-th trap. By the same procedure, the decay of the photocurrent density after shutting off the light can be expressed as

$$J_p(t) = J_o \sum_i a_i e^{-t/\tau_i}$$

(5-11)

where J_o is the photocurrent density at the moment the light is shut off. The measured photocurrent shape in a forward biased a-Si:H p-i-n diode

with a 1 msec light pulse is shown in Fig. 5-3 with the curves fitted by Eq. (5-10) and (5-11), where a_i and τ_i were used as fitting parameters.

A more complete derivation of the transient photocurrent equation from Eq. (5-9) was performed by Schmidlin using Laplace transforms,[25] but still it is hard to correlate the resulting photocurrent equation with physical concepts. For a continuous distribution of traps in the forbidden gap, the photocurrent decay can also be described by a power of time.[25] Using a multiple trapping model and Fourier integral theorem, Pandya and Schiff numerically calculated the decay of photocurrents in photoconductors with an exponential distribution of traps as in a-Si:H, and both the power law and exponential behavior of the photocurrent decay were found.[28] The power law dependence of the photocurrent decay on time in
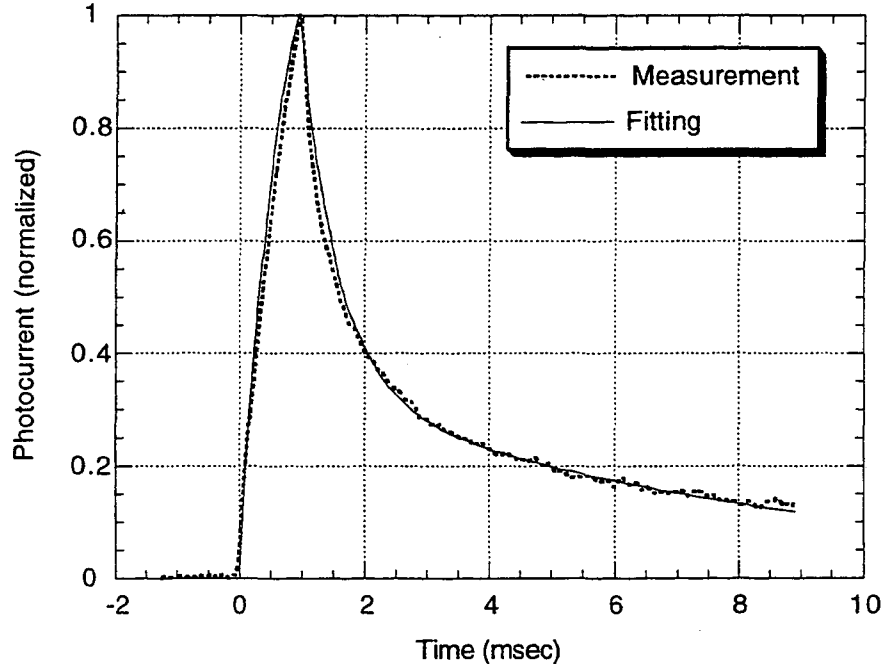
Fig. 3   Photocurrent shape in a forward biased a-Si:H p-i-n diode with a 1 msec light pulse. The current is normalized to the maximum current at 1 msec. 3 V of forward bias was applied. Eq. (5-10) and (5-11) were used to fit the measurement.

a-Si:H photoconductors was also found by others.[15,17]

When a low bias is applied to a photoconductor the transit time t_r of an electron in the a-Si:H photoconductor is determined by Ohm's law and is given by

$$t_r = \frac{d^2}{V\mu_e} \quad ,$$

(5-12)

where V is the applied bias and μ_e is the microscopic mobility of free electrons in the conduction band, which is about 10 cm^2/Vsec in intrinsic a-Si:H. Therefore, the steady state photocurrent density in a-Si:H photoconductors is linearly proportional to the applied bias at low voltage and can be expressed as

$$J_{ss} = \frac{qF\mu_e\tau_l V}{d}$$

(5-13)

The $\mu\tau$ expression in Eq. (5-13) is different from the $\mu\tau$'s obtained from the time-of-flight measurements. $\mu\tau$ values are generally measured by the time-of-flight charge collection measurement, which is discussed in Chapter 2, or the steady state photoconductivity measurement. The $\mu\tau$ value obtained from the steady state photoconductivity measurement is a product of the microscopic mobility and the recombination lifetime and is about two orders of magnitude greater than the $\mu\tau$ value obtained from the TOF measurement, which is a product of the drift mobility and the deep trapping time.[30-33]

When a sufficiently high bias is applied to an a-Si:H photoconductor like an n-i-n device such that the number of injected electrons is greater than that of the photo-induced electrons, the transit time t_r of an electron is

equal to the dielectric relaxation time of the photoconductor due to the space charge effect.[23,24] In this case the steady state photocurrent is no longer linearly proportional to the applied bias, but rather sensitive to the dark current since the dielectric relaxation time t_Ω is dependent on the dark current as

$$t_\Omega = \frac{\varepsilon_{Si}}{q n_f \mu_e} \propto \left(\frac{d}{J_d} \right)^{\frac{l}{l+1}}, \quad \text{with} \quad l = \frac{T_t}{T} \qquad (5\text{-}14)$$

where ε_{Si} is the dielectric constant of a-Si:H, T_t represents the characteristic temperature of the exponential distribution of traps and J_d is the space charge limited dark current density which is given by[34-37]

$$J_d = C \frac{V^{(l+1)}}{d^{(2l+1)}} \qquad (5\text{-}15)$$

where C is a constant which depends on the material properties.

5.3   Experimental

The photoconductive gain in a-Si:H devices was measured on two time scales: one for a short pulse of visible light ($< 1\ \mu sec$) which simulates the transit of an energetic charged particle, and the other for a rather long pulse of light (1 msec) which simulates x-ray exposure in medical imaging. Two definitions of photoconductive gain were used: current gain and charge gain which is an integration of the current gain.

5.3.1 Devices

Various device types such as p-i-n, n-i-n and n-i-p-i-n structures were fabricated and tested. Test samples were fabricated using our PECVD machine and all of the samples had sandwich structure. The thicknesses of the i-layers were 1 ~ 30 μm for p-i-n diodes, 14 μm for n-i-n devices and 1 μm for the thick i-layer of n-i-p-i-n diodes. The thin i-layer in the n-i-p-i-n diodes was about 30 nm thick, and the p-layer was about 15 nm thick and slightly doped with boron (500 ppm of diborane) to suppress the dark current without affecting the photoconductive gain mechanism by recombination of electrons in the p-layer.[11] The n- and p- layers of the p-i-n diodes were thick enough to prevent tunneling of electrons or holes in reverse biased condition, but thin enough to let the light pass through those. These layers provided ohmic contacts in forward bias which is essential for the photoconductive gain as discussed in Section 5.2.1.

5.3.2 Experimental System

The measurements of the photo-signal were performed on two different time scales. In order to simulate the transit of a fast charged particle, an LED of 0.2 μsec pulse width was used, and for the simulation of x-ray exposure, 1 ~ 30 msec of LED light was incident on the samples.

The conventional experimental system for detecting single particles was used for the short pulse measurement, and is shown in Fig. 5-4 (a). As the signal is processed through the charge sensitive preamplifier and the shaping amplifier, the signal amplitude displayed on the oscilloscope is
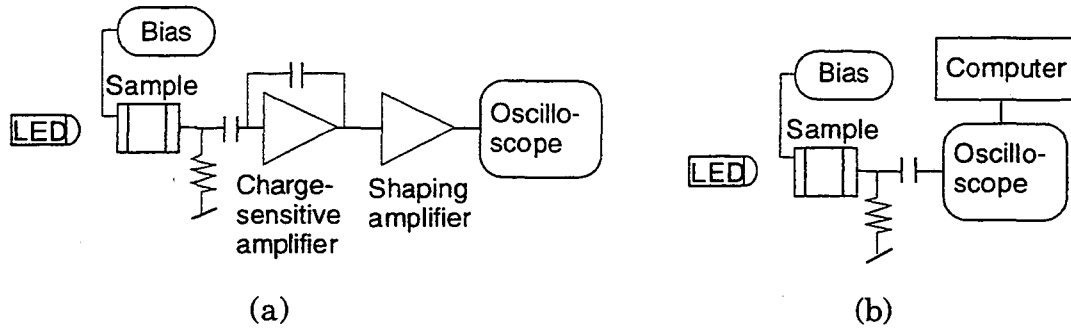
Fig. 5-4   Experimental systems for photoconductive gain measurements.   A conventional radiation measurement system (a) was used for short light pulse measurements, and with a long light pulse the photocurrent was directly read by an oscilloscope via AC coupling (b).

approximately proportional to the charge which is an integration of the photocurrent during the shaping amplifier integration time. Therefore the gain obtained in the short pulse measurements is a charge gain. The gain of a p-i-n or n-i-p-i-n diode was calculated by dividing the photo-signal in forward bias by the maximum signal in reverse bias, which was also used to calculate the gain in an n-i-n device which had the same thickness and transparency as the corresponding p-i-n diode.

For the long pulse measurements, the photocurrents from the sample devices were directly measured as shown in Fig. 5-4 (b). Using AC coupling, the DC dark current could be separated from the photocurrent. The RC time constant of the measuring system was made long enough to prevent decay of the photocurrent level. The data of the measured photocurrent was stored in a computer which is connected to the digital oscilloscope. The measured photocurrent was integrated in the computer, and both the current gain and the charge gain were calculated by comparing the amplitude in forward bias and in reverse bias as in the short pulse measurements.

131

5.4   Results and Analyses

5.4.1   Long Light Pulses

For a 1 msec light pulse, the photocurrent obtained with a 14 μm thick p-i-n diode is shown in Fig. 5-5. The photocurrent is normalized to the maximum value in reverse bias to show the gain. To achieve a unity gain in reverse bias, the detector bias should be higher than the depletion bias which is defined as the required bias for full depletion of the i-region. More than 200 V was needed to obtain the unity gain in reverse bias with this diode, while the unity gain could be easily achieved with about 1.5 V in forward bias. The photocurrent increased almost linearly with the applied
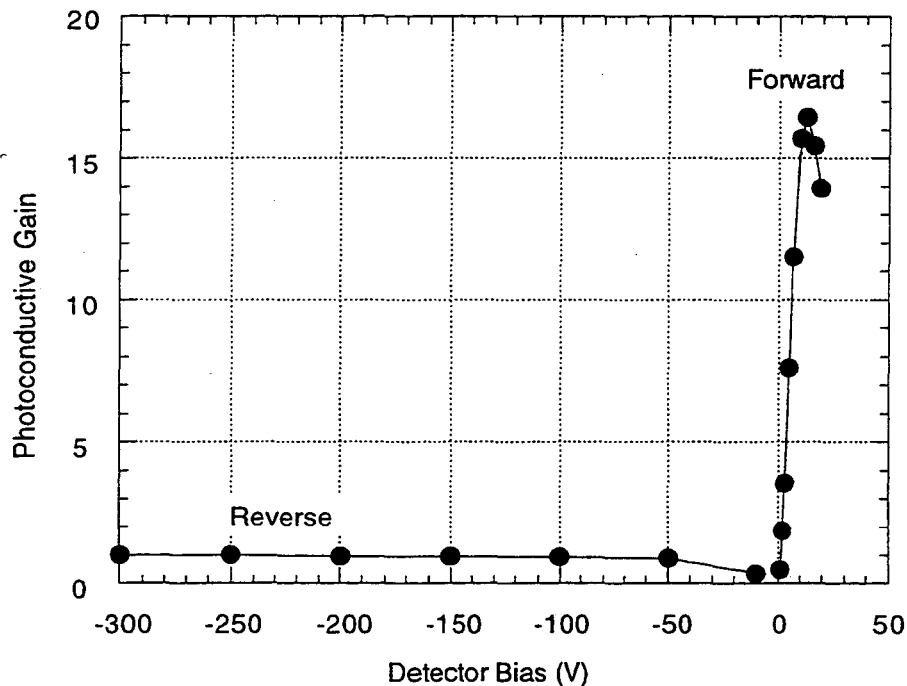
Fig. 5-5   The photocurrent in a 14 μm thick p-i-n diode as a function of detector bias when a 1 msec of light is illuminated. The current is normalized to the maximum value in reverse bias to show gain.

forward bias and reached its maximum value of 17 at 13 V; the gain decreased at higher forward bias as discussed in Section 5.4.3.

For a 1 msec light pulse, the current gain of the same thickness n-i-n device is compared with that of the p-i-n diode in Fig. 5-6 (a) and (b) as a function of detector bias and dark current density, respectively. At low biases the gain in the p-i-n diode is higher than that of the n-i-n device, but at higher biases the gain of the p-i-n diode decrease while that of the n-i-n device keeps increasing and at 100 V the current gain is about 110. While the gain behaviors of the p-i-n and n-i-n devices are quite different when those are plotted as functions of detector bias as in Fig. 5-6 (a), they showed similar dependencies on the dark current at a low current level as shown in Fig. 5-6 (b). The current gain of the n-i-n device was found to be proportional to $J_d{}^{0.6}$, where J_d is the dark current density. From these results, we may say that the photoconductive gain is mainly determined by the dark current rather than the applied bias. This dependence of the photoconductive gain on the dark current level was also expected from Eq. (5-14). At low dark currents, the gains of the p-i-n diode and n-i-n device of the same thickness were almost the same for the same dark current. The dark current densities of the p-i-n and n-i-n devices are plotted in Fig. 5-7 as functions of the detector bias. The dark current in the p-i-n diode is recombination limited as a result of double injection of carriers, and the power law behavior of the dark current on the voltage ($J_d \sim V^3$) was observed as reported by others.[11,38,39] At low voltages, the dark current in the n-i-n device is ohmic, hence it is linearly proportional to the detector bias. At higher voltages (> 15 V), since the n-i-n device is a single carrier

133
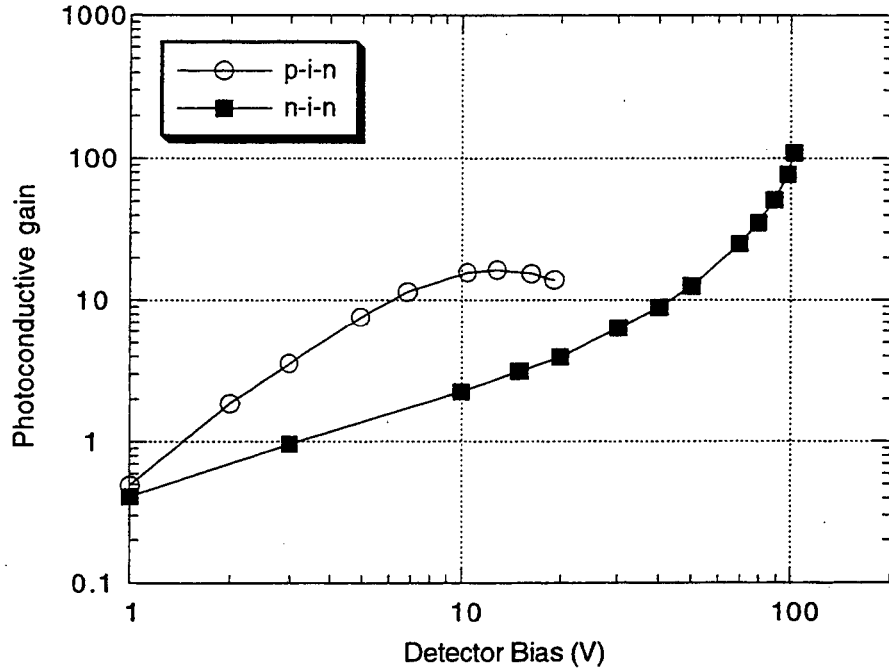
(a)
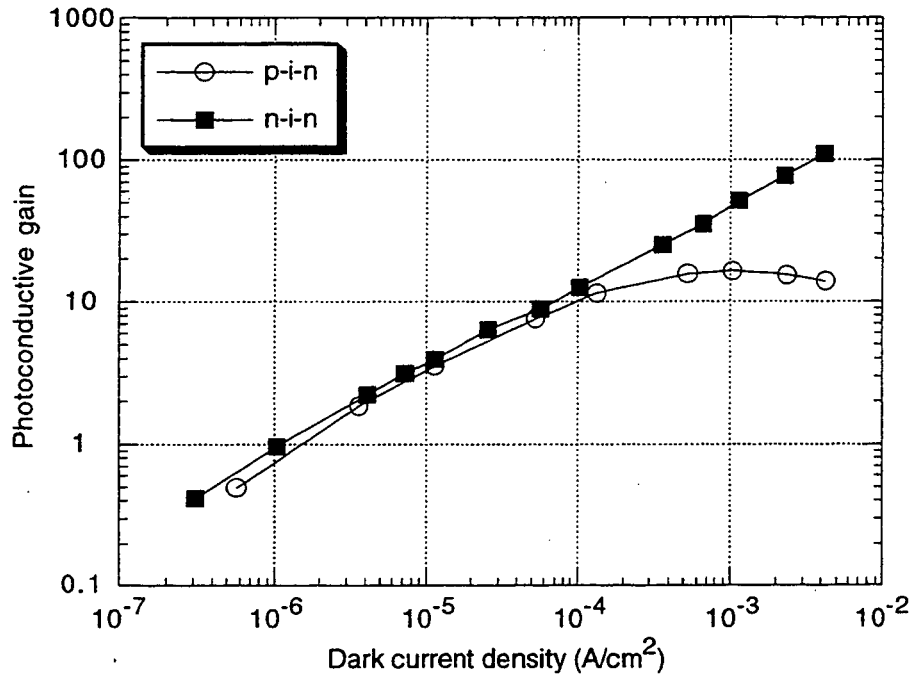
(b)

Fig. 5-6   Comparisons of the photoconductive current gains
in p-i-n diode and n-i-n device. The thickness of the
devices is 14 μm and both devices have the same
transparency. 1 msec of light was exposed.
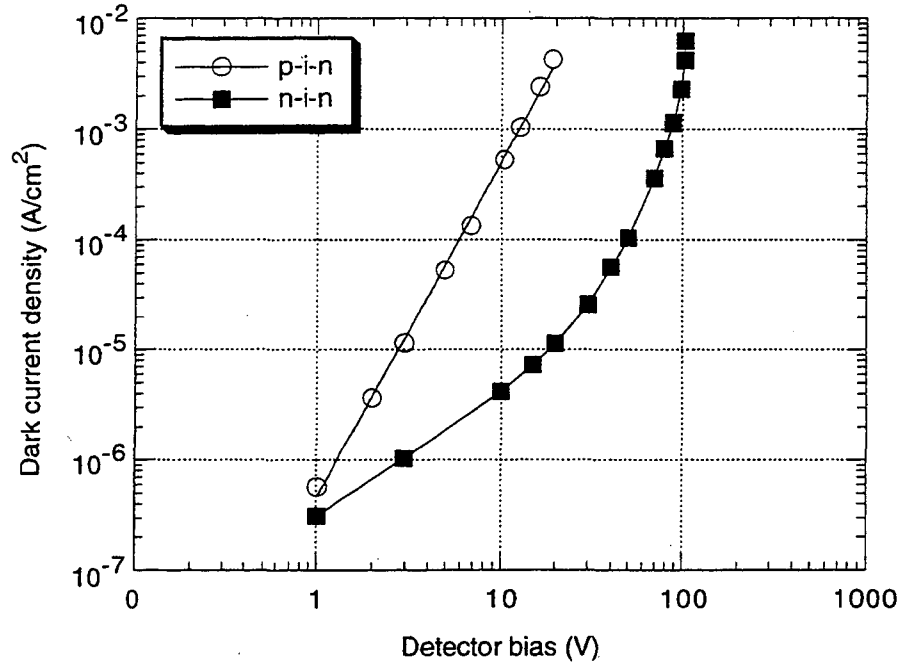
Fig. 5-7   Dependence of the dark current on the applied bias
in forward biased p-i-n diodes and n-i-n devices.

(electron) device, the dark current is space charge limited and follows the expression Eq. (5-15). As the dark current in the n-i-n device is space charge limited it is much lower than that of the same thickness p-i-n diode at a same voltage as shown in Fig. 5-7.[11,38]

The charge gains of a 14 μm thick p-i-n diode and a same thickness n-i-n device for 1 msec light pulse are shown in Fig. 5-8 (a) and (b) as functions of dark current density with various integration times. Due to the long decay time of the photocurrent after shutting of the light, the charge gain is higher for a longer integration time in both p-i-n and n-i-n devices. The behaviors of the charge gain in the p-i-n diode and n-i-n device are very similar to those of the current gain described above. The maximum charge gain in the p-i-n diode for 5 msec of integration time was about 20 at the dark current density of 0.5 mA/cm^2, and for the same integration time a
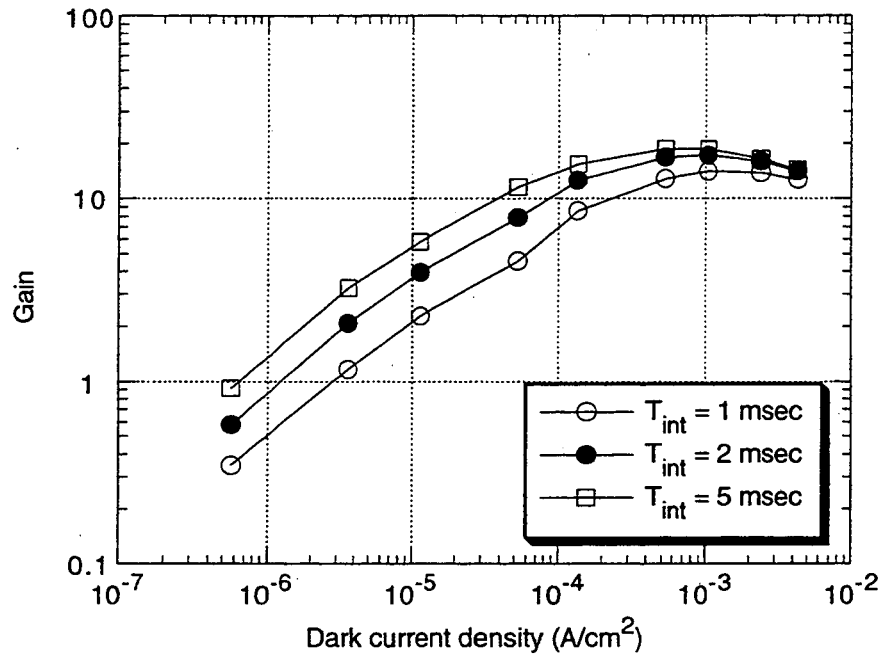
(a)
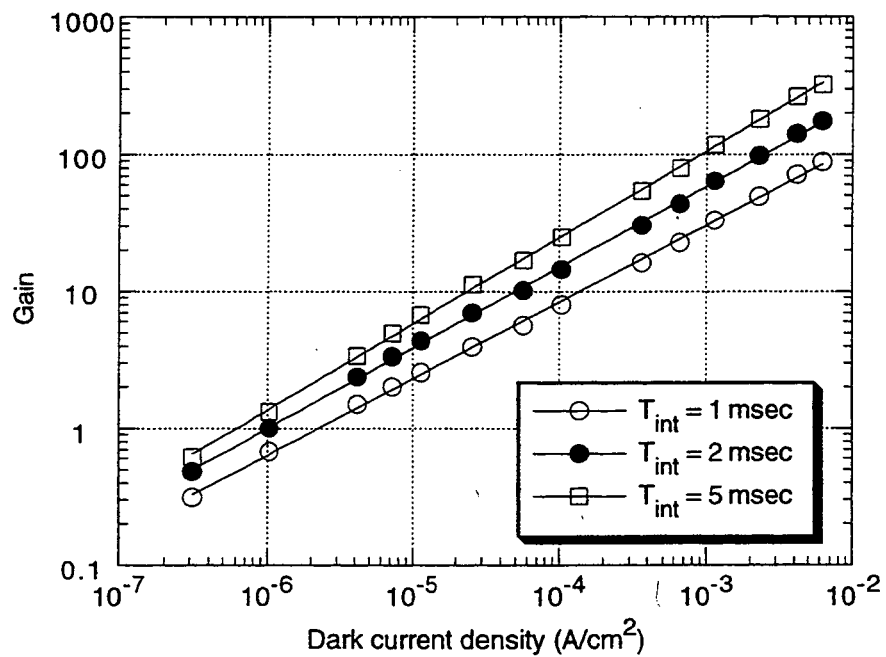
(b)

Fig. 5-8   Charge gains in 14 μm thick p-i-n diode and n-i-n
device as functions of dark current density. Similar
behaviors as in the current gains are seen.

charge gain of 260 could be achieved in the n-i-n device at the dark current density of 6 mA/cm^2. The charge gains in the n-i-n device were proportional to $J_d{}^\alpha$, where $\alpha = 0.56 \sim 0.63$.

The n-i-p-i-n diodes showed similar gain behavior as the n-i-n devices. This is because an n-i-p-i-n diode is basically an n-i-n device with a very slightly doped p-layer which is thin and located close to one end of the device, hence the overall properties are similar to those of the n-i-n device except that it has the polarity of the operation bias, that is, if a negative bias is applied to the thin i-layer side it is in reverse bias. The measured photocurrent in an n-i-p-i-n diode for 10 msec light pulse is shown in Fig. 5-9 (a) as a function of the detector bias in reverse and forward, where the photocurrent is normalized to the maximum value in reverse bias to show the gain. The current gain as a function of dark current density is plotted in Fig. 5-9 (b), and is also proportional to $J_d{}^{0.6}$.

5.4.2 Short Light Pulses

The gains of 14 μm thick p-i-n and n-i-n devices for short light pulse (0.2 μsec) are shown in Fig. 5-10 as functions of dark current density with two different shaping amplifier integration times. As in the case of long light pulses, longer integration time produced larger gains. For short light pulses, the behavior of the p-i-n and n-i-n devices was almost identical to each other for the same dark current, and at a dark current density of 10 mA/cm^2, gains of 3 and 6 are shown in Fig. 5-10 with the integration times of 1 and 5 μsec, respectively. A similar behavior was also found with
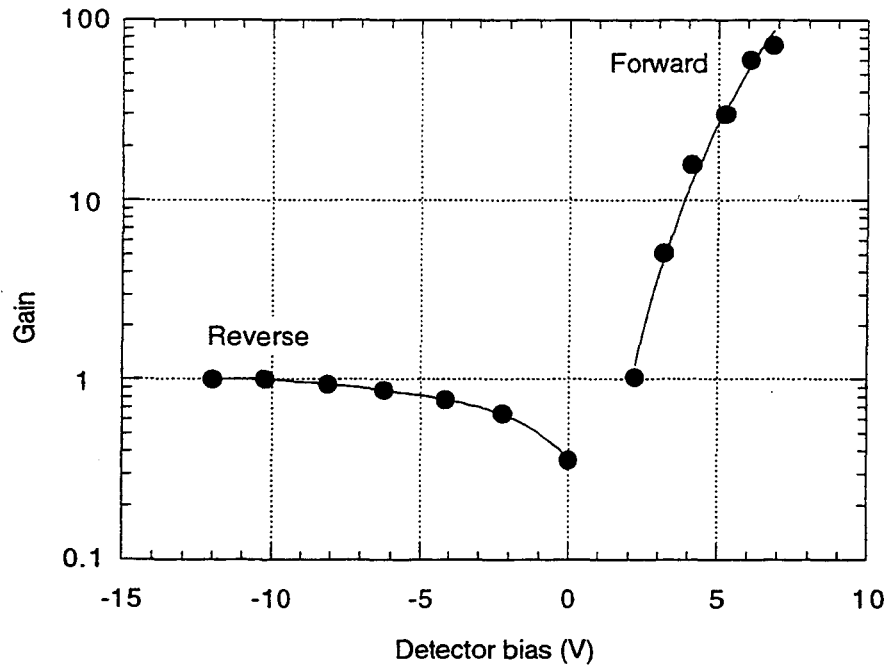
(a)
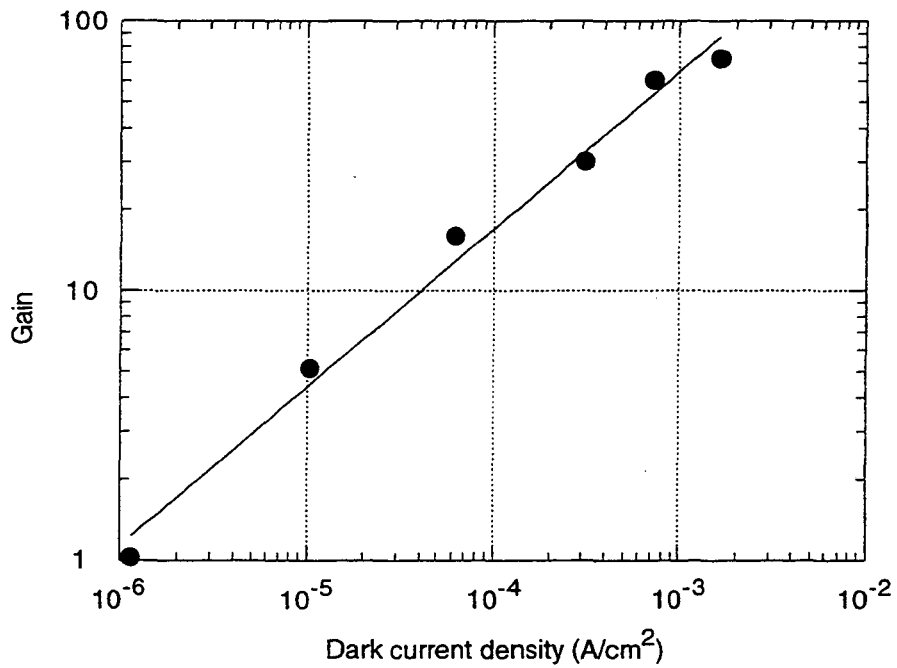
(b)

Fig. 5-9   The current gain as a function of (a) detector bias
and (b) dark current density in 1 μm n-i-p-i-n diode.
10 msec of light was exposed.
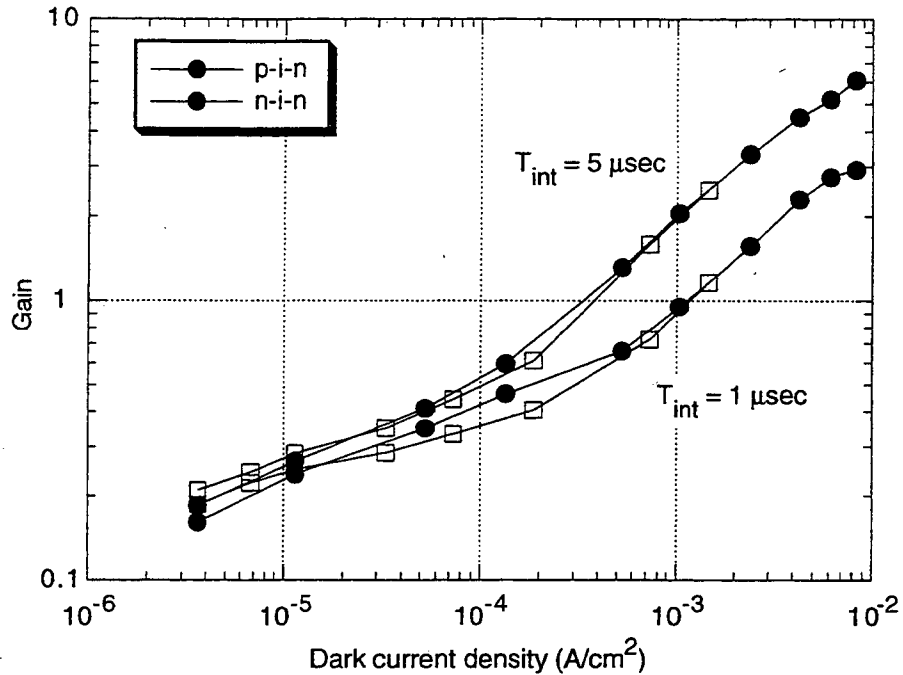
Fig. 5-10 The charge gains of p-i-n and n-i-n devices for 0.2 μsec of light pulse. The integration time was controlled in the shaping amplifier.

the n-i-p-i-n diodes. The maximum gains obtained with our best samples at a dark current density of 10 mA/cm^2 were 6 and 9 for integration times of 1 μsec and 5 μsec, respectively. These maximum values were achieved after annealing the samples at 160°C for a week. The annealing effects are discussed in Section 5.4.4.

5.4.3 Decay Characteristics

In order to investigate the characteristics of the current decay, which is related to the charge gains, the photocurrents of p-i-n and n-i-n devices after a short pulse of light were measured. In Fig. 5-11 (a) and (b), the
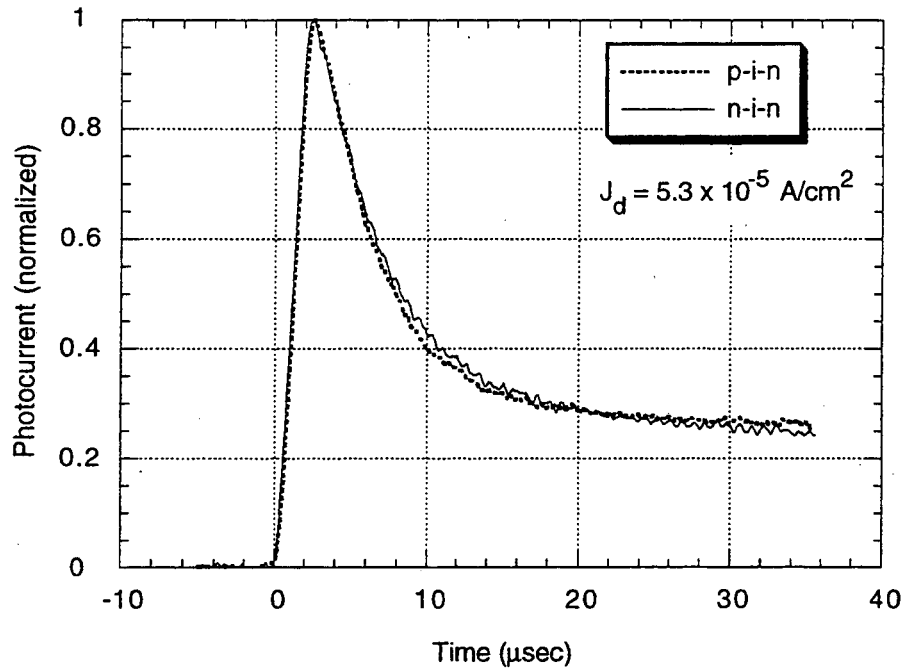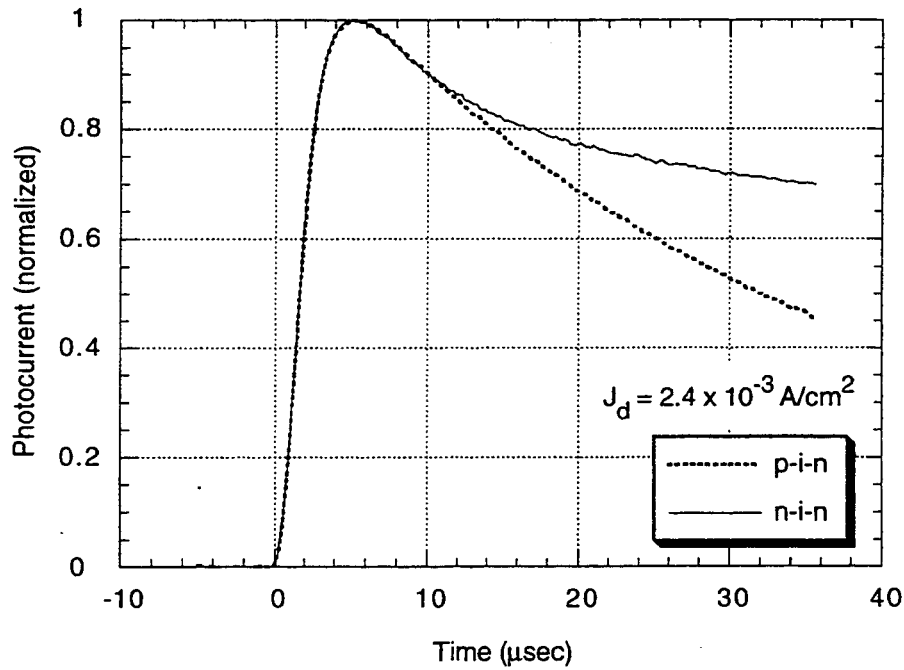
Fig. 5-11   The decaying photocurrent shapes of p-i-n and n-i-n devices after a short light pulse at two different dark current levels.

measured photocurrent shapes at two different dark current densities are compared. At the same dark current densities, the initial decay times of the p-i-n and n-i-n devices are almost identical, and this explains why their gains are almost the same for the short light pulses at any dark current level. At higher dark current levels, however, the photocurrent of the p-i-n diode decays faster than that of the n-i-n device for the longer time scales as shown in Fig. 5-11 (b). To extract more information about the decay characteristics in long time scales, the time ($T_{30\%}$) taken to reach 30% of the peak photocurrent after 1 msec of light exposure was measured with p-i-n diode and n-i-n device, and the results are shown in Fig. 5-12 (a) and (b). The $T_{30\%}$ of the n-i-n device increases approximately linearly with the detector bias and proportional to $J_d^{0.4}$, while that of the p-i-n diode decreases as the bias increases and is approximately proportional to the reciprocal of the detector bias and also proportional to $J_d^{-0.3}$. The decreasing decay time constant ($T_{30\%}$) in the p-i-n diode may be explained by the decrease of the electron lifetime. As the forward bias increases, the dark current increases due to the increased amount of electrons and holes by double injections from the contacts, and correspondingly the quasi-Fermi energy levels of the electrons and holes move toward the band edges since they are related to the free carrier densities as

$$E_c - E_{Fn} = kT \ln\left(\frac{N_c}{n_f}\right)$$

$$E_{Fp} - E_v = kT \ln\left(\frac{N_v}{p_f}\right) \quad , \qquad (5\text{-}15)$$

where E_c is the conduction band edge, E_v is the valence band edge, E_{Fn} and E_{Fp} is the quasi-Fermi energy level of electrons and holes, respectively, N_c
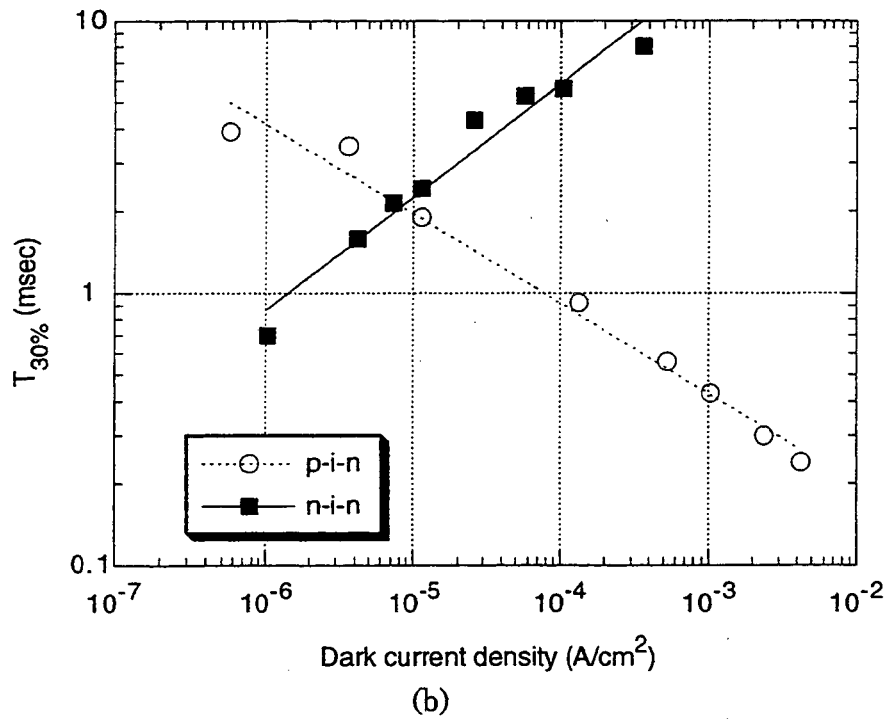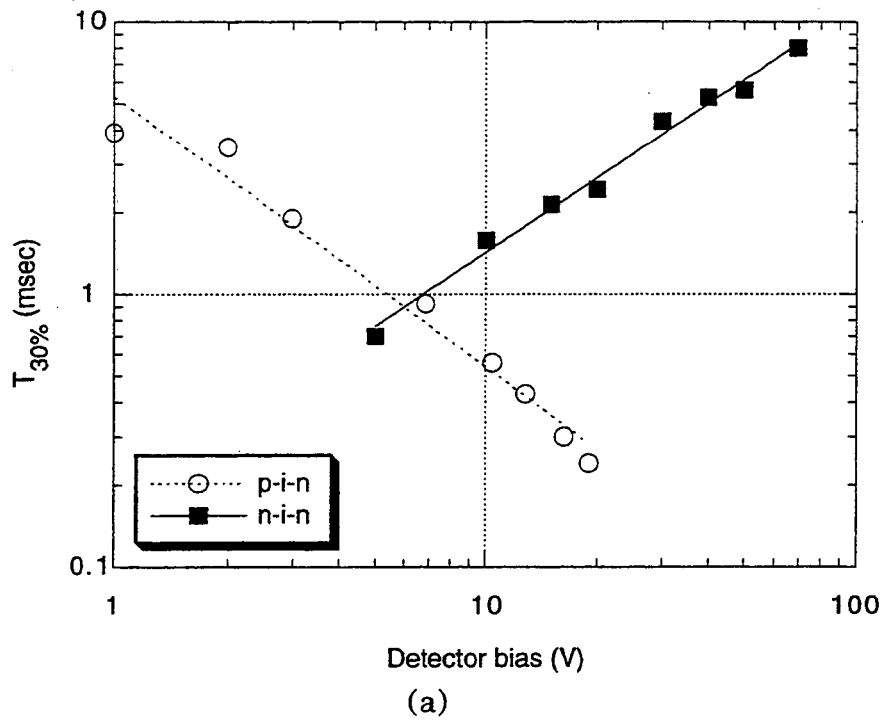
Fig. 5-12 $T_{30\%}$ of p-i-n and n-i-n devices. $T_{30\%}$ is defined in
the text.

and N_v is the density of states at the conduction band edge and valence band edge, respectively, n_f is the free electron density and p_f is the free hole density. Accordingly, the demarcation levels also move toward the band edges making the recombination centers broadened,[7,23,24] therefore more recombination of electrons and holes occurs and eventually the lifetime of the electrons is decreased. Due to this decrease in the lifetime, the photocurrent of the p-i-n diode decreases at high forward biases, since J_{ss} in Eq. (5-10) and (5-13) is proportional to the electron lifetime τ_l. At low biases, however, the increase of the value in the parenthesis in Eq. (5-10) is more dominant than the decrease in J_{ss} with the bias, hence the photocurrent increases with the bias. The decrease of electron lifetime and photoconductive gain with the increase of voltage in p-i-n diodes has also been found by others.[12,13]

5.4.4 Annealing Effects

In a-Si:H the dangling bonds are known to be the dominant recombination centers.[7-9] Therefore, if the density of the dangling bonds is reduced somehow the recombination rate will be reduced and the lifetime of the electrons will be increased. The effect of the dangling bond density on the steady state photoconductivity has been investigated by many groups and the increase in dangling bond density has been found to cause reduction in photoconductivity.[8,13,40] It has been shown that the increased defect densities in the degraded a-Si:H devices can be reduced almost to the original values by annealing,[41-44] and improvements of the
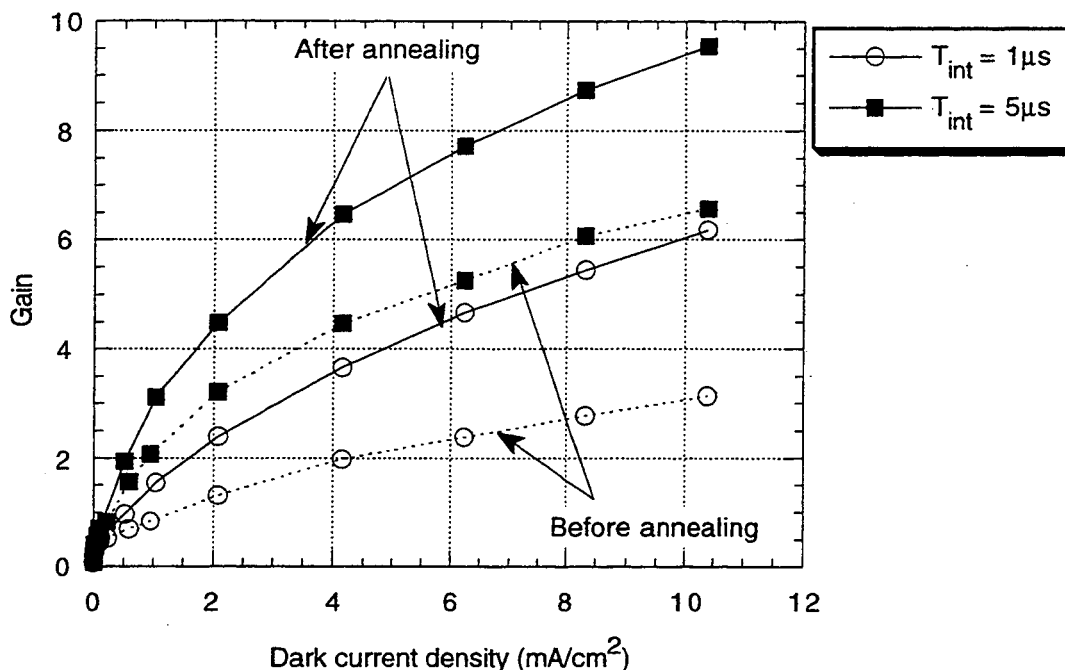
Fig. 5-13   Charge gains in a 14 μm p-i-n diode for 0.2 μsec
light pulse before and after annealing.

steady state photoconductivity in degraded samples by annealing have also
been reported.[13,42]

Some of the p-i-n and n-i-n samples were annealed at 160 °C for a
week and the ionized dangling bond densities were reduced to 60 ~ 70% of
the original values.   After annealing both the current gains and charge
gains in p-i-n and n-i-n devices were improved to 120% ~ 200% of the values
before annealing, indicating that the dangling bond density was reduced
and the electron lifetime was increased as a result of annealing.   The
improvement of the charge gains after annealing in a 14 μm p-i-n diode for
0.2 μsec light pulses is shown in Fig. 5-13 as an example.   For 1 μsec of
integration time, the gain at a dark current density of 10 mA/cm^2 was
improved by 100% after annealing.

5.4.5 Measurements with Actual Radiation Sources

The long light pulse measurements with n-i-n devices were repeated using an x-ray source instead of an LED. A 900 μm CsI(Tl) layer was coupled to the n-i-n device during measurements. The gain behavior was the same as in the case of using LED light, that is, proportional to $J_d{}^{0.6}$. In order to see the response of the photocurrent to the variation of the light intensity, the photocurrents were measured with various x-ray intensities at different dark current densities, and are plotted in Fig. 5-14 as functions of light intensity.[45] The photocurrents are proportional to the 0.9 power of the light intensity. The power law dependence of the photocurrent on the light intensity is a quite common characteristic of the photocurrent in photoconductors.[20,23,24]
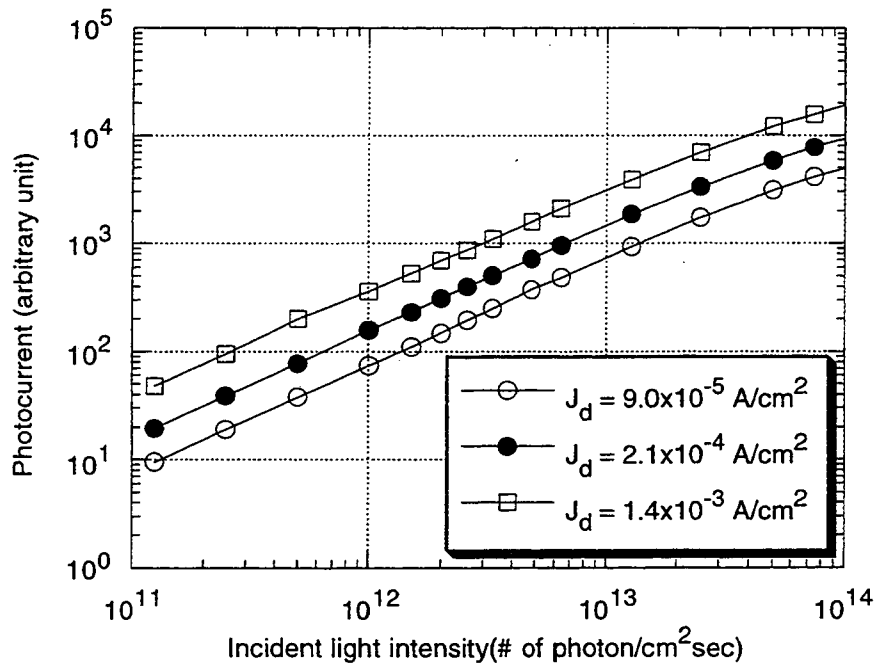
Fig. 5-14 Response of the photocurrent in an n-i-n device to the variation of the light intensity.
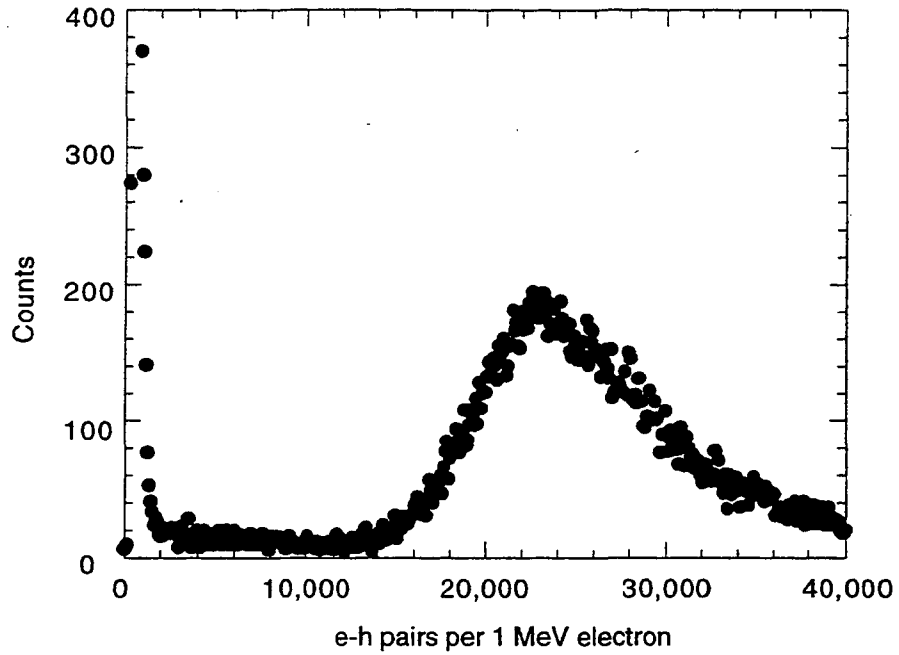
(a)
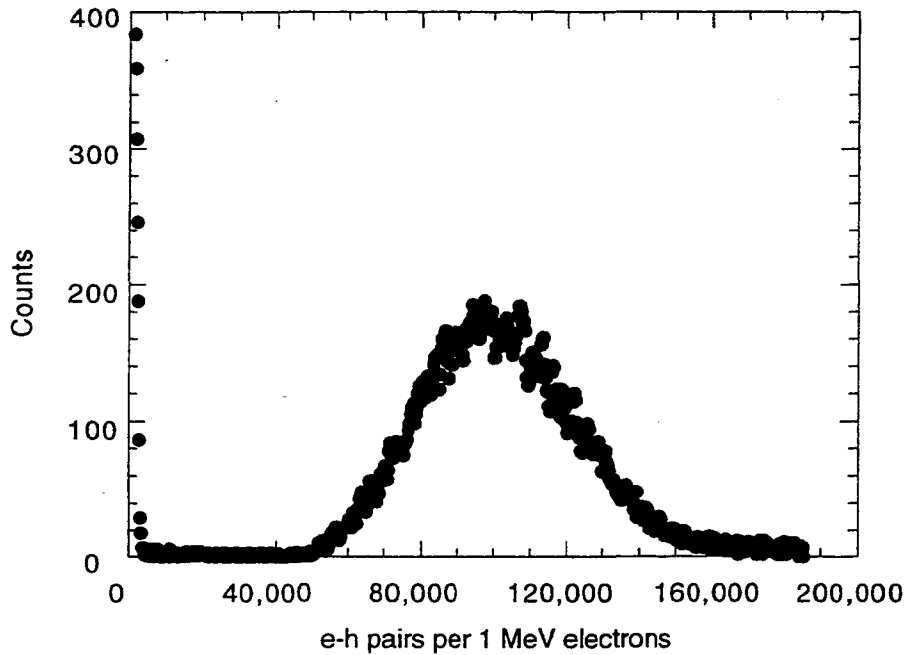
(b)

Fig. 5-15   Pulse height spectrum of 1 MeV beta particles
measured with a p-i-n diode coupled to CsI(Tl) in (a)
reverse bias and (b) forward bias.

146

Using the short pulse measurement system with a p-i-n diode coupled to CsI(Tl), the beta particles from a Sr^{90} source were measured both in reverse and forward bias. The pulse height spectrum of the measured signal in reverse bias and forward bias is shown in Fig. 5-15 (a) and (b), respectively.[45] It is easily seen in these graphs that the signal size was increased by a factor of about four in forward bias compared to the signal in reverse bias, and as much as ~92,000 electron-hole pairs were collected in forward bias for a 1 MeV beta particle. The signal in forward bias, however, has a higher noise level which is mainly shot noise due to the high dark current. But the same gain with less noise can be achieved by making the pixel area small since the gain is dependent on the dark current density while the noise is dependent on the total dark current rather than dark current density.

5.5   Discussion

The transient photoconductive gains were measured with p-i-n, n-i-n and n-i-p-i-n devices. For rather long light pulses ($\geq$ 1 msec), n-i-n and n-i-p-i-n devices showed higher gains than p-i-n diodes, while for short pulses (< 1 μsec) the gain was almost the same for all the devices. The decay times of the p-i-n diode and n-i-n device were almost identical in short time scales, hence the gains were almost the same. In longer time scales, however, the decay time of the photocurrent in p-i-n diodes decreased as the forward bias was increased, which caused the photoconductive gain to decrease at high biases. The decrease of the decay time in p-i-n diodes at high dark current level is expected to be due to the decrease of electron

lifetime. The gains were improved by annealing at 160 °C, and the maximum gain of 9 could be obtained for short light pulses with 5 μsec of integration time at a dark current density of ~10 mA/cm^2, and more than 200 could be achieved for 1 msec light pulses with 5 msec integration time at the same dark current density. Using a beta-ray source the actual radiation measurements were performed, and with a gain of about four, 92,000 electron-hole pairs on average could be collected from a 1 MeV beta particle. From x-ray intensity measurements, the output photocurrent of an n-i-n device was found to be proportional to 0.9 power of the light intensity, which is a general behavior in most photoconductors. As the gain is high with a long light pulse, the photoconductive mechanism may be applied to medical x-ray imaging such that the dose to patients can be reduced at the same signal size. Single charged particle detection using photoconductive gain mechanism is expected to have higher noise level due to higher dark current compared to the conventional methods of radiation detection using reverse biased a-Si:H p-i-n diodes. This can, however, be reduced by making pixels with small area. As the photoconductive gain depends on the dark current density, the same gain can still be obtained with reduced pixel area, while the shot noise is reduced by the decreased pixel area.

References

[1]   W. Guang-Pu, H. Okamoto and Y. Hamakawa, "Amorphous-Silicon Photovoltaic X-Ray Sensor," Jpn. J. Appl. Phys., 24, 1105 (1985)

[2]   V. Perez-Mendez, J. Morel, S. N. Kaplan and R. A. Street, "Detection of Charged Particles in Amorphous Silicon Layers," Nucl. Instr. and Meth., 252, 478 (1986).

[3]   V. Perez-Mendez, "Charged Particle, Gamma Ray, and Light Detection in Amorphous Silicon Devices," Chapter 8 in *Amorphous & Microcrystalline Semiconductor Devices*, edited by J. Kanicki, Artech House, Boston (1991)

[4]   I. Fujieda, G. Cho, J. Drewerey, T. Gee, T. Jing, S. N. Kaplan, V. Perez-Mendez and D. Wildermuth, "X-Ray and Charged Particle Detection with CsI(Tl) Layer Coupled to a-Si:H Photodiode Layers," IEEE Trans. Nuc. Sci., NS-38, 255 (1991).

[5]   H. K. Lee, J. S. Drewery, W. S. Hong, T. Jing, S. N. Kaplan, A. Mireshghi and V. Perez-Mendez, "Hydrogenated Amorphous Silicon (a-Si:H) Based Gamma Camera - Monte Carlo Simulations," SPIE Vol. 2163, Medical Imaging 1994: Physics of Medical Imaging, 427 (1994)

[6]   A. Mireshghi, G. Cho, J. S. Drewery, W. S. Hong, T. Jing, H. K. Lee, S. N. Kaplan and V. Perez-Mendez, "High Efficiency Neutron Sensitive Amorphous Silicon Pixel Detectors," IEEE Trans. Nucl. Sci., 41, 915 (1994)

[7]   R. S. Crandall, "Photoconductivity," Chapter 8 in *Semiconductors and Semimetals*, Vol. 21, Part B, edited by J. I. Pankove, Academic Press, Inc., Orlando (1984)

[8]   T. J. McMahon and R. S. Crandall, "Hole Trapping, Light Soaking, and Secondary Photocurrent Transients in Amorphous Silicon," Phys. Rev. B, 39, 1766 (1989)

[9] R. A. Street, *Hydrogenated Amorphous Silicon*, Cambridge University Press, Cambridge, (1991)

[10] R. Williams and R. S. Crandall, "Carrier Generation, Recombination, and Transport in Amorphous Silicon Solar Cells," RCA Rev., 40, 371 (1979)

[11] M. Hack, M. Shur and C. C. Tsai, "Amorphous Silicon Photoconductive Diode," Appl. Phys. Lett., 54, 96 (1989)

[12] F. A. Rubinelli, J. Y. Hou and S. J. Fonash, "Bias-Voltage- and Bias-Light-Dependent High Photocurrent Gains in Amorphous Silicon Schottky Barriers," J. Appl. Phys., 73, 2548 (1993)

[13] R. Vanderhaghen, R. Amokrane, D. Han and M. Silver, "Effect of Light-Induced Degradation on Photoconductive Gain in a-Si:H n-i-p devices," J. Non-Cryst. Solids, 164-166, 599 (1993)

[14] Y. Suda, K. Suzuki and T. Saito, "Matrix-Driven Contact Image Sensor," Toshiba Rev., No. 160, 43 (1987)

[15] T. Saito, K. Suzuki, T. Nakai, Y. Suda, S. Takayama, K. Mori, O. Shimada, K. Sasaoka, T. Sakano, Y. Fukumoto and K. Ambo, "Amorphous Silicon Photoconductive Contact Image Sensor," Extended Abstracts of the 18th Conference on Solid State Devices and Materials, Tokyo, 703 (1986)

[16] T. Hamano, H. Ito, T. Nakamura, T. Ozawa, M. Fuse and M. Takenouchi, "An Amorphous Si High Speed Linear Image Sensor," Jpn. J. Appl. Phys., 21, 245 (1982)

[17] T. Kagawa, N. Matsumoto and K. Kumabe, "Amorphous Silicon Photoconductive Sensor," Jpn. J. Appl. Phys., 21, 251 (1982)

[18] T. Saika, N. Kaifu, I. Gofuku, K. Hatanaka, K. Ichihashi and T. Komatsu, "Integrated a-Si:H Linear Image Sensor Using TFT Type Photo-Sensor," Extended Abstracts of the 19th Conference on Solid State Devices and Materials, Tokyo, 509 (1987)

[19]   K. Rosan, "Amorphous Semiconductor Image Sensors: Physics, Properties, and Performance," Chapter 7 in *Amorphous & Microcrystalline Semiconductor Devices*, edited by J. Kanicki, Artech House, Boston (1991)

[20]   R. G. Stearns and R. L. Weisfield, "Two-Dimensional Amorphous-Silicon Photoconductor Array for Optical Imaging," Appl. Optics, 31, 6874 (1992)

[21]   T. Jing, C. A. Goodman, J. S. Drewery, G. Cho, W. S. Hong, H. K. Lee, S. N. Kaplan, A. Mireshghi, V. Perez-Mendez and D. Wildermuth, "Amorphous Silicon Pixel Layers with Cesium Iodide Converters for Medical Radiography," IEEE Tran. Nucl. Sci., 41, 903 (1994)

[22]   H. K. Lee, J. S. Drewery, W. S. Hong, T. Jing, S. N. Kaplan and V. Perez-Mendez, "Utilization of Photoconductive Gain in a-Si:H Devices for Radiation Detection," To be presented at MRS Meeting in April at San Francisco (1995)

[23]   A. Rose, *Concepts in Photoconductivity and Allied Problems*, Interscience Publishers, New York (1963)

[24]   R. H. Bube, *Photoconductivity of Solids*, John Wiley & Sons, Inc., New York (1960)

[25]   F. W. Schmidlin, "Theory of Trap-Controlled Transient Photo-conduction," Phys. Rev. B, 16, 2362 (1977)

[26]   N. V. Joshi, "Analytical Approach towards Transient Phenomena in Photoconductors," Phys. Rev. B, 27, 6272 (1983)

[27]   N. V. Joshi and J. M. Martin, "New Technique for Analyzing Relaxation Curves in Photoconductors," Phys. Lett., 113A, 318 (1985)

[28]   R. Pandya and E. A. Schiff, "A Multiple-Trapping Model with Optical Bias," Philos. Mag. B, 52, 1075 (1985)

[29] R. J. Fleming, "Trap-Controlled Transient Photoconductivity in Dielectrics," J. Appl. Phys. 50, 8075 (1979)

[30] J. -H. Zhou and S. R. Elliott, "Deep Trapping and Recombination in Hydrogenated Amorphous Silicon," Philos. Mag. B, 69, 147 (1994)

[31] R. S. Crandall, "Mobility-Lifetime Products in Hydrogenated Amorphous Silicon," Appl. Phys. Lett., 58, 508 (1991)

[32] H. Antoniadis and E. A. Schiff, "Unraveling the $\mu\tau$ Mystery in a-Si:H," J. Non-Cryst. Solids, 137&138, 435 (1991)

[33] C. Main, J. Berkin, R. Bruggemann and J. M. Marshall, "Excess Carrier Dispersion in Conventionally Dispersive Amorphous Semiconductors and the Mobility-Lifetime Anomaly in a-Si:H," J. Non-Cryst. Solids, 137&138, 439 (1991)

[34] M. A. Lampert and P. Mark, *Current Injection in Solids*, Academic Press, New York (1970)

[35] A. Rose, "Space-Charge-Limited Currents in Solids," Phys. Rev., 97, 1538 (1955)

[36] G. G. Roberts and F. W. Schmidlin, "Study of Localized Levels in Semi-Insulators by Combined Measurements of Thermally Activated Ohmic and Space-Charge-Limited Conduction," Phys. Rev., 180, 785 (1969)

[37] K. D. Mackenzie, P. G. LeComber and W. E. Spear, "The Density of States in Amorphous Silicon Determined by Space-Charge-Limited Current Measurements," Philos. Mag. B., 46, 377 (1982)

[38] M. Hack and W. den Boer, "A Comparison of Single- and Double-Carrier Injection in Amorphous Silicon Alloys," J. Appl. Phys., 58, 1554 (1985)

[39] M. Hack and M. Shur, "Theoretical Modeling of Amorphous Silicon-Based Alloy p-i-n Solar Cells," J. Appl. Phys., 54, 5858 (1983)

[40]   E. Morgado, "Recombination at Correlated Dangling Bonds and the Effects of Fermi Level Position on Steady-State Photoconductivity in Amorphous Silicon," Philos. Mag. B, 63, 529 (1991)

[41]   Y. Kitsuno, G. Cho, J. S. Drewery, W. S. Hong and V. Perez-Mendez, "Defect Equilibration and Intrinsic Stress in Undoped Hydrogenated Amorphous Silicon," Jpn. J. Appl. Phys., (1993)

[42]   T. J. McMahon and R. Tsu, "Equilibrium Temperature and Related Defects in Intrinsic Glow Discharge Amorphous Silicon," Appl. Phys. Lett., 51, 412 (1987)

[43]   T. J. McMahon, "Defect Equilibration and Metastability in Low-Spin-Density Amorphous Hydrogenated Silicon," Solar Cells, 30, 235 (1991)

[44]   T. J. McMahon, "Defect Equilibration and Stabilization in Low-Spin-Density a-Si:H," Phys. Rev. B, 45, 4512 (1992)

[45]   T. Jing, C. A. Goodman, J. S. Drewery, W. S. Hong, H. K. Lee, S. N. Kaplan, V. Perez-Mendez and D. Wildermuth, "Detection of Charged Particles and X-Rays by Scintillator Layers Coupled to Amorphous Silicon Photodiode Arrays," To be published in Nucl. Instr. and Meth.

Chapter 6   Conclusion

Hydrogenated amorphous silicon radiation detectors have been investigated in connection with applications to medical imaging. Utilizing the capability of large area deposition and high radiation hardness, the a-Si:H pixel arrays can be used in digital radiography and radioisotope imaging in nuclear medicine. For x-ray and γ-ray imaging, pixel arrays of thin a-Si:H p-i-n photodiodes are coupled to a scintillating layer such as CsI(Tl).

Prototypes of a-Si:H based gamma cameras were designed and their performances were estimated from Monte Carlo simulations. These cameras do not need the photomultiplier tubes, hence their size and weight are less then those of the conventional gamma cameras. Two types of a-Si:H based gamma cameras were proposed. One (type A) is composed of a scintillating layer, an a-Si:H p-i-n photodiode pixel array and a charge sensitive preamplifier in each pixel, and would be operated in the event-by-event mode with γ-energy selection as conventional gamma cameras. A type A camera, however, requires complex fabrication processes due to the pixel amplifiers. The other (type B) is composed of a scintillating layer and a-Si:H p-i-n photodiode pixels which are attached to storage capacitors, and would be operated in the current-integrating mode, in which scattered γ photons cannot be rejected. In order to predict the performance of the proposed type B a-Si:H based gamma camera, Monte Carlo codes were made using Fortran 77, and the effect of γ scattering was extensively investigated. From the simulation results, the intrinsic spatial resolution of the proposed a-Si:H based gamma camera (FWHM < 3 mm) was better than that of the conventional gamma cameras (FWHM = 3 ~ 4 mm). Due to

the γ scattering, however, the images obtained with the type B a-Si:H based gamma camera were more blurred than those of conventional gamma cameras. The blurred images, however, were improved considerably by deconvolution such as Wiener filtering. According to the simulation results, type B a-Si:H based gamma cameras should be suitable for imaging shallow organs such as the thyroid.

Prototype samples of a charge-storage pixel detector suitable for a type B a-Si:H based gamma camera were made and the storage performance in terms of background charge generation and maximum storage time was investigated. It was found that at room temperature, the thermal generation current was so high that the storage capacitor was saturated with the background charge in a short time, but, as the thermal generation process is significantly dependent on the ambient temperature, the background charge could be reduced remarkably by lowering the temperature. At -20°C, for example, the test samples could store the signal charge as long as 5 min with little influence from background charge. In order to estimate the charge storage behavior, thermal generation current in a reverse biased a-Si:H p-i-n diode was also investigated theoretically. The measurements and theoretical calculation results were in excellent agreement, and showed that the Poole-Frenkel effect was the dominant source of thermal generation current under our operation conditions. A voltage- and time-dependent thermal generation current model for the charge storage pixel detector was developed, with which the operation conditions of the proposed gamma cameras could be predicted.

The transient photoconductive gain in a-Si:H was investigated with various configurations of devices such as p-i-n, n-i-n and n-i-p-i-n in

155

connection with applications to digital radiography and more general radiation detection. For short light pulses (< 1 μsec), which simulate the fast transit of charged particles, the gain was almost the same for all the devices at the same dark current level, while for rather longer light pulses ($\geq$ 1 msec), which simulate the x-ray exposure in digital radiography, n-i-n and n-i-p-i-n devices produced higher gains than p-i-n diodes. In order to study the characteristics of the transient photoconductive gain, the decay times of the photocurrent were measured. From the experimental results, the decay times of the photocurrents in short time scales (< 10 μsec) were almost the same in all devices at the same dark current level, while on longer time scales (> 10 μsec) the photocurrents in p-i-n diode decayed faster than those of the other devices. This explains why the gains for the short light pulses are almost the same in all devices but are lower in p-i-n diodes for the long light pulses at the same dark current levels. With short light pulses (0.2 μsec) a maximum gain of 9 could be achieved, and for long light pulses (1 msec) the gain was more than 200. As the gain is high for long light pulses, this photoconductive gain mechanism can enhance the signal levels in digital radiography, or, at the same signal size, the dose to patients can be reduced.

Appendix

Programs for the Monte Carlo Simulations in Chapter 3

C OBJECTIMAGE.FOR (Main Code)

C This program simulates the IMAGE of the gamma rays from distributed sources in
C WATER PHANTOM.
C The output is the distribution of the photons in a 2-D detector array

```
      REAL FWHMDATA(17)
      REAL IMAGE_HNRATIO, IMAGE(128,128), NGAMMA
      REAL ESPECT(256)
      DOUBLE PRECISION NCST,NPA,NOB,NLE,NTOTAL,NCOLL,
     +      NSCINT,SCST,SPAT,SEST,VDETT, MU, WZ1, STRANGE
      INTEGER*4 NORMALSPOT,HOTSPOT,PNORMAL,PHOT
      CHARACTER COLTYPE*16
      DATA IMAGE/16384*0./
      DATA ESPECT/256*0./
      OPEN (1,FILE='RAN-SEED.DAT',STATUS='OLD')
      OPEN (3,FILE='HIGH-RESOL.DAT',STATUS='OLD')
      OPEN (10,FILE='SUMMARY.OUT',STATUS='NEW')
      READ (1,*) IX
```

C Constants and Source Parameters
```
      PI = 3.141592654
      EGS = 140.E-3                 !Source Energy              [MeV]
      NGAMMA = 1.0E9                !total # of Gamma Sources in source object
      IMAGE_HNRATIO = 3.0           !Hot/Normal ratio in detector image
      PNORMAL = 1992                !# of normal source elements
      PHOT = 8                      !# of hot source elements
! # of elements along a vertical line which passes the hot elements
      LINE_NORMAL = 8
      LINE_HOT = 2
! # of Gamma Sources in a normal and hot source elements
      TERMM = (IMAGE_HNRATIO*(LINE_NORMAL+LINE_HOT)-
      LINE_NORMAL)/LINE_HOT
      NORMALSPOT = NINT(NGAMMA/(PNORMAL+PHOT*TERMM))
      HOTSPOT = NORMALSPOT*NINT(TERMM)
      SOURCE_HNRATIO = FLOAT(HOTSPOT/NORMALSPOT)
```

C Geometrical Parameters
! 1. Source Distribution
```
      XSRCH = 4.0                   !Object max x-value         [cm]
      XSRCL = -XSRCH                ! " "     min   " "         [cm]
      YSRCH = 2.0                   ! " "     max y-value       [cm]
      YSRCL = -YSRCH                ! " "     min   " "         [cm]
      ZSRCH = 11.0                  ! " "     max z-value       [cm]
      ZSRCL = 7.0                   ! " "     min   " "
      NSRCX = 20                    !# of pixels in x-direction
      NSRCY = 10                    !  " "          y   " "
```

```
            NSRCZ = 10                        !    " "           z   " "
            DELSRC = 0.4                      !Pixel size of the Object         [cm]
! 2. Water Phantom
            XPH = 15.0                        !Phantom max. x-value             [cm]
            XPL = -XPH                        ! " "       min.   " "            [cm]
            YPH = 15.0                        ! " "       max. y-value          [cm]
            YPL = -YPH                        ! " "       min.   " "            [cm]
            ZPH = 15.                         ! " "       max. z-value          [cm]
            ZPL = 0.                          ! " "       min.   " "            [cm]
! 3. Collimator
!   Type: High-Resolution
            COLTYPE = 'High-Resolution '
            READ (3,*) DELC
            READ (3,*) (FWHMDATA(J),J=1,17)
            XCH = 8.4
            XCL = -XCH
            APPROX = (XCH-XCL)/DELC
            NC = INT(APPROX)                  !NC^2 = # of collimator pixels
            IF (APPROX.GT.NC) NC=NC+1

            XCH = FLOAT(NC)*DELC/2.           !Collimator max. x-value      [cm]
            XCL = -XCH                        !   " "            min.  " "   [cm]
            YCH = XCH                         !   " "            max. y-value [cm]
            YCL = -YCH                        !   " "            min.   " "   [cm]
! 4. Scintillator
            XSH = 8.4                         !Scint. max. x-value          [cm]
            XSL =-XSH                         !Scint. min. x-value          [cm]
            YSH = XSH                         !Scint. max. y-value          [cm]
            YSL =-YSH                         !Scint. min. y-value          [cm]
            ZSH = 0.5                         !Scint. max. z-value (top)    [cm]
            ZSL = 0.0                         !Scint. min. z-value (bottom) [cm]
! 5. Detector
            XDH = 6.4                         !Detector max. x-value        [cm]
            XDL =-XDH                         !Detector min. x-value        [cm]
            YDH = XDH                         !Detector max. y-value        [cm]
            YDL =-YDH                         !Detector min. y-value        [cm]
            ND = 128                          !ND^2 = # of detector pixels
            DELD = (YDH-YDL)/FLOAT(ND)        !Detector Pixel Size          [cm]
C
C Energy Spectrum Parameters
C
            EMIN = 0.0                        !Min. gamma energy            [MeV]
            EMAX = EGS                        !Max. gamma energy            [MeV]
            NE = 256                          !# of energy channels
            DELE = (EMAX-EMIN)/FLOAT(NE-1)    !Energy width for each channel[MeV]
            EMINV = EMIN - DELE*0.5           !                             [MeV]
            EMAXV = EMAX + DELE*0.5           !                             [MeV]
C
C Print System Specifications
C
            CALL HEADING (EGS,NORMALSPOT,HOTSPOT,PNORMAL,PHOT,
     +          LINE_NORMAL,LINE_HOT,NGAMMA,SOURCE_HNRATIO,
     +          IMAGE_HNRATIO,XSRCH,YSRCH,ZSRCH,ZSRCL,NSRCX,
     +          NSRCY,NSRCZ,DELSRC,XPH,YPH,ZPH,COLTYPE,XCH,YCH,
```

```
      +             NC,DELC,XSH,YSH,ZSH,XDH,YDH,ND,DELD,EMIN,EMAX,
      +             NE,DELE)
C
C Number of Events
C
! 1. In the Water Phantom
            NCST = 0.0              !Total # of Compton Scatterings
            NPA = 0.0               !Total # of Photoelectic Absorptions
            NOB = 0.0               !Total # of Out of Boundary Escapings
            NLE = 0.0               !Total # of Too Low Photon Energy Events

! 2. In the Collimator
            NCOLL = 0.0             !Total # of Gamma Photons Arrived at Collimator
            NSCINT = 0.0            !Total # of Detected Gamma Photons

! 3. In the Scintillator (CsI(Tl))
            SCST = 0.0              !Total # of Compton Scatterings
            SPAT = 0.0              !Total # of Photoelectric Absorption
            SEST = 0.0              !Total # of Escaping of Gamma Photons
            VPHOTT = 0.0            !Total # of Generated Visible Photons
            VDETT = 0.0             !Total # of Undetected Visible Photons

            DO 105 KZ=1,NSRCZ
            DO 102 KY=1,NSRCY
            DO 100 KX=1,NSRCX
                XS1 = XSRCL + FLOAT(KX-1)*DELSRC
                YS1 = YSRCL + FLOAT(KY-1)*DELSRC
                ZS1 = ZSRCL + FLOAT(KZ-1)*DELSRC
C
C Source Strength
C
            IF ((KX.GE.10).AND.(KX.LE.11).AND.(KY.GE.5).AND.(KY.LE.6).AND.
      +        (KZ.GE.5).AND.(KZ.LE.6)) THEN
                NSOURCE = HOTSPOT
            ELSE
                NSOURCE = NORMALSPOT
            ENDIF

            DO 100 I=1,NSOURCE

                XS = XS1 + RAN(IX)*DELSRC
                YS = YS1 + RAN(IX)*DELSRC
                ZS = ZS1 + RAN(IX)*DELSRC

C
C In the Water Phantom
C
                NCS = 0        !# of Compton Scatterings for a Single Gamma Ray

                EG1 = EGS
                X1 = XS
                Y1 = YS
                Z1 = ZS
```

```
! Direction of Source Photon (Isotropic)
        PHI = RAN(IX)*2.*PI
912     WZ1 = -1. + RAN(IX)                         !Isotropic btwn Wz = -1 ~ 0
        IF ((WZ1.LT.-1.).OR.(WZ1.GT.0.)) GOTO 912
        SQRTWZ1 = SQRT(1.-WZ1**2.)
        WX1 = SQRTWZ1*COS(PHI)
        WY1 = SQRTWZ1*SIN(PHI)


! Next Collision Position
20      CALL CROSSWATER(EG1,SIGC,SIGP,SIGT)    !Cross-Sections in
                                               !Water          [cm^-1]

        H = RAN(IX)
        IF (H .EQ. 0.0) GOTO 20
        S = -LOG(H)/SIGT                       !Traveling Distance        [cm]
        X2 = X1 + S*WX1                        !x-position of collision   [cm]
        Y2 = Y1 + S*WY1                        !y-position of collision   [cm]
        Z2 = Z1 + S*WZ1                        !z-position of collision   [cm]
        IF (Z2.GT.ZPH) THEN
            GOTO 30                            !Out of Boundary
        ELSEIF (Z2.LT.ZPL) THEN
            XC = X1 - Z1*WX1/WZ1               !x-value of Photon Position on Collimator
            YC = Y1 - Z1*WY1/WZ1               !y-value of Photon Position on Collimator
            IF ((XC.LT.XCL).OR.(XC.GT.XCH)) GOTO 30     !Out of Coll.Boundary
            IF ((YC.LT.YCL).OR.(YC.GT.YCH)) GOTO 30     ! "  "      "  "
            GOTO 40                            !Photon Arrived at Collimator
        ELSE
            IF ((X2.LT.XPL).OR.(X2.GT.XPH)) GOTO 30     !Out of Boundary
            IF ((Y2.LT.YPL).OR.(Y2.GT.YPH)) GOTO 30     ! "  "
        ENDIF


! Collision Type
        PP = SIGP/SIGT                         !Probability of Photoelectric Effect
        H = RAN(IX)
! 1.Photoelectric Absorption
        IF (H.LE.PP) THEN
                NPA = NPA + 1.0
                GOTO 50
        ENDIF


! 2.Compton Scattering
911     CALL COMPTONR(IX,EG1,EG2,MU)       !Obtain Eg2 and mu
        IF ((MU.LT.-1.).OR.(MU.GT.1.)) GOTO 911
        NCS = NCS + 1


! Photon with Too Low Energy
        IF (EG2.LT.0.01) THEN
                NLE = NLE + 1.0
                GOTO 50
        ENDIF
! Direction of Scattered gamma Ray
        PHI = 2*PI*RAN(IX)  !Sampling of azimuthal angle(isotropic)     [radian]
        CP = COS(PHI)
        SP = SIN(PHI)
```

```fortran
        IF ((WZ1.EQ.-1.0).OR.(WZ1.EQ.1.0)) THEN
              TERM1 = SQRT(1.-MU**2.)
              WX2 = TERM1*CP
              WY2 = TERM1*SP
              WZ2 = WZ1*MU
        ELSE
              STRANGE = (1.-MU**2.)/(1.-WZ1**2.)
              IF (STRANGE.LT.0.0) THEN
                    WRITE(*,*) 'MU=',MU,' WZ1=',WZ1,
     +                          'NEGATIVE STRANGE'
                    GOTO 50
              ENDIF
              TERM1 = SQRT(STRANGE)
              WX2 = TERM1*(WY1*CP + WX1*WZ1*SP) + WX1*MU
              WY2 = TERM1*(-WX1*CP + WY1*WZ1*SP) + WY1*MU
              WZ2 = -SQRT((1.-WZ1**2.)*(1.-MU**2.))*SP + WZ1*MU
        ENDIF

        EG1 = EG2
        X1 = X2
        Y1 = Y2
        Z1 = Z2
        WX1 = WX2
        WY1 = WY2
        WZ1 = WZ2
        GO TO 20                        !Continue to travel

! Photon out of ROI
30      NOB = NOB + 1.0
        GOTO 50
C
C  In the Collimator
C
40      NCOLL = NCOLL + 1.0

C  Rejected or Transmitted by the Collimator
        IZ = INT(Z1)
        FWHM = (FWHMDATA(IZ+2)-FWHMDATA(IZ+1))*
     +  (Z1-FLOAT(IZ))+FWHMDATA(IZ+1)
        DDO =2.*SQRT((XC-X1)**2.+(YC-Y1)**2.)

! Rejected by the Collimator
        IF (DDO.GT.FWHM) GOTO 50

! Accepted by the Collimator
! 1. Position of gamma in the collimator
C       QX = (XC-XCL)/DELC+1.
C       QY = (YC-YCL)/DELC+1.
C       II = INT(QY)
C       JJ = INT(QX)
C       IF (II.EQ.NC+1) II = NC
C       IF (JJ.EQ.NC+1) JJ = NC
C       COLLPHOTON(II,JJ) = COLLPHOTON(II,JJ) + 1.
C       COLLENERGY(II,JJ) = COLLENERGY(II,JJ) + EG1
```

```fortran
! 2. Energy Spectrum
        QE = (EG1-EMINV)/DELE + 1.
        IE = INT(QE)
        IF (IE.EQ.NE+1) IE = NE
        ESPECT(IE) = ESPECT(IE) + 1.
C
C  In the Scintillator
C
        NSCINT = NSCINT + 1.0
        CALL PSFCSI (IX,EG1,XC,YC,XSH,XSL,YSH,YSL,ZSH,ZSL,XDH,
     +              XDL,YDH,YDL,ND,DELD,SCST,SPAT,SEST,VPHOTT,
     +              VDETT,IMAGE)

50      NCST = NCST + FLOAT(NCS)

100     CONTINUE
        WRITE(*,*) 'KY=',KY
102     CONTINUE
        WRITE(*,*) 'KZ=',KZ
        WRITE(*,*)
C
C  Print Output Images
C
! IMAGE.OUT
        OPEN (13,FILE='IMAGE.OUT',STATUS='NEW')
        DO 90 J=ND,1,-1
90              WRITE(13,1000) (IMAGE(J,K),K=1,ND)
1000            FORMAT(8(1X,E9.3))
        CLOSE (13)

105     CONTINUE

C
C  Statistics
C
! 1.Water Phantom
        NTOTAL = NPA + NCST              !Total # of Events in Phantom
        PPA1 = NPA/NTOTAL*100.           !% of Photoelectric Abs. Events
        PCS = 100. - PPA1                !% of Compton Scattering Events
        FNGAMMA = 100./NGAMMA
        PPA2 = NPA*FNGAMMA               !% of Absorbed Gamma Photons
        POB = NOB*FNGAMMA                !% of Escaped Gamma Photons
        PLE = NLE*FNGAMMA                !% of Energy-Lost Gamma Photons
! 2.Collimator
        PCOLL = NCOLL*FNGAMMA            !% of Collimator-Arrived Phots.
        PSCINT = NSCINT*FNGAMMA          !% of Coll.-Transmitted Phots.
! 3.Scintillator
!   3.1 Gamma Photons
        STOTAL = SPAT + SCST             !Total # of Events in the Scintillator
        PSPAT = SPAT*100./STOTAL         !% of Photoelectric Absorption Events
        PSCST = 100.-PSPAT               !% of Compton Scattering Events
        PSAB = SPAT/NSCINT*100.          !% of Absorbed Gamma Photons
        PSES = 100.-PSAB                 !% of Escaped Gamma Photons
!   3.2 Visible Photons
```

162

```fortran
      VUNDT = VPHOTT - VDETT      !Total # of Undetected Visible Photons
      PVDETT = VDETT/VPHOTT*100.  !% of Detected Visible Photons
      PVUNDT = 100. - PVDETT      !% of Undetected Visible Photons
C
C Print Summary of Calculations
C
      WRITE(10,860) NTOTAL,NPA,PPA1,NCST,PCS
860   FORMAT('1',
     + ' ************ SUMMARY OF SIMULATIONS ************',
     + //' *** Water Phantom ***'/
     + ' Total # of Events in the Water Phantom = ',E10.3/
     + ' Total # of Phtoelectric Events = ',E10.3,2X,'(',F6.2,'%)'/
     + ' Total # of Compton Scatterings = ',E10.3,2X,'(',F6.2,'%)'/)
      WRITE(10,870) NPA,PPA2,NOB,POB,NLE,PLE
870   FORMAT(' Total # of Absorbed Gamma Photons = ',
     + E10.3,2X,'(',F6.2,'%)'/
     + ' Total # of Escaped Gamma Photons = ',E10.3,2X,'(',F6.2,'%)'/
     + ' Total # of Energy-Lost Gamma Photons = ',
     + E10.3,2X,'(',F6.2,'%)'//)
      WRITE(10,890) NCOLL,PCOLL,NSCINT,PSCINT
890   FORMAT(' *** Collimator ***'/
     + ' Total # of Collimator-Reached Gamma Photons = ',E10.3,
     + 2X,'(',F6.2,'%)'/
     + ' Total # of Collimator-Transmitted Gamma Photons = ',
     + E10.3,2X,'(',F6.2,'%)'//)
      WRITE(10,900) STOTAL,SPAT,PSPAT,SCST,PSCST
900   FORMAT(' *** Scintillator (CsI) ***'/
     + ' +++ 1. Gamma Photons +++'/
     + ' Total # of Events in the Scintillator = ',E10.3/
     + ' Total # of Phtoelectric Events = ',E10.3,2X,'(',F6.2,'%)'/
     + ' Total # of Compton Scatterings = ',E10.3,2X,'(',F6.2,'%)'/)
      WRITE(10,910) SPAT,PSAB,SEST,PSES
910   FORMAT(1X,'Total # of Absorbed Gamma Photons = ',
     + E10.3,2X,'(',F6.2,'%)',/
     + ' Total # of Escaped Gamma Photons = ',
     + E10.3,2X,'(',F6.2,'%)'/)
      WRITE(10,920) VPHOTT,VDETT,PVDETT,VUNDT,PVUNDT
920   FORMAT(' +++ 2. Output Visible Photons +++'/
     + ' Total # of Output Visible Photons = ',E10.3/
     + ' Total # of Detected Visible Photons = ',
     + E10.3,2X,'(',F6.2,'%)'/
     + ' Total # of Undetected Visible Photons = ',
     + E10.3,2X,'(',F6.2,'%)')
C
C Print Energy Spectrum
C
      OPEN(14, FILE='SPECTRUM.OUT',STATUS='NEW')
      WRITE(14,1100)
1100  FORMAT(' Channel #',3X,'Energy [MeV]',3X,'# of Gamma')
      DO 200 I = 1,NE
          ENERGY = EMINV + (FLOAT(I)-0.5)*DELE
200       WRITE(14,1200) I,ENERGY,ESPECT(I)
1200      FORMAT(1X,I4,5X,F7.4,5X,E11.4)
C
```

```
C Update Random Number Seed data file (RAN-SEED.DAT)
C
        OPEN (2,FILE='RAN-SEED.DAT', STATUS='NEW')
        WRITE(2,*) IX

        WRITE(*,*) 'Hee Haw! Simulation ended at last!!'
        END




        SUBROUTINE HEADING (EGS,NORMALSPOT,HOTSPOT,
     +        PNORMAL,PHOT,LINE_NORMAL,LINE_HOT,NGAMMA,
     +        SOURCE_HNRATIO,IMAGE_HNRATIO,
     +        XSRCH,YSRCH,ZSRCH,ZSRCL,NSRCX,NSRCY,NSRCZ,
     +        DELSRC,XPH,YPH,ZPH,COLTYPE,XCH,YCH,NC,DELC,
     +        XSH,YSH,ZSH,XDH,YDH,ND,DELD,EMIN,EMAX,NE,DELE)

        INTEGER*4 NORMALSPOT,HOTSPOT,PNORMAL,PHOT
        REAL NGAMMA, IMAGE_HNRATIO
        CHARACTER COLTYPE*16, DMY*9, HMS*8
        WRITE(10,*) 'SUMMARY.OUT'
        CALL DATE(DMY)
        CALL TIME(HMS)
        WRITE(10,910) DMY,HMS
910         FORMAT(1X/1X,A9,7X,A8/)
        WRITE(10,915)
915     FORMAT(' *********** SYSTEM SPECIFICATIONS ***********')
        WRITE(10,920) EGS,NGAMMA,2.*XSRCH,2.*YSRCH,
     +        (ZSRCH-ZSRCL),ZSRCL,DELSRC,DELSRC,DELSRC,
     +        NSRCX,NSRCY,NSRCZ,PNORMAL,PHOT,
     +        NORMALSPOT,HOTSPOT,SOURCE_HNRATIO,
     +        IMAGE_HNRATIO
920     FORMAT(1X,'*** Gamma Sources ***'/' Eo = ',F5.3,'MeV'/
     +        ' Total # of Gamma Source Quanta = ',E10.3/
     +        ' Direction = Isotropic btwn mu = 0 ~ -1'/
     +        ' Source Object Size = (',2(F3.1,', '),F4.1,') [cm]'/
     +        ' Distance btwn Object bottom and Collimator = 'F4.1' [cm]'/
     +        ' Source Object Pixel Size = ',2(F4.2,' x '),F4.2,' [cm^3]'/
     +        ' # of Pixels (x,y,z) = '2(I3' x ')I3/
     +        ' # of Normal Pixels = 'I5/' # of Hotspot Pixels = 'I5/
     +        ' # of Gamma Source in NORMAL pixel = 'I12/
     +        ' # of Gamma Source in HOTSPOT pixel = 'I12/
     +        ' Source_Hot/Normal = 'F8.1/
     +        ' Detector Image_Hot/Normal = 'F8.1/)

        WRITE(10,930) 2.*XPH,2.*YPH,ZPH
930     FORMAT(1X,'*** Water Phantom ***'/1X,'Phantom Size = ',
     +        2(F4.1,' x '),F4.1,' [cm^3]'/)
        WRITE(10,940) COLTYPE,2.*XCH,2.*YCH,DELC,NC,NC
940     FORMAT(1X,'*** Collimator ***'/1X,'Collimator Type = ',
     +        A16/' Collimator Area = ',F7.4,' x ',F7.4,' [cm^2]'/
     +        ' Collimator Pixel Size = 'F6.4,' [cm]'/' # of Pixel = ',
     +        I3,' x ',I3/)
```

```
        WRITE(10,942) 2.*XSH,2.*YSH,ZSH
942     FORMAT(1X,'*** Scintillator ***'/1X,'Scintillator Size = ',
    +         2(F4.1,' x '),F4.1,' [cm^3]'/)
        WRITE(10,944) 2.*XDH,2.*YDH,DELD,ND,ND
944     FORMAT(1X,'*** Detector ***'/' Detector Size = ',
    +         F7.4,' x ',F7.4,' [cm^2]'/' Detector Pixel Size = ',
    +         F6.4,' [cm]'/' # of Pixel = ',I3,' x ',I3//)
        WRITE(10,955) EMIN,EMAX,NE,DELE*1000.
955     FORMAT(1X,'*** Energy Spectrum Setting ***'/
    +         ' Emin = ',F7.3,'[MeV]'/
    +         ' Emax = ',F7.3,'[MeV]'/' # of Channels = ',I4,/
    +         ' Energy Width for a Channel = ',F7.4,'[KeV]')
        END




C CROSS-WATER.FOR

        SUBROUTINE CROSSWATER(EG,SIGC,SIGP,SIGT)

C This program calculates Cross Sections of Compton Scaterring and
C Photoelectric Effects in WATER
C using INTERPOLATIONS :
C
C       Compton Scattering  : Linear Interpolation
C       Photoelectric Effect : log(sigma) = a*log(Egamma) + b
C

        IF (EG .LE. 0.048) THEN
         IF (EG .LE. 0.024) THEN
          IF (EG .LE. 0.014) THEN
           IF (EG .LE. 0.011) THEN
            CALL SIGMA(EG,0.010,0.011,0.2140,0.2134,4.78,3.4,SIGC,SIGP)
           ELSEIF (EG .LE. 0.012) THEN
            CALL SIGMA(EG,0.011,0.012,0.2134,0.2117,3.4,2.6,SIGC,SIGP)
           ELSEIF (EG .LE. 0.013) THEN
            CALL SIGMA(EG,0.012,0.013,0.2117,0.2111,2.6,2.0,SIGC,SIGP)
           ELSE
            CALL SIGMA(EG,0.013,0.014,0.2111,0.2095,2.0,1.5,SIGC,SIGP)
           ENDIF
          ELSEIF (EG .LE. 0.019) THEN
           IF (EG .LE. 0.015) THEN
            CALL SIGMA(EG,0.014,0.015,0.2095,0.2079,1.5,1.27,SIGC,SIGP)
           ELSEIF (EG .LE. 0.016) THEN
            CALL SIGMA(EG,0.015,0.016,0.2079,0.2072,1.27,1.0,SIGC,SIGP)
           ELSEIF (EG .LE. 0.017) THEN
            CALL SIGMA(EG,0.016,0.017,0.2072,0.2066,1.0,0.8,SIGC,SIGP)
           ELSEIF (EG .LE. 0.018) THEN
            CALL SIGMA(EG,0.017,0.018,0.2066,0.2068,0.8,0.66,SIGC,SIGP)
           ELSE
            CALL SIGMA(EG,0.018,0.019,0.2068,0.2072,0.66,0.56,SIGC,SIGP)
           ENDIF
          ELSE
```

```
      IF (EG . LE. 0.02 ) THEN
          CALL  SIGMA(EG,0.019,0.02,0.2072,0.2065,0.56,0.505,SIGC,SIGP)
      ELSEIF (EG .LE. 0.021 ) THEN
          CALL  SIGMA(EG,0.020,0.021,0.2065,0.2058,0.505,0.40,SIGC,SIGP)
      ELSEIF (EG .LE. 0.022 ) THEN
          CALL  SIGMA(EG,0.021,0.022,0.2058,0.2051,0.40,0.36,SIGC,SIGP)
      ELSEIF (EG .LE. 0.023) THEN
          CALL  SIGMA(EG,0.022,0.023,0.2051,0.2045,0.36,0.30,SIGC,SIGP)
      ELSE
          CALL  SIGMA(EG,0.023,0.024,0.2045,0.2038,0.30,0.26,SIGC,SIGP)
      ENDIF
    ENDIF
  ELSE
   IF (EG .LE. 0.029) THEN
     IF (EG . LE. 0.025) THEN
          CALL  SIGMA(EG,0.024,0.025,0.2038,0.2030,0.26,0.23,SIGC,SIGP)
      ELSEIF (EG .LE. 0.026) THEN
          CALL  SIGMA(EG,0.025,0.026,0.2030,0.2024,0.23,0.20,SIGC,SIGP)
      ELSEIF (EG .LE. 0.027) THEN
          CALL  SIGMA(EG,0.026,0.027,0.2024,0.2017,0.20,0.18,SIGC,SIGP)
      ELSEIF (EG .LE. 0.028) THEN
          CALL  SIGMA(EG,0.027,0.028,0.2017,0.2010,0.18,0.16,SIGC,SIGP)
      ELSE
          CALL  SIGMA(EG,0.028,0.029,0.2010,0.2001,0.16,0.14,SIGC,SIGP)
      ENDIF
   ELSEIF (EG .LE. 0.038) THEN
     IF (EG . LE. 0.030) THEN
          CALL  SIGMA(EG,0.029,0.030,0.2001,0.1995,0.14,0.12,SIGC,SIGP)
      ELSEIF (EG .LE. 0.032) THEN
          CALL  SIGMA(EG,0.030,0.032,0.1995,0.1980,0.12,0.10,SIGC,SIGP)
      ELSEIF (EG .LE. 0.034) THEN
          CALL  SIGMA(EG,0.032,0.034,0.1980,0.1975,0.10,0.083,SIGC,SIGP)
      ELSEIF (EG .LE. 0.036) THEN
          CALL SIGMA(EG,0.034,0.036,0.1975,0.1970,0.083,0.070,SIGC,SIGP)
      ELSE
          CALL SIGMA(EG,0.036,0.038,0.1970,0.1955,0.070,0.058,SIGC,SIGP)
      ENDIF
   ELSE
     IF (EG . LE. 0.040) THEN
          CALL  SIGMA(EG,0.038,0.040,0.1955,0.194,0.058,0.048,SIGC,SIGP)
      ELSEIF (EG .LE. 0.042) THEN
          CALL SIGMA(EG,0.040,0.042,0.1940,0.1935,0.048,0.042,SIGC,SIGP)
      ELSEIF (EG .LE. 0.044) THEN
          CALL SIGMA(EG,0.042,0.044,0.1935,0.1920,0.042,0.036,SIGC,SIGP)
      ELSEIF (EG .LE. 0.046) THEN
          CALL SIGMA(EG,0.044,0.046,0.1920,0.1905,0.036,0.030,SIGC,SIGP)
      ELSE
          CALL SIGMA(EG,0.046,0.048,0.1905,0.1888,0.030,0.027,SIGC,SIGP)
      ENDIF
    ENDIF
  ENDIF
ELSE
 IF (EG .LE. 0.0833) THEN
   IF (EG .LE. 0.058) THEN
```

```
        IF (EG . LE. 0.050) THEN
            CALL SIGMA(EG,0.048,0.050,0.1888,0.1872,0.027,0.023,SIGC,SIGP)
        ELSEIF (EG .LE. 0.052) THEN
            CALL SIGMA(EG,0.050,0.052,0.1872,0.1866,0.023,0.021,SIGC,SIGP)
        ELSEIF (EG .LE. 0.054) THEN
            CALL SIGMA(EG,0.052,0.054,0.1866,0.1860,0.021,0.018,SIGC,SIGP)
        ELSEIF (EG .LE. 0.056) THEN
            CALL SIGMA(EG,0.054,0.056,0.1860,0.1844,0.018,0.016,SIGC,SIGP)
        ELSE
            CALL SIGMA(EG,0.056,0.058,0.1844,0.1838,0.016,0.014,SIGC,SIGP)
        ENDIF
      ELSEIF (EG .LE. 0.068) THEN
        IF (EG . LE. 0.060) THEN
            CALL SIGMA(EG,0.058,0.060,0.1838,0.1832,0.014,0.012,SIGC,SIGP)
        ELSEIF (EG .LE. 0.062) THEN
            CALL SIGMA(EG,0.060,0.062,0.1832,0.1815,0.012,0.011,SIGC,SIGP)
        ELSEIF (EG .LE. 0.064) THEN
            CALL SIGMA(EG,0.062,0.064,0.1815,0.1799,0.011,0.010,SIGC,SIGP)
        ELSEIF (EG .LE. 0.066) THEN
            CALL SIGMA(EG,0.064,0.066,0.1799,0.1793,0.010,0.0093,SIGC,SIGP)
        ELSE
            CALL SIGMA(EG,0.066,0.068,0.1793,0.1786,0.0093,0.0087,SIGC,SIGP)
        ENDIF
      ELSE
        IF (EG .LE. 0.070) THEN
            CALL SIGMA(EG,0.068,0.070,0.1786,0.1770,0.0087,0.0080,SIGC,SIGP)
        ELSEIF (EG .LE. 0.0733) THEN
            CALL SIGMA(EG,0.070,.0733,0.1770,0.1755,0.0080,0.0068,SIGC,SIGP)
        ELSEIF (EG .LE. 0.0766) THEN
            CALL SIGMA(EG,.0733,.0766,.1755,.1740,0.0068,0.0056,SIGC,SIGP)
        ELSEIF (EG .LE. 0.08) THEN
            CALL SIGMA(EG,.0766,0.08,.1740,.1714,0.0056,0.0050,SIGC,SIGP)
        ELSE
            CALL SIGMA(EG,0.08,.0833,.1714,.1710,0.0050,0.0042,SIGC,SIGP)
        ENDIF
      ENDIF
      ELSE
        IF (EG .LE. 0.1) THEN
        IF (EG .LE. 0.0866) THEN
            CALL SIGMA(EG,.0833,.0866,.1710,.1693,0.0042,0.0038,SIGC,SIGP)
        ELSEIF (EG .LE. 0.090) THEN
            CALL SIGMA(EG,.0866,0.090,.1693,.1678,0.0038,0.0032,SIGC,SIGP)
        ELSEIF (EG .LE. 0.0933) THEN
            CALL SIGMA(EG,0.090,.0933,.1678,.1660,0.0032,0.0029,SIGC,SIGP)
        ELSEIF (EG .LE. 0.0966) THEN
            CALL SIGMA(EG,0.0933,0.0966,.1660,.1645,.0029,.0026,SIGC,SIGP)
        ELSE
            CALL SIGMA(EG,.0966,0.10,.1645,.1629,0.0026,0.0022,SIGC,SIGP)
        ENDIF
      ELSE
        IF (EG .LE. 0.11) THEN
            CALL SIGMA(EG,0.10,0.11,.1629,.1600,.0022,.0017,SIGC,SIGP)
        ELSEIF (EG .LE. 0.12) THEN
            CALL SIGMA(EG,0.11,0.12,.1600,.156,.0017,.0013,SIGC,SIGP)
```

167

```
      ELSEIF (EG .LE. 0.13) THEN
          CALL  SIGMA(EG,0.12,0.13,.156,.154,.0013,.00097,SIGC,SIGP)
      ELSEIF (EG .LE. 0.14) THEN
          CALL  SIGMA(EG,0.13,0.14,.154,.1497,.00097,.00073,SIGC,SIGP)
      ELSE
          CALL  SIGMA(EG,0.14,0.15,.1497,.1474,.00073,.00058,SIGC,SIGP)
      ENDIF
     ENDIF
    ENDIF
ENDIF

SIGT = SIGC + SIGP

END

SUBROUTINE  SIGMA(EG,X1,X2,YC1,YC2,YP1,YP2,SIGC,SIGP)
SIGC=(YC2-YC1)*(EG-X1)/(X2-X1)+YC1

T1=LOG10(YP2/YP1)
T2=LOG10(EG/X1)
T3=LOG10(X2/X1)
SIGP=YP1*10.**(T1*T2/T3)

END




C  COMPTONR.FOR

    SUBROUTINE COMPTONR(IX,EG1,EG2,MU)

C This program determines the ENERGY and the ANGLE of the Compton-scattered
C photon using Klein-Nishina formula and REJECTION METHOD (KAHN)

    REAL MC
    DOUBLE PRECISION MU,AL,ALO

    PI = 3.141592654
    MC = 0.511              !Electron mass energy          [MeV]
    ALO = EG1/MC

C Rejection Method
10     RH1 = RAN(IX)
       RH2 = RAN(IX)
       RH3 = RAN(IX)

       VAL1 = (1. + 2.*ALO)/(9. + 2.*ALO)
       IF (RH1 .LE. VAL1) THEN
              X = 1.+2.*RH2*ALO
              VAL2 = 4.*(1./X - 1./X**2.)
              IF (RH3 .LE. VAL2) THEN
                    AL = ALO/X
              ELSE
```

```
                GOTO 10
        ENDIF
    ELSE
        X = (1.+2.*ALO)/(1.+2.*RH2*ALO)
        VAL2 = (1./ALO - X/ALO + 1.)**2. + 1./X
        IF (2.*RH3 .LE. VAL2) THEN
                AL = ALO/X
        ELSE
                GOTO 10
        ENDIF
    ENDIF

C  Results
        EG2 = AL*MC
        MU = 1. - 1./AL + 1./ALO

        END




C  PSF-CSI-SUB.FOR
C
C  This Program calculates the POINT-SPREAD FUNCTION of CsI(Tl) output photons
C  when a single gamma ray is incident normal to the scintillator surface
C
C  Number of Collisions
C        SCST  : Total No. of Compton Scatterings of Gamma Photons
C        SPAT  : Total No. of Photoelectric Absorp. of Gamma Photons
C        SEST  : Total No. of Escaping Gamma Photons
C  Numbers about Output Visible Photons
C        VPHOTT      : Total No. of Output Visible Photons
C        VDETT       : Total No. of Detected Output Visible Photons


        SUBROUTINE  PSFCSI(IX,EG0,X0,Y0,XSH,XSL,YSH,YSL,ZSH,ZSL,
   +                XDH,XDL,YDH,YDL,ND,DELD,SCST,SPAT,SEST,
   +                VPHOTT,VDETT,IMAGE)

        REAL MC
        REAL IMAGE(ND,ND)
        DOUBLE PRECISION SCST,SPAT,SEST,VDETT,MU

C  Constants
        PI = 3.141592654
        MC = 0.511              ! Electron Mass Energy                   [MeV]
        YIELD = 53000.          ! # of Visible Photons for 1 MeV Gamma Rays

C  Incident Gamma Ray
        EG1 = EG0               ! Incident Energy                        [MeV]
        X1 = X0                 ! x-position of incident gamma           [cm]
        Y1 = Y0                 ! y-position    "      "  "               [cm]
        Z1 = ZSH                ! z-position(thick.of CsI(Tl))           [cm]
        WX1 = 0.                ! x-direction of incident gamma
```
169

```fortran
      WY1 = 0.                    ! y-direction    " "      " "
      WZ1 = -1.                   ! z-direction    " "      " "

      NCS = 0                     ! No. of Compton Scattering
      NPA = 0                     ! No. of Photoelectric Absorp.
      NES = 0                     ! No. of Escaping

C Next Collision Position
20    H = RAN(IX)
      IF (H .EQ. 0.0) GO TO 20
      CALL CROSSCSI(EG1,SIGC,SIGP,SIGT) ! Cross-Sections          [cm^-1]
      S = -LOG(H)/SIGT            ! Traveling Distance       [cm]
      X2 = X1 + S*WX1             ! x-collision position     [cm]
      Y2 = Y1 + S*WY1             ! y-collision position     [cm]
      Z2 = Z1 + S*WZ1             ! z-collision position     [cm]
      NC = NC +1                  ! No. of Collision
      IF ((Z2.LT.ZSL).OR.(Z2.GT.ZSH)) GOTO 30
      IF ((X2.LT.XSL).OR.(X2.GT.XSH)) GOTO 30
      IF ((Y2.LT.YSL).OR.(Y2.GT.YSH)) GOTO 30


C Collision Type
      PP = SIGP/SIGT              ! Probability of PHOTOELECTRIC EFFECT
      H = RAN(IX)
! Photoelectric Absorption
      IF (H.LE.PP) THEN
        NPA = NPA + 1
        EE = EG1                            ! Electron Energy           [MeV]
        NVPHOT = NINT(YIELD*EE)    ! # of generated visible photons for an event
        VPHOTT = VPHOTT + NVPHOT           ! total # of generated visible photons
! Positions of Output Visible Phtons
            CALL OUTPOSEVEN(IX,XDL,XDH,YDL,YDH,ND,DELD,X2,Y2,Z2,
     +           NVPHOT,VDETT,IMAGE)
        GO TO 40
      END IF
! Compton Scattering
      NCS = NCS + 1
      CALL COMPTONR(IX,EG1,EG2,MU)        ! Obtain mu
      EE = EG1 - EG2                      ! Recoil Electron Energy     [MeV]
      NVPHOT = NINT(YIELD*EE)
      VPHOTT = VPHOTT + NVPHOT
! Positions of Output Visible Phtons
      CALL OUTPOSEVEN(IX,XDL,XDH,YDL,YDH,ND,DELD,X2,Y2,Z2,
     +           NVPHOT,VDETT,IMAGE)
      IF (EG2.LE.0.0) GOTO 40
! Direction of Scattered Gamma Ray
      PHI = 2.*PI*RAN(IX)                 !Sampling of azimuthal angle (isotropic) [radian]
      CP = COS(PHI)
      SP = SIN(PHI)
      IF ((WZ1.EQ.-1.0).OR.(WZ1.EQ.1.0)) THEN
            TERM1 = SQRT(1.-MU**2.)
            WX2 = TERM1*CP
            WY2 = TERM1*SP
            WZ2 = WZ1*MU
      ELSE
```

```
                TERM1 = SQRT((1.-MU**2.)/(1.-WZ1**2.))
                WX2 = TERM1*(WY1*CP + WX1*WZ1*SP) + WX1*MU
                WY2 = TERM1*(-WX1*CP + WY1*WZ1*SP) + WY1*MU
                WZ2 = -SQRT((1.-WZ1**2.)*(1.-MU**2.))*SP + WZ1*MU
         ENDIF

         EG1 = EG2
         X1 = X2
         Y1 = Y2
         Z1 = Z2
         WX1 = WX2
         WY1 = WY2
         WZ1 = WZ2
         GO TO 20

C  Outside Collision
30       NES = NES + 1

40       SPAT = SPAT + FLOAT(NPA)
         SCST = SCST + FLOAT(NCS)
         SEST = SEST + FLOAT(NES)

         END




C CROSS-CSI.FOR

         SUBROUTINE CROSSCSI(EG,SIGC,SIGP,SIGT)
C
C This program calculates Cross Sections of Compton Scaterring and
C Photoelectric Effects using INTERPOLATIONS :
C
C        Compton Scattering  : Linear Interpolation
C        Photoelectric Effect : log(sigma) = a*log(Egamma) + b
C

         IF (EG .LE. 0.08) THEN
           IF (EG .LE. 0.03) THEN
             IF (EG .LE. 0.017) THEN
               IF(EG .LE. 0.011) THEN
               CALL SIGMA(EG,0.010,0.011,0.76,0.76,750.,600.,SIGC,SIGP)
               ELSE IF (EG .LE. 0.012) THEN
               CALL SIGMA(EG,0.011,0.012,0.76,0.76,600.,480.,SIGC,SIGP)
               ELSE IF (EG .LE. 0.013) THEN
               CALL SIGMA(EG,0.012,0.013,0.76,0.76,480.,380.,SIGC,SIGP)
               ELSE IF (EG .LE. 0.014) THEN
               CALL SIGMA(EG,0.013,0.014,0.76,0.76,380.,310.,SIGC,SIGP)
               ELSE IF (EG .LE. 0.015) THEN
               CALL SIGMA(EG,0.014,0.015,0.76,0.76,310.,256.,SIGC,SIGP)
               ELSE IF (EG .LE. 0.016) THEN
               CALL SIGMA(EG,0.015,0.016,0.76,0.76,256.,220.,SIGC,SIGP)
               ELSE
```

```
                CALL  SIGMA(EG,0.016,0.017,0.76,0.76,220.,190.,SIGC,SIGP)
                END IF
        ELSE
            IF (EG .LE. 0.018) THEN
            CALL  SIGMA(EG,0.017,0.018,0.76,0.76,190.,160.,SIGC,SIGP)
            ELSE IF (EG .LE. 0.019) THEN
            CALL  SIGMA(EG,0.018,0.019,0.76,0.76,160.,140.,SIGC,SIGP)
            ELSE IF (EG .LE. 0.020) THEN
            CALL  SIGMA(EG,0.019,0.020,0.76,0.75,140.,125.,SIGC,SIGP)
            ELSE IF (EG .LE. 0.022) THEN
            CALL  SIGMA(EG,0.020,0.022,0.75,0.75,125.,95.,SIGC,SIGP)
            ELSE IF (EG .LE. 0.024) THEN
            CALL  SIGMA(EG,0.022,0.024,0.75,0.74,95.,80.,SIGC,SIGP)
            ELSE IF (EG .LE. 0.026) THEN
            CALL  SIGMA(EG,0.024,0.026,0.74,0.74,80.,65.,SIGC,SIGP)
            ELSE IF (EG .LE. 0.028) THEN
            CALL  SIGMA(EG,0.026,0.028,0.74,0.74,65.,55.,SIGC,SIGP)
            ELSE
                CALL  SIGMA(EG,0.028,0.030,0.74,0.73,55.,44.,SIGC,SIGP)
            END IF
        END IF
    ELSE
      IF (EG .LE. 0.046) THEN
            IF (EG .LE. 0.032) THEN
                CALL  SIGMA(EG,0.030,0.032,0.73,0.73,44.,36.,SIGC,SIGP)
            ELSE IF (EG  .LE. 0.034) THEN
                CALL  SIGMA(EG,0.032,0.034,0.73,0.72,36.,32.,SIGC,SIGP)
            ELSE IF (EG  .LE. 0.036) THEN
                CALL  SIGMA(EG,0.034,0.036,0.72,0.71,32.,27.,SIGC,SIGP)
            ELSE IF (EG  .LE. 0.038) THEN
                CALL  SIGMA(EG,0.036,0.038,0.71,0.71,27.,80.,SIGC,SIGP)
            ELSE IF (EG  .LE. 0.040) THEN
                CALL  SIGMA(EG,0.038,0.040,0.71,0.70,80.,70.,SIGC,SIGP)
            ELSE IF (EG  .LE. 0.042) THEN
                CALL  SIGMA(EG,0.040,0.042,0.70,0.70,70.,115.,SIGC,SIGP)
            ELSE IF (EG  .LE. 0.044) THEN
            CALL  SIGMA(EG,0.042,0.044,0.70,0.69,115.,105.,SIGC,SIGP)
            ELSE
                CALL  SIGMA(EG,0.044,0.046,0.69,0.69,105.,90.,SIGC,SIGP)
            END IF
        ELSE
            IF (EG .LE. 0.048) THEN
                CALL  SIGMA(EG,0.046,0.048,0.69,0.68,90.,75.,SIGC,SIGP)
            ELSE IF (EG .LE. 0.050) THEN
                CALL  SIGMA(EG,0.048,0.050,0.68,0.67,75.,68.,SIGC,SIGP)
            ELSE IF (EG .LE. 0.055) THEN
                CALL  SIGMA(EG,0.050,0.055,0.67,0.67,68.,55.,SIGC,SIGP)
            ELSE IF (EG .LE. 0.060) THEN
                CALL  SIGMA(EG,0.055,0.060,0.67,0.66,55.,41.,SIGC,SIGP)
            ELSE IF (EG .LE. 0.065) THEN
                CALL  SIGMA(EG,0.060,0.065,0.66,0.65,41.,34.,SIGC,SIGP)
            ELSE IF (EG .LE. 0.070) THEN
                CALL  SIGMA(EG,0.065,0.070,0.65,0.65,34.,27.,SIGC,SIGP)
            ELSE IF (EG .LE. 0.075) THEN
```

```fortran
              CALL  SIGMA(EG,0.070,0.075,0.65,0.64,27.,23.,SIGC,SIGP)
          ELSE
              CALL  SIGMA(EG,0.075,0.080,0.64,0.63,23.,18.,SIGC,SIGP)
          END IF
      END IF
    END IF
ELSE
  IF (EG .LE. 0.24) THEN
    IF (EG .LE. 0.14) THEN
      IF (EG .LE. 0.085) THEN
              CALL  SIGMA(EG,0.080,0.085,0.63,0.62,18.,16.,SIGC,SIGP)
          ELSE IF (EG .LE. 0.090) THEN
              CALL  SIGMA(EG,0.085,0.090,0.62,0.61,16.,13.,SIGC,SIGP)
          ELSE IF (EG .LE. 0.095) THEN
              CALL  SIGMA(EG,0.090,0.095,0.61,0.60,13.,12.,SIGC,SIGP)
          ELSE IF (EG .LE. 0.10) THEN
              CALL  SIGMA(EG,0.095,0.10,0.60,0.60,12.,10.,SIGC,SIGP)
          ELSE IF (EG .LE. 0.11) THEN
              CALL  SIGMA(EG,0.10,0.11,0.60,0.59,10.,8.,SIGC,SIGP)
          ELSE IF (EG .LE. 0.12) THEN
              CALL  SIGMA(EG,0.11,0.12,0.59,0.57,8.,6.5,SIGC,SIGP)
          ELSE IF (EG .LE. 0.13) THEN
              CALL  SIGMA(EG,0.12,0.13,0.57,0.56,6.5,5.,SIGC,SIGP)
          ELSE
              CALL  SIGMA(EG,0.13,0.14,0.56,0.55,5.,4.1,SIGC,SIGP)
          END IF
      ELSE
      IF (EG .LE. 0.15) THEN
              CALL  SIGMA(EG,0.14,0.15,0.55,0.55,4.1,3.3,SIGC,SIGP)
          ELSE IF (EG .LE. 0.16) THEN
              CALL  SIGMA(EG,0.15,0.16,0.55,0.54,3.3,2.8,SIGC,SIGP)
          ELSE IF (EG .LE. 0.17) THEN
              CALL  SIGMA(EG,0.16,0.17,0.54,0.53,2.8,2.4,SIGC,SIGP)
          ELSE IF (EG .LE. 0.18) THEN
              CALL  SIGMA(EG,0.17,0.18,0.53,0.52,2.4,2.0,SIGC,SIGP)
          ELSE IF (EG .LE. 0.19) THEN
              CALL  SIGMA(EG,0.18,0.19,0.52,0.51,2.0,1.7,SIGC,SIGP)
          ELSE IF (EG .LE. 0.20) THEN
              CALL  SIGMA(EG,0.19,0.20,0.51,0.50,1.7,1.5,SIGC,SIGP)
          ELSE IF (EG .LE. 0.22) THEN
              CALL  SIGMA(EG,0.20,0.22,0.50,0.48,1.5,1.15,SIGC,SIGP)
          ELSE
              CALL  SIGMA(EG,0.22,0.24,0.48,0.47,1.15,0.9,SIGC,SIGP)
          END IF
      END IF
    ELSE
    IF (EG .LE. 0.40) THEN
      IF (EG .LE. 0.26) THEN
              CALL  SIGMA(EG,0.24,0.26,0.47,0.46,0.9,0.7,SIGC,SIGP)
          ELSE IF (EG .LE. 0.28) THEN
              CALL  SIGMA(EG,0.26,0.28,0.46,0.45,0.7,0.58,SIGC,SIGP)
          ELSE IF (EG .LE. 0.30) THEN
              CALL  SIGMA(EG,0.28,0.30,0.45,0.44,0.58,0.46,SIGC,SIGP)
          ELSE IF (EG .LE. 0.32) THEN
```

```fortran
                    CALL  SIGMA(EG,0.30,0.32,0.44,0.43,0.46,0.40,SIGC,SIGP)
              ELSE IF (EG .LE. 0.34) THEN
                    CALL  SIGMA(EG,0.32,0.34,0.43,0.42,0.4,0.32,SIGC,SIGP)
              ELSE IF (EG .LE. 0.36) THEN
                    CALL  SIGMA(EG,0.34,0.36,0.42,0.42,0.32,0.28,SIGC,SIGP)
              ELSE IF (EG .LE. 0.38) THEN
                    CALL  SIGMA(EG,0.36,0.38,0.42,0.40,0.28,0.23,SIGC,SIGP)
              ELSE
                    CALL  SIGMA(EG,0.38,0.40,0.40,0.39,0.23,0.20,SIGC,SIGP)
              END IF
           ELSE
              IF (EG .LE. 0.42) THEN
                    CALL  SIGMA(EG,0.40,0.42,0.39,0.38,0.2,0.18,SIGC,SIGP)
              ELSE IF (EG .LE. 0.44) THEN
                    CALL  SIGMA(EG,0.42,0.44,0.38,0.37,0.18,0.16,SIGC,SIGP)
              ELSE IF (EG .LE. 0.46) THEN
                    CALL  SIGMA(EG,0.44,0.46,0.37,0.37,0.16,0.14,SIGC,SIGP)
              ELSE IF (EG .LE. 0.48) THEN
                    CALL  SIGMA(EG,0.46,0.48,0.37,0.36,0.14,0.125,SIGC,SIGP)
              ELSE
              CALL  SIGMA(EG,0.48,0.50,0.36,0.36,0.125,0.115,SIGC,SIGP)
              END IF
           END IF
         END IF
      END IF

      SIGT = SIGC + SIGP

      END



      SUBROUTINE SIGMA(EG,X1,X2,YC1,YC2,YP1,YP2,SIGC,SIGP)

      SIGC=(YC2-YC1)*(EG-X1)/(X2-X1)+YC1

      T1=LOG10(YP2/YP1)
      T2=LOG10(EG/X1)
      T3=LOG10(X2/X1)
      SIGP=YP1*10.**(T1*T2/T3)

      END




C OUTPOSEVEN.FOR

      SUBROUTINE OUTPOSEVEN(IX,XDL,XDH,YDL,YDH,ND,DELD,
     +            XP,YP,ZP,NVPHOT,VDETT,IMAGE)
C
C This program calculates the position of output visible photon AND
C also DIGITIZE the position
C
C IX          : Seed for Random Number Generation Function (RAN(IX))
```

174

```fortran
C XDL        : Lower Boundary of the Detector in X-direction
C XDH        : Upper  " "          " "              " "
C YDL        : Lower  " "          " "        in Y-direction
C YDH        : Upper  " "          " "              " "
C ND         : ND^2 = Pixel # of the Detector
C DELD       : Pixel Size of the Detector
C XP         : X-position of the Collision in the Scintillator
C YP         : Y-position         " "              " "
C ZP         : Z-position         " "              " "
C NVPHOT     : # of Visible Photons Generated by an Event
C VDET       :      " "    " "     " "          " "       and Detected
C VDETT      : Total # of detected visible photons
C IMAGE      : Image Array of the Detector
C
         REAL IMAGE(ND,ND)
         DOUBLE PRECISION VDETT
         PI = 3.141592654
         QE = 0.7                        ! Quantum Efficiency of Scint.and Det.
         NACTUAL = NINT(NVPHOT/2.*QE)     ! 1/2 of NVPHOT lost due to isotropic
                                          ! emission.
         VDET = 0.0
         DO 10 IP=1,NACTUAL
20          WZ = -1. + RAN(IX)           ! Cosine of Poloidal Angle (Isotropic
                                         ! between theta=90~180)

            IF (WZ.GE.0.0) GOTO 20
            PHI = 2.*PI*RAN(IX)          ! Azimuthal Angle (Isotropic)
            TERM = SQRT(1.-WZ**2.)
            WX = TERM*COS(PHI)
            WY = TERM*SIN(PHI)
            XI = XP - ZP*WX/WZ           ! X-position of Visible phot. on det.
            YI = YP - ZP*WY/WZ           ! Y-" "            " "      " "
            IF ((XI.LT.XDL).OR.(XI.GT.XDH).OR.
     +          (YI.LT.YDL).OR.(YI.GT.YDH)) THEN
               GOTO 10                   ! Undetected Visible Photon
            ENDIF
            VDET = VDET + 1.0
C Digitization of the Output Photon Position
            QX = (XI-XDL)/DELD + 1.
            QY = (YI-YDL)/DELD + 1.
            II = INT(QY)
            JJ = INT(QX)
            IF (II.EQ.ND+1) II = ND
            IF (JJ.EQ.ND+1) JJ = ND
            IMAGE(II,JJ) = IMAGE(II,JJ) + 1.
10       CONTINUE
         VDETT = VDETT + VDET
         END
```

LAWRENCE BERKELEY LABORATORY
UNIVERSITY OF CALIFORNIA
TECHNICAL INFORMATION DEPARTMENT
BERKELEY, CALIFORNIA 94720